



Draft Manuscript for Review

**Generation and rejuvenation of a supervolcanic magmatic system: a case study from Mangakino volcanic centre, New Zealand**

Journal:	<i>Journal of Petrology</i>
Manuscript ID	JPET-Aug-15-0095.R1
Manuscript Type:	Original Manuscript
Date Submitted by the Author:	n/a
Complete List of Authors:	Cooper, George; Durham University , Department of Earth Sciences Wilson, Colin; Victoria University, School of Geography, Environment and Earth Sciences Millet, Marc-Alban; Durham University, Department of Earth Sciences Baker, Joel; The University of Auckland, School of Environment
Keyword:	magma chamber, Kidnappers eruption, Rocky Hill eruption, supereruption, trace elements, rhyolite , Taupo Volcanic Zone

SCHOLARONE™  
Manuscripts

1  
2  
3 **Generation and rejuvenation of a supervolcanic magmatic system: a case study from**  
4  
5 **Mangakino volcanic centre, New Zealand**  
6  
7

8  
9 George F. Cooper<sup>1,2\*</sup>, Colin J.N. Wilson<sup>1</sup>, Marc-Alban Millet<sup>1,2</sup>, Joel A. Baker<sup>3</sup>  
10  
11

12  
13  
14 <sup>1</sup>School of Geography, Environment and Earth Sciences, Victoria University of Wellington,  
15  
16 PO Box 600, Wellington 6140, New Zealand  
17

18 <sup>2</sup>Present Address: Department of Earth Sciences, Durham University, Science Labs,  
19  
20 Durham DH1 3LE, UK  
21

22 <sup>3</sup>School of Environment, The University of Auckland, Private Bag 92019, Auckland, New  
23  
24 Zealand  
25  
26  
27  
28  
29  
30  
31  
32

33  
34 \*corresponding author:  
35

36 email: [george.cooper@durham.ac.uk](mailto:george.cooper@durham.ac.uk)  
37

38 phone: +44 7739525205  
39

40 fax: +44 0191 3342301  
41  
42  
43  
44

45 Keywords: Kidnappers eruption; magma chamber; Rocky Hill eruption; supereruption; trace  
46  
47 elements; rhyolite  
48  
49  
50  
51  
52  
53  
54  
55  
56  
57  
58  
59  
60

**ABSTRACT**

The Kidnappers (~1200 km<sup>3</sup>, DRE) and Rocky Hill (~200 km<sup>3</sup>, DRE) caldera-forming events (Taupo Volcanic Zone, New Zealand) were erupted in close succession from the Mangakino volcanic centre. They have identical radiometric ages at ~1 Ma, yet erosion along the contact between the two deposits suggest that some years to decades separated the two eruptions.

Field constraints, and the similarities of crystal textures and compositions and glass chemistries of both eruption deposits demonstrate that they came from one overall magmatic system with a common crystal mush source. However, second-order variations in these parameters confirm that the Kidnappers and Rocky Hill deposits represent distinct events and are not the products of a single zoned magma chamber. The systematically zoned Kidnappers fall deposits provide evidence for the tapping of three discrete magma bodies, whereas the succeeding Kidnappers ignimbrite is compositionally more diverse. The transition from fall to flow deposition marks a change in the style of caldera collapse and the simultaneous evacuation of discrete but compositionally diverse melts, each of which underwent a distinct evolution and were held at slightly different P–T conditions prior to eruption. Contrasting plagioclase and orthopyroxene zonation patterns are present from pumices originating from three discrete magma bodies. Less evolved mafic melts interacted with the system, which mobilised portions of the final erupted melt through heating and volatile/chemical exchange in the mush. The two largest Kidnappers melt-dominant bodies were re-tapped in modified form, or reestablished from their common mush source prior to, the Rocky Hill event. Rocky Hill pumices contain common, fluid-affected antecrystic crystal clots, derived from chamber wall material. Amphibole compositions from each eruption reflect melt evolution processes and, in particular, the coeval crystallisation of biotite and breakdown of orthopyroxene. Plagioclase and orthopyroxene from Rocky Hill pumices share common zonation patterns with those from the two largest magma bodies in the Kidnappers. The rapid production of

1  
2  
3 new melt-dominant bodies and the triggering of the Rocky Hill eruption reflect the ability of  
4  
5 the magmatic system to rejuvenate on a geologically short timescale. The Mangakino centre  
6  
7 did not follow a typical cycle of decreased activity after the supervolcanic Kidnappers event,  
8  
9 instead producing a second caldera-forming eruption, within years to decades from the same  
10  
11 system.  
12

## 13 14 15 16 **INTRODUCTION**

17  
18 Reconstructing the processes that occur in silicic (dacite and rhyolite) magma systems prior to  
19  
20 and during supereruptions ( $>10^{15}$  kg  $\approx$  450 km<sup>3</sup> of magma erupted; e.g. Miller & Wark, 2008),  
21  
22 and understanding how such vast parental bodies of magma are generated, stored and  
23  
24 ultimately erupted is challenging. Concepts of the nature and storage conditions of large  
25  
26 silicic magma bodies, and how a chemical zonation (if any) is developed within these magma  
27  
28 systems vary widely (e.g. Cashman & Giordano, 2014). Hildreth (1981) proposed the classic  
29  
30 high-silica rhyolite magma chamber paradigm, where any chemical or physical magma  
31  
32 chamber zonation is inversely reflected in the eruption products (Smith, 1979; Bachmann &  
33  
34 Bergantz, 2008). This model was largely based on compositional variations observed within  
35  
36 the Bishop Tuff (Hildreth, 1979), reflecting eruption of earlier crystal-poor, more evolved  
37  
38 magmas, followed by crystal-rich, less evolved magmas, with gradients in crystal content  
39  
40 matching those in chemical and mineralogical properties (Hildreth & Wilson, 2007;  
41  
42 Chamberlain *et al.*, 2015). Many large Quaternary rhyolitic deposits in the Taupo Volcanic  
43  
44 Zone (TVZ) of New Zealand show significant compositional variations (e.g. Briggs *et al.*,  
45  
46 1993; Brown *et al.*, 1998a, Milner *et al.*, 2003; Wilson *et al.*, 2006; Cooper *et al.*, 2012; Allan  
47  
48 *et al.*, 2013; Bégué *et al.*, 2014). These variations are, however, often non-systematic: erupted  
49  
50 compositions may be reversely ordered, or be distributed such that multiple discrete magma  
51  
52 bodies are inferred to have been tapped within single eruptive events, both large (Gravley *et*  
53  
54  
55  
56  
57  
58  
59  
60

1  
2  
3 *al.*, 2007; Cooper *et al.*, 2012; Bégué *et al.*, 2014) and small (Nairn *et al.*, 2004; Shane *et al.*,  
4  
5 2007, 2008a, b). Additionally, with the possible exception of Toba (Chesner, 2012), caldera-  
6  
7 forming eruptions are not isolated, but are coupled with other, smaller (by one or more orders  
8  
9 of magnitude) pre- and post-caldera eruptions from a common magmatic focus. At one  
10  
11 extreme, a precursor leak occurred only ~3 kyr prior to the 25.4 kyr Oruanui supereruption in  
12  
13 New Zealand, then there was only ~5 kyr of quiescence before frequent eruptive activity  
14  
15 resumed (e.g. Wilson & Charlier, 2009; Barker *et al.*, 2015). Other examples of smaller-scale  
16  
17 pre- and post-caldera activity include Yellowstone (Girard & Stix, 2010; Pritchard & Larson,  
18  
19 2012; Watts *et al.*, 2012), Valles caldera, New Mexico (Smith & Bailey, 1966; Self *et al.*,  
20  
21 1986; Stix *et al.*, 1988; Wolff *et al.*, 1999, 2011; Kennedy *et al.*, 2012), and Long Valley  
22  
23 caldera (Metz & Mahood, 1985, 1991; Hildreth, 2004).  
24  
25  
26

27  
28 In each of these systems, pre- and post-caldera-forming activity on short timescales  
29  
30 (thousands to tens of thousands of years) is modest in volume. A notable contrast to these  
31  
32 examples, however, is the 1 Ma (Houghton *et al.*, 1995; Wilson *et al.*, 1995a) Kidnappers and  
33  
34 Rocky Hill caldera-forming eruptions from Mangakino volcanic centre in the TVZ, which  
35  
36 were erupted in close succession from a common source (Wilson, 1986; Wilson *et al.*, 2008).  
37  
38 Zircon U–Pb age spectra in pumices from the two eruptions are closely similar, suggesting  
39  
40 that zircon growth occurred within a common magmatic system over a period of ~200 kyr,  
41  
42 with two peaks in zircon crystallisation about 100 kyr before and immediately prior to  
43  
44 eruption, respectively (Cooper *et al.*, 2014). The two sets of deposits collectively provide  
45  
46 windows into the short-term processes involved in the development and immediately post-  
47  
48 eruptive state of a supervolcanic magmatic system.  
49  
50

51  
52 The Kidnappers and Rocky Hill deposits also highlight issues in the material available  
53  
54 for analysis to interrogate the compositional record in large silicic eruptions. Stratigraphically  
55  
56 ordered fall deposits can be used to track compositional variations through time within and  
57  
58  
59  
60

1  
2  
3 between eruptions (e.g., Snake River Plain rhyolites; Perkins & Nash, 2002; Cathey & Nash,  
4  
5 2004). However, sufficiently large pumice clasts for individual analysis are absent in the  
6  
7 Kidnappers fall deposits, and therefore the inter-relationships between mineral, glass and  
8  
9 whole-rock compositions cannot be easily studied. Conversely, the Kidnappers and Rocky  
10  
11 Hill ignimbrites, although poorly exposed and lacking all but the broadest of stratigraphic  
12  
13 controls (e.g. the latter overlies the former), contain fresh pumices large enough to permit the  
14  
15 whole-rock, glass and mineral relationships of individual clasts to be explored.  
16  
17

18  
19 Here, we present geochemical and petrological data from the Kidnappers fall deposit,  
20  
21 and the Kidnappers and Rocky Hill ignimbrites in order to compare and contrast the deposits  
22  
23 and reconstruct their magmatic sources. Matrix glass from pumices within the Kidnappers and  
24  
25 Rocky Hill ignimbrites is compared to the three glass types previously identified in the  
26  
27 Kidnappers fall deposit (Cooper *et al.*, 2012). New mineral compositional data from the fall  
28  
29 deposit (organised by stratigraphic ordering) are compared alongside the data from ignimbrite  
30  
31 pumices (organised by major element chemistry), providing a record through the full  
32  
33 (preserved) stratigraphic history of the parental eruptions. The following questions are  
34  
35 addressed: (1) Can the distinction made between these eruptions from field evidence be  
36  
37 observed in the minerals and glasses, or geochemically and mineralogically do the  
38  
39 Kidnappers and Rocky Hill deposits appear to be phases of a single eruption? (2) How many  
40  
41 melt compositions were involved in the Kidnappers and Rocky Hill eruptions, and how were  
42  
43 they stored, and were they mixed? (3) Is evidence present in the geochemical and  
44  
45 mineralogical data to support inferences from zircon U–Pb age spectra (Cooper *et al.*, 2014)  
46  
47 that the Kidnappers and Rocky Hill deposits were derived from a common system? (4) Are  
48  
49 there any geochemical signatures present within the eruption deposits to give insights into  
50  
51 potential triggering mechanisms and rejuvenation processes? (5) Did conditions operating  
52  
53  
54  
55  
56  
57  
58  
59  
60

1  
2  
3 within the magmatic system (in particular temperature, pressure, oxygen fugacity and H<sub>2</sub>O  
4  
5 contents) remain constant or change between eruptive events?  
6  
7

## 8 9 **GEOLOGICAL BACKGROUND**

10  
11 The TVZ is a NNE-trending locus of volcanism and associated extension forming the  
12  
13 southern, continental termination of the Tonga–Kermadec arc, itself associated with westward  
14  
15 subduction of the Pacific plate beneath the Indo–Australian plate (Cole & Lewis, 1981). The  
16  
17 TVZ has been the dominant focus of volcanism in the central North Island of New Zealand  
18  
19 since ~2 Ma, and is divided into three segments on the basis of the dominant magma  
20  
21 composition and magma fluxes. Within the ~120 × 60 km rhyolite-dominated central  
22  
23 segment, >16,000 km<sup>3</sup> of magma has been erupted since ~1.6 Ma in >25 caldera-forming and  
24  
25 numerous other smaller eruptions from eight volcanic centres (Houghton *et al.*, 1995; Wilson  
26  
27 *et al.*, 1995b, 2009). The Mangakino volcanic centre (MVC; Fig. 1) on the northwestern  
28  
29 margin of the TVZ was recognised from the presence of a major negative gravity anomaly, in  
30  
31 addition to geological field evidence that linked several ignimbrites to a source in this area  
32  
33 (Blank, 1965; Stern, 1979; Rogan, 1982; Wilson *et al.*, 1984; Wilson, 1986). The MVC is a  
34  
35 composite feature, activity from which is grouped into two periods of caldera-forming  
36  
37 eruptions (Houghton *et al.*, 1995), from 1.62–1.51 Ma and 1.21–0.91 Ma. The latter period  
38  
39 includes the Kidnappers and Rocky Hill eruptions, as well as the 1.21 Ma Ongatiti  
40  
41 supereruption (Briggs *et al.*, 1993; Cooper & Wilson, 2014).  
42  
43  
44  
45  
46  
47

48 The Kidnappers and Rocky Hill eruptions are dated at ~1 Ma by <sup>40</sup>Ar/<sup>39</sup>Ar techniques  
49  
50 on plagioclase, and constrained by their position towards the top of the Jaramillo Normal  
51  
52 Subchron (1.07–0.99 Ma) (Black, 1992; Houghton *et al.*, 1995; Wilson *et al.*, 1995a; Tanaka  
53  
54 *et al.*, 1996; Singer, 2014). The Kidnappers is the second largest TVZ eruption known (1200  
55  
56 km<sup>3</sup> ± 50%, DRE; Cooper *et al.*, 2012) and it generated three components: (1) a voluminous  
57  
58  
59  
60

1  
2  
3 phreatomagmatic fall deposit, recorded across the North Island and for >1000 km eastwards  
4  
5 across the Pacific Ocean floor (Ash A of Ninkovich, 1968; Carter *et al.*, 2004; Cooper *et al.*,  
6  
7 2012); (2) an exceptionally widespread non-welded ignimbrite that covers ~45000 km<sup>2</sup>  
8  
9 (Wilson *et al.*, 1995a; Fig. 1); and (3) >1.3 km of poorly welded, hydrothermally altered tuff  
10  
11 deposited within the inferred source collapse structure (Wilson *et al.*, 2008). Geochemical  
12  
13 investigations of the fall deposit showed that three laterally separated magma chambers were  
14  
15 sequentially tapped during the volumetrically dominant earlier stages of the Kidnappers  
16  
17 eruption, within what became an inferred common composite caldera (Cooper *et al.*, 2012).  
18  
19

20  
21 The Kidnappers eruption was followed by a short period of quiescence before eruption  
22  
23 of the Rocky Hill ignimbrite (~200 km<sup>3</sup>, DRE), which extends to at least 85 km from source  
24  
25 (Briggs *et al.*, 1993; Fig. 1). The ignimbrite grades from a partially welded, pumice- and  
26  
27 crystal-rich base to a densely welded upper part with lower pumice abundance (Blank, 1965;  
28  
29 Wilson, 1986; Moyle, 1989). In addition, >0.5 km of Rocky Hill ignimbrite was penetrated by  
30  
31 drillholes within the Mangakino composite collapse caldera (Wilson *et al.*, 2008; Cooper *et*  
32  
33 *al.*, 2014). Zircon U–Pb age spectra from both Kidnappers and Rocky Hill pumices define  
34  
35 two modes at 1.1 and 1.0 Ma (Cooper *et al.*, 2014), inferred to represent two periods of  
36  
37 enhanced crystallization: first, in a common magmatic source (‘mush’) zone and second, in  
38  
39 the melt dominant bodies shortly prior to or interrupted by eruption, respectively. In the field,  
40  
41 the welded Rocky Hill ignimbrite forms crags and large boulder exposures (Blank, 1965), but  
42  
43 the Kidnappers deposits are only exposed in slip scars or road cuttings (Fig. 2). Although the  
44  
45 relevant contact is very rarely exposed, a time break between them is represented by erosional  
46  
47 reworking (but not soil development) of the top of the Kidnappers ignimbrite before  
48  
49 emplacement of the Rocky Hill ignimbrite (Fig. 2). In addition, the Rocky Hill ignimbrite is  
50  
51 sometimes observed to rest on older rocks from which the Kidnappers deposits have been  
52  
53 stripped. A period of years to decades between eruptions is thus inferred, based on  
54  
55  
56  
57  
58  
59  
60



1  
2  
3 observations that vegetation regrowth and incipient soil development on thick deposits under  
4  
5 New Zealand interglacial climate conditions could be expected to show up after about 50-100  
6  
7 years (e.g. Turner, 1928; Wilson, 1993). It is also inferred from glass compositions (Cooper *et*  
8  
9 *al.*, 2012) and field characteristics that the Kidnappers and Rocky Hill eruptions collectively  
10  
11 contributed to a composite deposit of primary and reworked volcanoclastic material that is  
12  
13 mapped widely throughout New Zealand as the Potaka Tephra (e.g., Shane, 1994; Carter *et*  
14  
15 *al.*, 2004; Alloway *et al.*, 2005).  
16  
17  
18  
19

## 20 21 **SAMPLING**

22  
23 Sampling of the Kidnappers fall deposit is discussed in Cooper *et al.* (2012). The majority of  
24  
25 Kidnappers pumices were sampled from pumice-rich, non-welded to sintered ignimbrite in a  
26  
27 quarry near Litchfield (38.108563°S, 175.836467°E), ~30 km from source, and others from a  
28  
29 farm pumice pit at 37.848558°S, 175.704651°E (Fig. 1). At both sites the ignimbrite is >10 m  
30  
31 thick, and contains pumices up to ~60 cm long. Kidnappers pumice is typically light grey-buff  
32  
33 in colour and contains discrete crystals (rather than crystal clots). Biotite is visibly present in  
34  
35 the majority of pumice clasts (although commonly weathered to a golden hydromica, which is  
36  
37 also obvious in the matrix), and pumices have a remarkably similar physical appearance  
38  
39 throughout the sampled ignimbrite.  
40  
41  
42

43  
44 Rocky Hill pumices were sampled from several locations of indurated to poorly  
45  
46 welded ignimbrite west of Mangakino within the Waipa Valley (Fig. 1), ~50 km from source,  
47  
48 at 38.437617°S, 175.363719°E and 38.404997°S, 175.343761°E. The eponymous Rocky Hill  
49  
50 type locality (Martin, 1961; Blank, 1965) was sampled at 38.381729°S, 175.308160°E and  
51  
52 38.382241°S, 175.308460°E. Most Rocky Hill pumice is glomeroporphyritic, with both  
53  
54 spherical crystal clots (commonly with brown glass selvages) and schlieren. Large (up to 4–  
55  
56 5 mm) amphibole phenocrysts are ubiquitous within Rocky Hill pumice and biotite, whilst  
57  
58  
59  
60

1  
2  
3 present, is sparse. The overall colour of pumice clasts varies from white (~70%) to dark grey  
4  
5 or brown (~30%), either with or without colour streaking.  
6  
7

## 8 9 10 **ANALYTICAL TECHNIQUES**

11 These are summarised here, with full details presented in the Supplementary Information.

12  
13 Analyses of reference standards used to demonstrate the overall reproducibility and accuracy  
14  
15 of the data are also presented in Supplementary Data.  
16

17  
18 Whole-rock major element analyses were carried out by X-ray fluorescence (XRF)  
19  
20 spectrometry using Philips PW2400 Sequential Wavelength Dispersive X-ray Fluorescence  
21  
22 Spectrometers at the University of Canterbury and Spectrachem Analytical (CRL Energy Ltd),  
23  
24 Lower Hutt. Whole-rock trace element analyses were carried out by solution inductively  
25  
26 coupled plasma mass spectrometry (ICP-MS), using an Agilent 7500cs ICP-MS at Victoria  
27  
28 University of Wellington.  
29  
30

31  
32 Backscattered electron (BSE) imaging and quantitative major element analyses of  
33  
34 glass and crystals were carried out using a JEOL JXA-8230 Superprobe at Victoria University  
35  
36 of Wellington. Minerals were analysed with a 15 kV accelerating voltage and a 12 nA focused  
37  
38 beam. Glass was analysed with a 15 kV accelerating voltage and an 8 nA beam current with a  
39  
40 defocused beam (20  $\mu\text{m}$ ). Trace element compositions of minerals and glass were determined  
41  
42 using a New Wave deep UV (193 nm solid state) laser ablation system coupled to a Agilent  
43  
44 7500cs ICP-MS at Victoria University of Wellington. All data were acquired as static spot  
45  
46 analyses with a beam diameter of 35  $\mu\text{m}$ , a laser repetition rate of 5 Hz, 85% laser power and  
47  
48 using helium as the carrier gas.  
49  
50

## 51 52 53 54 **RESULTS**

1  
2  
3 The Kidnappers fall matrix glass data were presented in Cooper *et al.* (2012) and are used  
4 here as a basis for comparison between pumice matrix glass data from the overlying  
5 ignimbrites. Establishing variations in pumice matrix glass chemistry is essential when  
6  
7 examining deposits such as the Kidnappers and Rocky Hill ignimbrites (where stratigraphic  
8 control is limited), so that crystal characteristics can be given additional context from the  
9 eruption deposits as a whole. All samples used for glass and crystal specific work in this study  
10 are listed in Fig. 3. All data used in this paper are presented in the supplementary electronic  
11 appendices.  
12  
13  
14  
15  
16  
17  
18  
19

### 20 21 22 23 **Whole-rock pumice compositions and glass chemistry**

24  
25 Pumices within the Kidnappers (and to a lesser extent the Rocky Hill) deposits are of very  
26 similar physical appearance. End-member pumice types were first determined on the basis of  
27 their whole-rock chemistry before representative clasts were chosen for glass and crystal-  
28 specific analyses (Fig. 3). All pumices analysed show some degree of secondary hydration,  
29 with loss-on-ignition values of up to 5 wt.%. All reported whole-rock and glass major element  
30 data were normalized to an anhydrous basis.  
31  
32  
33  
34  
35  
36  
37  
38  
39  
40

#### 41 *Kidnappers whole-rock pumice compositions*

42  
43 Whole-rock major element data cluster into three different groups based on SiO<sub>2</sub>, MgO, TiO<sub>2</sub>  
44 and CaO values (Fig. 4). The majority of Kidnappers ignimbrite (KI) pumices can therefore  
45 be divided into a dominant mid-SiO<sub>2</sub> type (KI-1: 72–74 wt.% SiO<sub>2</sub>) a high SiO<sub>2</sub> variant (KI-2:  
46 >74.5 wt.% SiO<sub>2</sub>) and a low SiO<sub>2</sub> variant (KI-3: <72 wt.% SiO<sub>2</sub>) (Tables 1 and 2). Trace  
47 elements Ni, Zn, Sr and Zr behave compatibly with increasing SiO<sub>2</sub>, whereas Ba and Rb  
48 behave incompatibly (Fig. 5), despite the abundance of biotite (for which both elements have  
49 Kd>1). Rb/Sr ratios within Kidnappers pumices range from 0.5 to 2.0 with elevated Rb/Sr  
50  
51  
52  
53  
54  
55  
56  
57  
58  
59  
60

1  
2  
3 values in pumices with the highest SiO<sub>2</sub> content (KI-2), consistent with the accumulation of  
4 plagioclase (Fig. 5). Eu/Eu\* ranges from 0.74–0.47 and decreases with decreasing Al<sub>2</sub>O<sub>3</sub>. The  
5 relative differences in the compositions of average Kidnappers matrix glass mirror those of  
6 the three whole-rock compositional groups (e.g. the low-SiO<sub>2</sub> whole-rock group corresponds  
7 to the low-SiO<sub>2</sub> glass group; Figs. 4 and 5). The variance of whole-rock pumice geochemistry  
8 is therefore influenced by the chemistry of the matrix glass i.e., the melt phase, in addition to  
9 reflecting the varying crystal cargo within each clast.  
10  
11  
12  
13  
14  
15  
16  
17  
18  
19

### 20 *Kidnappers pumice matrix glass compositions*

21  
22  
23 Eleven representative pumices covering all compositional groups from the Kidnappers  
24 ignimbrite were chosen for analysis of their matrix glass (Table 2). Tie-lines drawn between  
25 major element whole-rock and average matrix glass compositions have gradients in common  
26 with the overall whole-rock data, apart from K<sub>2</sub>O and Na<sub>2</sub>O which share a similar range in  
27 concentrations between whole-rock and glass (Fig. 4). Average matrix glass values range  
28 from 76.3–78.5 wt.% SiO<sub>2</sub>, 3.4–4.6 wt.% K<sub>2</sub>O and 0.6–1.3 wt.% CaO, and the overall  
29 eruption products are characterised by glass heterogeneity (Fig. 6). Matrix glass within  
30 individual pumice samples from KI-1 and KI-2 is homogeneous with respect to major  
31 elements, apart from FeO that spans a range beyond analytical uncertainty in all clasts.  
32  
33  
34 However, matrix glasses from the two KI-3 pumices (Fig. 3) have major element  
35 heterogeneity beyond analytical uncertainties (Fig. 6). Trace element heterogeneity at a single  
36 pumice scale is particularly evident in elements highly compatible in plagioclase and zircon  
37 such as Sr and Zr, respectively (Fig. 6).  
38  
39  
40  
41  
42  
43  
44  
45  
46  
47  
48  
49  
50  
51

52 In addition to the aforementioned elemental variability, there are compositional gaps  
53 in matrix glass across the suite of analysed pumice samples (Fig. 6). The glass chemistry  
54 shows clustering into three groups (best defined by plots of SiO<sub>2</sub> versus CaO, or Zr versus  
55  
56  
57  
58  
59  
60

1  
2  
3 Th), which correspond in almost all cases to the three groups evident from whole-rock  
4  
5 compositions (Fig. 4). Matrix glass from the KI-3 group shows separate, sub-parallel trends  
6  
7 when compared to the KI-1 and KI-2 groups on all major and trace element plots (Fig. 6).  
8  
9 Compositional fields covered by KI-1 and KI-2 glasses overlap and display the same slope in  
10  
11 terms of FeO and Rb/Sr (Fig. 6). The three matrix glass groups within the Kidnappers  
12  
13 ignimbrite pumices span a larger range than the three compositionally distinct glass types  
14  
15 found in the underlying fall deposit (Cooper *et al.*, 2012; Fig. 6). KI-1 overlaps both the KF-A  
16  
17 and KF-C (KF: fall deposit) compositional fields on all plots apart from SiO<sub>2</sub> vs. Mg, and  
18  
19 extends to higher trace element concentrations (Zr, Sr, La and Th) (Fig. 6). KI-2 overlaps KF-  
20  
21 B but extends to lower CaO and FeO concentrations as well as higher trace element  
22  
23 concentrations (Zr, Sr, La and Th). KI-3 does not overlap any of the Kidnappers fall groups,  
24  
25 and has significantly higher Al<sub>2</sub>O<sub>3</sub> concentrations (~13.4 wt.%), therefore representing a  
26  
27 magma apparently confined to later ignimbrite-forming stages of the Kidnappers eruption.  
28  
29  
30  
31  
32  
33

#### 34 *Rocky Hill whole-rock pumice compositions*

35  
36 In comparison to the Kidnappers whole-rock data, similar or larger (e.g., 65.0–76.2 wt.%  
37  
38 SiO<sub>2</sub>; 13.1–21.3 wt.% Al<sub>2</sub>O<sub>3</sub>; Fig. 7) major element variations are evident. K<sub>2</sub>O and Na<sub>2</sub>O  
39  
40 concentrations are generally lower and higher, respectively, in Rocky Hill pumices as  
41  
42 compared with Kidnappers pumices (Fig. 7). MgO concentrations are lower than those  
43  
44 observed in Kidnappers pumice samples (Fig. 7d) at the less-evolved end of the  
45  
46 compositional range (<71 wt.% SiO<sub>2</sub>). Unlike in the Kidnappers pumices, a continuity of  
47  
48 values is shown across the range in major element concentrations. Trace elements such as Ni,  
49  
50 Zn, Sr and Zr behave compatibly whereas Rb behaves incompatibly (Fig. 8). Ba is less  
51  
52 incompatible in the Rocky Hill than the Kidnappers samples (Fig. 8b). Rb/Sr ratios within  
53  
54 Rocky Hill pumice span a more restricted range and form a sub-parallel trend to the  
55  
56  
57  
58  
59  
60

1  
2  
3 Kidnappers compositional array when plotted against  $K_2O$  (Fig. 8).  $Eu/Eu^*$  ratios cover a  
4 smaller range (0.76–0.53) with a sharp decrease observed in pumices with  $<16$  wt.%  $Al_2O_3$   
5 (Fig. 8). Unlike the Kidnappers pumices, Y shows a more systematic relationship with  $Al_2O_3$   
6 (Fig. 8). Unlike the Kidnappers pumices, Y shows a more systematic relationship with  $Al_2O_3$   
7 with sub-parallel tie lines (Fig. 8f).  
8  
9

#### 14 *Rocky Hill pumice matrix glass compositions*

16  
17 Nine pumices from the Rocky Hill ignimbrite were chosen for matrix glass analysis on the  
18 basis of whole-rock composition (Fig. 3 and Tables 1 and 2). In general, tie-lines drawn  
19 between major element whole-rock and average matrix glass compositions have the same  
20 slopes (over similar lengths) as in the Kidnappers pumices, suggesting a similar degree of  
21 influence of the crystal content on pumice–glass relationships (Fig. 7). However, unlike in the  
22 Kidnappers pumices,  $K_2O$  tie-lines have positive and  $Na_2O$  tie-lines negative slopes with  
23 increasing  $SiO_2$  (Fig. 7). Rocky Hill matrix glass has higher Rb/Sr and  $K_2O$  values than its  
24 corresponding whole-rock value (Fig. 8) and displays less variation in major element  
25 chemistry than within the Kidnappers pumices (Fig. 9). The matrix glass within each pumice  
26 clast is homogeneous (within a 2 sd range) with respect to major elements, apart from FeO  
27 that ranges over 0.8 wt.% in each sample (Fig. 9). Two compositionally discrete matrix glass  
28 groups are present across the Rocky Hill (RH) pumice suite (best shown by Th vs. Zr: Fig.  
29 9f), and therefore clasts are grouped into ‘normal’ (RH-1; higher CaO and lower  $SiO_2$ ) and  
30 high- $SiO_2$  types (RH-2; lower CaO; Fig. 9a).  
31  
32  
33  
34  
35  
36  
37  
38  
39  
40  
41  
42  
43  
44  
45  
46  
47

48 Although these groups reflect distinct matrix glass compositions, associated whole-  
49 rock compositions show a large range with no compositional gaps. An arbitrary value of 74  
50 wt.%  $SiO_2$  is therefore used to distinguish the RH-1 and RH-2 pumices. As in the Kidnappers  
51 pumice glass, heterogeneity within Rocky Hill pumice glass is more pronounced in trace  
52 elements, particularly Zr and Sr (Fig. 9). Matrix glass major-element compositions overlie the  
53  
54  
55  
56  
57  
58  
59  
60

1  
2  
3 KI-1 and KI-2 Kidnappers glass groups. Trace element concentrations from the dominant RH-  
4  
5 1 type matrix glass overlie and extend the KI-1 Kidnappers glass group but do not show the  
6  
7 same trends as the KI-3 group. Pumice samples P2029 and P2030 from group RH-1 (Fig. 3)  
8  
9 have matrix glass Mg concentrations of <500 ppm, lower than any values within the  
10  
11 Kidnappers products (Fig. 9d). Trace element concentrations within group RH-2 overlap the  
12  
13 KI-2 group concentrations with respect to all elements. The two Rocky Hill glass groups form  
14  
15 sub-parallel trends on plots of Sr versus La and Zr versus Th with limited or no overlap (Fig.  
16  
17 9f, g).  
18  
19

20  
21 In many Rocky Hill pumices, particularly those of RH1 type, brown glass can be  
22  
23 observed sheathing crystal clots (Supplementary Fig. 1). The brown glass is less vesicular and  
24  
25 has thicker bubble walls than the matrix glass and is commonly compositionally distinct with,  
26  
27 on average, higher Na<sub>2</sub>O (5.1 wt.%) and CaO (1.2 wt.%) but lower K<sub>2</sub>O (1.4 wt.%), Rb (66  
28  
29 ppm), Ba (716 ppm) and Li (19 ppm) than the matrix glass (Supplementary Fig. 1).  
30  
31

### 32 33 34 **Mineral textures**

35  
36  
37 All pumices analysed from both ignimbrites and the Kidnappers fall deposit contain a  
38  
39 similar phenocryst assemblage, in decreasing order of abundance, of plagioclase + quartz +  
40  
41 orthopyroxene + hornblende + magnetite + ilmenite, plus accessory zircon and apatite. Of the  
42  
43 major phases, plagioclase (the dominant phase in all deposits) and orthopyroxene show  
44  
45 distinct textural characteristics (core-rim zoning) and the differences between compositional  
46  
47 groups and deposits are described below. Amphiboles do not display consistent textural core-  
48  
49 to-rim relationships or systematic zoning patterns and it was not feasible to characterise these  
50  
51 grains based on zoning visible in BSE imagery. However 10–20% of amphibole grains have  
52  
53 patchy recrystallised cores, which may represent an antecrystic or xenocrystic component.  
54  
55

56  
57 Within Rocky Hill pumices, amphibole occurs distinctively as euhedral crystals up to 4–5 mm  
58  
59  
60



1  
2  
3 long. Biotite appears part way through the Kidnappers fall deposit (in association with the  
4 KF-B-type glass: Cooper *et al.*, 2012), is present in nearly all Kidnappers pumices, but is  
5 sparse within Rocky Hill pumices. In all cases, however, the biotite displays no clear BSE  
6 zoning patterns, is generally weathered in the Kidnappers deposits and is not described further  
7 below. Quartz is present throughout the Kidnappers fall deposit and within all Kidnappers and  
8 Rocky Hill pumices. Cathodoluminescence (CL) imaging, which largely reflects the  
9 concentration of Ti, reveals oscillatory zoned quartz grains, often with multiple resorption  
10 zones. Samples chosen for crystal specific analyses from each deposit are listed in Fig. 3 and  
11 characteristics of the mineral phases are summarised in Table 3.  
12  
13  
14  
15  
16  
17  
18  
19  
20  
21  
22  
23

#### 24 *Kidnappers fall deposit mineral textures*

25  
26 Mineral characteristics and accompanying compositions in the Kidnappers fall deposit, briefly  
27 discussed in Cooper *et al.* (2012), are presented here in more detail to allow comparisons with  
28 the two ignimbrites. Samples were collected from the most proximal (~30 km from the  
29 caldera rim) and thickest (4.0 m) section known of the Kidnappers fall deposit. The mineral  
30 assemblage at each sampled horizon (apart from the KF-A-dominant base) reflects a mixture  
31 of material from at least two compositional groups. Thus, crystals from the fall deposit cannot  
32 always be definitively matched with the glass compositional groups. In particular, crystals  
33 from KF-C cannot be separated out from the other groups and so KF-C material is presented  
34 within the 'other' group below (Fig. 3).  
35  
36  
37  
38  
39  
40  
41  
42  
43  
44  
45  
46  
47

48         Around 25% of plagioclase at all stratigraphic heights displays patchy cores, often  
49 with a sieved texture (Tsuchiyama, 1985; Nelson & Montana, 1992). Plagioclase outermost  
50 rims at each analysed fall horizon (Fig. 3) are divided into three populations based on changes  
51 in BSE intensity between interior domains and outermost rims: light rims, dark rims, and non-  
52 distinct rims (that is, no tonal change, or fine oscillatory zoning to the outermost rim) (Fig. 10  
53  
54  
55  
56  
57  
58  
59  
60



1  
2  
3 and Supplementary Fig. 2). Grains displaying non-distinct rims are the dominant population  
4 (42–92%), and grains with light rims are subordinate at each stratigraphic horizon (3–12%).  
5  
6  
7 The most notable observation is the near absence of plagioclase with dark rims at the base of  
8  
9 the deposit (where glass type KF-A dominates). This suggests that dark rimmed grains are  
10  
11 characteristic of the KF-B compositional group which first appears ~1 m above the base of  
12  
13 the deposit.  
14  
15

16  
17 Orthopyroxene crystals at each analysed fall horizon (Fig. 3 and Supplementary Fig.  
18  
19 2) were classified into four populations based on simplified textural characteristics in BSE  
20  
21 imaging: (1, 2) grains in which interiors follow general (1) normal and (2) reverse zoning  
22  
23 patterns; (3) grains which are nominally unzoned; and (4) grains which have a patchy  
24  
25 appearance with no clear zoning relationships (Fig. 11 and Supplementary Fig. 2). Reversely  
26  
27 zoned grains are only present in any significant quantity (up to 25%) from just above the base  
28  
29 to ~2 m height in the fall deposit (Fig. 3 and Supplementary Fig. 2). The least evolved, KF-C  
30  
31 glass type is only found within the same horizons, suggesting that the reversely zoned grains  
32  
33 are associated with the KF-C melt.  
34  
35  
36  
37

### 38 *Kidnappers ignimbrite pumice mineral textures*

39  
40  
41 Around 20% of plagioclase across all pumice types display patchy (often sieve textured)  
42  
43 cores. Within KI-3 pumice, grains with light rims dominate (82%) and grains with dark rims  
44  
45 are absent, whereas in KI-2 pumice 42% of grains have prominent dark rims and only 2%  
46  
47 have light rims (Fig. 10). Within KI-1 pumice, non-distinct rims (66%) dominate over dark  
48  
49 (12%) or light (22%) rims. The dominance of light-rimmed plagioclase in KI-3 is distinctive  
50  
51 to the ignimbrite and not observed in the Kidnappers fall deposit (Supplementary Fig. 2).  
52  
53  
54  
55  
56  
57  
58  
59  
60

1  
2  
3 Quartz grains within a single KI-2 pumice were imaged by CL and were classified  
4  
5 into three groups: 80% of grains display dark rims, 7% light rims, and 13% have no  
6  
7 significant compositional change at the rim.  
8

9  
10 Orthopyroxene crystals were classified into the same four populations as within the  
11  
12 fall deposit. However, a further distinction can be made of crystals that show a dark exterior  
13  
14 zone (Fig. 11). This dark zone can be superimposed onto each of the four textural groups  
15  
16 described above and is either found within 100  $\mu\text{m}$  of the outermost crystal rim, or as the  
17  
18 outermost rim itself (Fig. 11). There is a high proportion (41%) of grains with a dark (high  
19  
20 Mg) exterior zone found in KI-3 pumice as compared with only 2% and 6%, in KI-2 and KI-3  
21  
22 pumice samples, respectively (Fig. 11). Systematic changes are observed in the proportions of  
23  
24 normally zoned, unzoned and reversely zoned types within each whole-rock compositional  
25  
26 group (Fig. 11). Patchy grains, interpreted to reflect significant recrystallization, do not follow  
27  
28 a particular trend and are generally subordinate to the other textural types.  
29  
30  
31  
32  
33

#### 34 *Rocky Hill ignimbrite pumice mineral textures*

35  
36 Broken and/or exploded plagioclase crystals are common within the crystal clots, the broken  
37  
38 crystals having textures like the 'phenoclasts' of Best and Christiansen (1997), surrounded by  
39  
40 palisade bubble textures (Rotella et al., 2015). The fragments of exploded crystals are  
41  
42 irregularly shaped, resembling a jigsaw, and held together by glass with large vesicles and  
43  
44 thick bubble walls (Supplementary Fig. 1). A greater proportion (~30%) of Rocky Hill  
45  
46 plagioclase displays patchy or sieve textured cores when compared to the Kidnappers.  
47  
48 Plagioclase rim-type proportions are closely matched between the RH-1 and KI-1, and RH-2  
49  
50 and KI-2 groups (Fig. 10). No Rocky Hill pumices contain plagioclase where light rims  
51  
52 dominate, in contrast to the KI-3 group (Fig. 10).  
53  
54  
55  
56  
57  
58  
59  
60

1  
2  
3 Quartz grains within a single RH-1 pumice were imaged by CL. In contrast to the  
4  
5 Kidnappers, grains with light rims dominate (61%) over those with dark rims (19.5%) and  
6  
7 those showing no change (19.5%).  
8

9  
10 Orthopyroxene crystals with normal zoning are 55% of the orthopyroxene population  
11  
12 in RH-1 pumice, increasing to 94% in RH-2 pumice. Concurrently, unzoned grains decrease  
13  
14 from 38% to 5%, and reversely zoned grains decrease from 7% to 1%, respectively (Fig. 11).  
15  
16 Grains with a dark (high Mg) exterior zone decrease in abundance from 13% in RH-1  
17  
18 pumices to 1% in RH-2 pumices, parallel to the changes observed between KI-1 to KI-2  
19  
20 pumices in the Kidnappers ignimbrite (Fig. 11).  
21  
22  
23  
24

## 25 **Mineral chemistry**

26  
27 Samples chosen for mineral chemical analysis are listed in Fig. 2 and the ranges in  
28  
29 compositions of crystal phases from each of the studied deposits is summarised in Table 4.  
30  
31 Biotite proved to be too weathered for reliable major element analysis by EPMA. Magnetite  
32  
33 and ilmenite pairs occur as free crystals in the matrix and also as inclusions within  
34  
35 orthopyroxene and, to a lesser extent, amphibole. Fe–Ti oxide pairs included within same host  
36  
37 orthopyroxene were targeted to ensure textural equilibrium for use in temperature estimates.  
38  
39  
40  
41  
42  
43

### 44 *Kidnappers fall deposit mineral chemistry*

45  
46 Plagioclase compositions from the Kidnappers fall deposit range from An<sub>68</sub> to An<sub>24</sub> and Or<sub>0.8</sub>  
47  
48 to Or<sub>4.8</sub> (Fig. 12a). Plagioclase core compositions show considerable overlap, even from  
49  
50 horizons where KF-A or KF-B material separately dominate (Tables 1 and 5), and range over  
51  
52 An<sub>64–28</sub> and Or<sub>3.90–0.85</sub>. Plagioclase rim values, however, cover only ~10 mol.% An, compared  
53  
54 with a ~30 mol.% range for cores at each stratigraphic height (Fig. 12a). Minimum  
55  
56 plagioclase rim values change with stratigraphic height from ~An<sub>35</sub> at the base to ~An<sub>26</sub> at the  
57  
58  
59  
60

1  
2  
3 top of the deposit (Fig. 12a). Plagioclase rim compositions throughout the deposit display a  
4  
5 bimodal distribution at  $An_{32.5} Or_{3.75}$  and  $An_{37.5} Or_{2.75}$  (Supplementary Fig. 3), although where  
6  
7 the KF-A glass is dominant only the  $An_{37.5} Or_{2.75}$  mode occurs, with KF-A glass selvages  
8  
9 (Cooper *et al.*, 2012). Broader ranges and bimodal distributions in major and trace element  
10  
11 compositions of rims are found in samples where glass types KF-B and KF-C are also present  
12  
13 as shards (Supplementary Fig. 3). The lower An (and Mg) plagioclase mode at  $An_{32.5} Or_{3.75}$   
14  
15 (Fig. 13) is therefore associated with the dominant KF-B glass but there is no specific  
16  
17 plagioclase composition that can be definitively linked to KF-C glass (Cooper *et al.*, 2012).  
18  
19 Core-to-rim variations in Ba (increase) and Mg (decrease) are associated with plagioclase  
20  
21 from the KF-B group, whereas grains from the KF-A group have no core-to-rim  
22  
23 compositional shifts (Fig. 13).  
24  
25  
26

27  
28 Orthopyroxene compositions range between  $En_{65-42}$  and  $Wo_{5.6-1.2}$  (Fig. 12b). The  
29  
30 majority of cores are between  $\sim En_{43-50}$  and  $Wo_{1.75-3.50}$  with a scatter to  $En_{65}$  and  $Wo_{1.2-5.6}$  (Fig.  
31  
32 14). Orthopyroxene cores from horizons where KF-A and KF-B glass compositions  
33  
34 separately dominate show considerable compositional overlap, with a bimodal distribution at  
35  
36  $\sim Wo_{2.2}$  and  $\sim Wo_{2.5}$  (Supplementary Fig. 4). Grains from horizons where the KF-B glass  
37  
38 dominates show a unimodal distribution defining a peak at  $Wo_{2.5}$ . Orthopyroxene rims, in  
39  
40 general, show a tight compositional range between  $\sim En_{42-48}$  and  $Wo_{1.6-3.0}$  (Fig. 14), but also  
41  
42 have a bimodal distribution with peaks at  $Wo_{2.2}$  and  $Wo_{1.8}$  (Supplementary Fig. 4). A  
43  
44 significant core-to-rim drop in Ca ( $Wo_{2.5-1.8}$ ) is displayed in  $\sim 40\%$  of grains from KF-B-  
45  
46 dominated horizons (Supplementary Fig. 4). Significant core-to-rim shifts in chemistry, in  
47  
48 contrast, are absent in grains from horizons where KF-A glass dominates. Orthopyroxenes  
49  
50 from the KF-A-dominant horizons have a more restricted range in trace element  
51  
52 concentrations and, in general, slightly higher Co (50–57 ppm) than in other fall samples  
53  
54 where more than one glass group occurs (Fig. 14).  
55  
56  
57  
58  
59  
60

1  
2  
3 Amphibole rims and the majority of cores (251 analyses) plot in the field of  
4  
5 magnesianhornblendes: of the other cores, 14 are tschermakitic pargasites and 4 are  
6  
7 magnesianhastingsites (terminology of Leake *et al.*, 2004). Amphibole core and intermediate  
8  
9 domain compositions cover the whole of the compositional range ( $Al^T$  1–2) but rims have a  
10  
11 smaller range ( $Al^T$  1.05–1.62). Average core compositions from lower (KF-A glass  
12  
13 dominated) and upper (KF-B glass dominated) parts of the fall deposit are very similar (Table  
14  
15 4). No consistent core-to-rim shifts in  $Al^T$  are present in any samples, but a number of grains  
16  
17 associated with KF-B material show a core-to-rim decrease in  $TiO_2$  (Supplementary Fig. 5).  
18  
19 When  $Al^T$  is plotted against other site-specific cation proportions such as  $(Na+K)^A$ , a slight  
20  
21 inflection in the data array is observed at  $Al^T \sim 1.2$  (Fig. 15). Inflections are also visible when  
22  
23 Mn and Zr are plotted against amphibole  $Eu/Eu^*$  (total range from 0.7 to 0.2) (Fig. 15), used  
24  
25 here as a quantitative measure of the degree of evolution of the host melt (Allan *et al.*, 2013).  
26  
27 Cores with  $Eu/Eu^* > 0.3$  do not show a systematic trend in trace element concentrations,  
28  
29 whereas in contrast, cores and rims with  $Eu/Eu^* < 0.3$  show sharp increases in Mn and  
30  
31 decreases in Zr with decreasing  $Eu/Eu^*$  (Fig. 15).  
32  
33  
34  
35

36 Magnetite compositions fall in the overall range of  $X_{usp0.27-0.46}$  and show a bimodal  
37  
38 distribution with respect to  $Al_2O_3$ . Ilmenite has a compositional range of  $X_{ilm0.87-0.93}$  and  
39  
40 shows a bimodal distribution with respect to MnO (Cooper *et al.*, 2012).  
41  
42  
43  
44

#### 45 *Kidnappers ignimbrite pumice mineral chemistry*

46  
47 Plagioclase cores from pumices in each of the whole-rock compositional groups have similar  
48  
49 mean compositions (Table 4). Plagioclase rim compositions cluster into three populations,  
50  
51 based on either average or minimum An values, that correspond to the three whole-rock  
52  
53 compositional groups (Fig. 12d; Table 4). Plagioclases from KI-3 pumices show core-to-rim  
54  
55 increases in An and decreases in Or proportions (Supplementary Fig. 3), reflected in the  
56  
57  
58  
59  
60

1  
2  
3 dominance (82%) within this group of BSE-light rims (Fig. 10). The opposite is the case for  
4  
5 plagioclase from the KI-2 samples. Plagioclase trace elements display parallel patterns to the  
6  
7 major elements, with KI-3 grains showing core-to-rim increases in Mg and Sr and a decrease  
8  
9 in Ba, the reverse of the trends in KI-1 and KI-2 grains (Fig. 13). Clear differences in Mg, Ba  
10  
11 and Sr concentrations are present between KI-3, versus KI-1 and KI-2 plagioclase rims (Fig.  
12  
13 13).

14  
15  
16 Orthopyroxene compositions range from  $En_{68-41}$  and  $Wo_{5.2-1.1}$  (Fig. 12e). Each of the  
17  
18 pumice compositional groups have very similar mean core compositions, but mean rim  
19  
20 compositions vary systematically with the whole-rock and glass compositions (Fig. 14; Table  
21  
22 4). Rim compositions range by  $\sim 10$  mol.% En within KI-3 pumices, but by only  $\sim 5$  mol.%  
23  
24 within KI-1 and KI-2 pumices (Fig. 12e). A core-to-rim drop in mean CaO of 1.2 to 1.0 wt.%  
25  
26 ( $Wo_{2.5-2.0}$ ) is found in crystals within the KI-2 group, whereas  $\sim 40\%$  of crystals from the KI-3  
27  
28 group display a rimward rise in Ca (Fig. 14). Crystal rim trace element concentrations  
29  
30 typically plot into distinct fields that can be linked to the whole-rock composition of their host  
31  
32 pumice (Fig. 14). Rims of grains from KI-1 and KI-2 pumices form parallel trends and  
33  
34 discrete groups on a plot of  $TiO_2$  versus Y (Fig. 14), with grains from the KI-3 pumices  
35  
36 forming an extension of the KI-1 field back to higher concentrations.  
37  
38  
39

40  
41 Amphibole cores plot in the fields of magnesiohornblende and tschermakite–pargasite  
42  
43 and outermost rims are all in the magnesiohornblende field. Total amphibole compositions  
44  
45 range from  $Al^T = 0.99$  to 1.94 (Fig. 12f). Amphibole core compositions have a large scatter  
46  
47 ( $Al^T$  1.02–1.88) but mean  $Al^T$  values are very similar between whole-rock compositional  
48  
49 groups (Fig. 11f; Table 4). Rim  $Al^T$  values (Table 4), along with other elemental  
50  
51 concentrations such as  $TiO_2$  (Supplementary Fig. 5), covary with the host pumice  
52  
53 compositional group. KI-3 amphiboles show a significant core-to-rim increase in  $Al^T$  (1.31-  
54  
55 1.42) whereas KI-2 amphiboles show the opposite (1.28-1.15) (Fig. 15; Table 4).  $TiO_2$   
56  
57  
58  
59  
60

1  
2  
3 concentrations in amphibole cores are similar in each group (~1.6 wt.%), but rim  
4  
5 compositions are distinct in each group, i.e., ~1.2 (KI-2), ~1.6 (KH-1) and ~2.0 wt.% TiO<sub>2</sub>  
6  
7 (KH-3) (Supplementary Fig. 5). When Al<sup>T</sup> is plotted against other site-specific cation  
8  
9 proportions such as (Na + K)<sup>A</sup> and Mg/(Mg + Fe<sup>3+</sup>), an inflection in data is observed at Al<sup>T</sup> =  
10  
11 ~1.2 (Fig. 15). This inflection is more prominent in amphiboles from the ignimbrite pumices  
12  
13 than those in the Kidnappers fall deposit and Rocky Hill ignimbrite. A sharp increase in Mn  
14  
15 and decrease in Zr concentrations occurs with the change in Eu/Eu\* from 0.3 to 0.2 (Fig. 15).

16  
17 Magnetite (total range of Usp<sub>24-51</sub>) and ilmenite (Ilm<sub>87-89</sub>) occur as inclusions in a high  
18  
19 proportion of orthopyroxenes, and to a lesser extent in amphiboles. Magnetites from the KI-3  
20  
21 pumices extend to higher TiO<sub>2</sub>, and have a mean of Usp<sub>35</sub>, compared to Usp<sub>31</sub> in the KI-1 and  
22  
23 KI-2 pumices, although ilmenite compositions are very similar between groups (Ilm<sub>87-89</sub>)  
24  
25 (Table 4).  
26  
27  
28  
29  
30  
31

### 32 *Rocky Hill ignimbrite pumice mineral chemistry*

33  
34 Plagioclase cores have similar mean compositions in RH-1 and RH-2 pumices (Table 4).  
35  
36 Mean rim compositions from RH-1 plagioclase are almost identical to their associated cores  
37  
38 (An<sub>36</sub> Or<sub>2.4</sub>), but RH-2 rims show more evolved compositions (An<sub>30</sub> Or<sub>3.3</sub>; Table 4). The lower  
39  
40 An rim compositions correspond to the higher proportion of dark BSE rims within this group  
41  
42 (Fig. 11). All core-to-rim trends recorded in grains from RH-1 and RH-2 groups are very  
43  
44 similar to trends in plagioclase in the KI-1 and KI-2 pumice groups, respectively (Figs. 11 and  
45  
46 13). RH-2 type grains display core-to-rim decreases in Mg and Sr and increases in Ba,  
47  
48 whereas cores from RH-1-type grains have concentrations both higher and lower than their  
49  
50 associated rims (Fig. 13). Clear differences in Mg, Ba and Sr concentrations characterise RH-  
51  
52 1 and RH-2 rims, corresponding with the discrete An modes (Fig. 13).  
53  
54  
55  
56  
57  
58  
59  
60



1  
2  
3 Orthopyroxene compositions range from  $En_{63-42}$  and  $Wo_{4.38-1.46}$  (Fig. 12h). Rim  
4  
5 compositions within each pumice range by  $<5$  mol.% En. (Fig. 12h) and rims from the two  
6  
7 pumice groups have the same mean En values. Orthopyroxene rims from RH-2 pumices show  
8  
9 a tight clustering around  $Wo_{1.6}$ , compared with  $Wo_{2.4}$  in RH-1 grains (Fig. 14; Table 4). A  
10  
11 consistent core-to-rim drop in Ca (Wo component) is reflected in the dominance of normal  
12  
13 zoned orthopyroxenes within the RH-2 group (Fig. 11). Trace element concentrations in  
14  
15 crystal rims from the RH-1 and RH-2 groups fall into distinct clusters, which overlie rim  
16  
17 compositions of the KI-1 and KI-2 groups, respectively (Fig. 14). The trend towards higher  
18  
19 elemental concentrations observed in crystals from the KI-3 group is not seen in the Rocky  
20  
21 Hill crystals (Fig. 14).  
22  
23  
24

25 Rocky Hill amphiboles are commonly complexly zoned, with cores plotting in the  
26  
27 field of magnesiohornblende and tschermakite–pargasite, and rims in the magnesiohornblende  
28  
29 field. Core compositions span the total range recorded ( $Al^T = 0.97-1.99$ ) and mean  $Al^T$  values  
30  
31 are almost identical between whole-rock groups (Fig. 12i; Table 4). Mean RH-1 rim  
32  
33 compositions are similar to associated cores, but have significant lower  $Al^T$  values within the  
34  
35 RH-2 group (Table 4). RH-1 amphiboles have both cores and rims with modes close to  $\sim 1.6$   
36  
37 wt.%  $TiO_2$ , whereas in RH-2 amphiboles the cores (mode  $\sim 1.5$  wt.%) and rims (mode  $\sim 1.2$   
38  
39 wt.%  $TiO_2$ ) are different (Supplementary Fig. 5). The core-to-rim trends observed within  
40  
41 Rocky Hill amphiboles from the RH-1 and RH-2 pumice groups are, as with other mineral  
42  
43 phases, closely similar to those within KI-1 and KI-2 groups, respectively (Supplementary  
44  
45 Fig. 5).  
46  
47  
48

49 Magnetite inclusions within orthopyroxene are in the range of  $Usp_{23-50}$  and ilmenite  
50  
51 inclusions fall between  $Ilm_{80-91}$ . Mean magnetite and ilmenite compositions do not vary  
52  
53 significantly between pumice compositional groups and are between  $Usp_{29-32}$  and  $Ilm_{87-88}$   
54  
55 (Table 4).  
56  
57  
58  
59  
60



## Model temperatures and pressures

Here, we present (Table 5) and compare estimates of intensive variables for the Kidnappers and Rocky Hill samples, obtained using amphibole (Ridolfi *et al.*, 2010 (R2010, below); Putirka, 2016), Fe–Ti oxides (Ghiorso & Evans, 2008), and plagioclase–melt and orthopyroxene–melt (Putirka, 2008) models.

### *Amphibole model temperature and pressure estimates*

*Kidnappers fall deposit:* Amphibole cores from horizons separately dominated by KF-A and KF-B glass compositions have overlapping ranges in R2010 model temperatures and rims with a total range between 770 and 900 °C (Fig. 16). Amphibole core R2010 model pressures are closely similar in samples from any stratigraphic position in the fall deposit. Rims cover a smaller model pressure range than cores, from 80 to 160 MPa in both KF-A- and KF-B-dominated fall material (Fig. 16).

*Kidnappers ignimbrite:* Amphibole core R2010 model temperatures show little difference between samples, with a peak at 790–800 °C and a tail to ~920 °C (Fig. 16). Rim model temperatures from crystals in both the KI-1 and KI-2 pumice groups have broad peaks between 780–800 °C, similar to associated core temperatures. In contrast, amphiboles from the KI-3 pumice group show core-to-rim temperature increases, with peak rim model temperatures of 810–840 °C. This pattern is reflected in R2010 model pressures, with cores displaying peak pressures of 90–130 MPa and a tail to ~270 MPa (Fig. 16). Rim R2010 model pressures from KI-1 and KI-2 pumice groups are tightly clustered, similar to associated core pressures (80–130 MPa) but without the tail to higher pressures, whereas rim model pressures from the KI-3 group are higher (130–170 MPa) than in their respective cores. The values for

1  
2  
3 R2010 model temperature and pressure from the KI-1 and KI-2 groups are similar to those in  
4  
5 the fall deposit, but the KI-3 samples have a higher temperatures and pressures (Fig. 16).  
6

7 *Rocky Hill ignimbrite*: Amphibole core R2010 model temperatures are similar  
8  
9 between pumice compositional groups, with the majority between 770 and 820 °C and a tail  
10  
11 to ~920 °C (Fig. 16). Rim R2010 model temperatures from the RH-1 amphiboles are  
12  
13 indistinguishable from those of the cores (both 780–820 °C). In contrast, RH-2 rim  
14  
15 temperatures are cooler (760–780 °C) and the core-to-rim decrease (~20 °C) is greater than in  
16  
17 the otherwise similar high-SiO<sub>2</sub> KI-2 group. R2010 model pressures from cores display a  
18  
19 narrow range between 90 and 120 MPa with a minor tail to ~270 MPa (Fig. 16). R2010 model  
20  
21 pressures from the rims are similar to those recorded in the cores (RH-1: 90–140 MPa; RH-2:  
22  
23 80–120 MPa) but without the tail to higher pressures.  
24  
25  
26

27 As a test for validation and consistency, R2010 model temperature and pressure  
28  
29 estimates are compared to those of Putirka (2016). The pressure independent model (equation  
30  
31 5 of Putirka, 2016) returns average compositional group core and rim temperatures that are  
32  
33 10-20 °C higher than those of R2010 (Table 5). The amphibole-liquid model (equation 9 of  
34  
35 Putirka, 2016) returns average compositional group core and rim temperatures between 10 °C  
36  
37 lower and 15 °C higher than those of R2010. The models of Putirka (2016) thus yield the  
38  
39 same relative core to rim temperature shifts, and compositional group differences as do the  
40  
41 R2010 models (Table 5). In contrast, the average pressures estimated using the Putirka (2016)  
42  
43 model (his equation 7a) are significantly higher (290-400 MPa) than those of R2010. Relative  
44  
45 core to rim relationships in pressure are not the same as those using R2010 (Table 5). The  
46  
47 Putirka (2016) equation 7a model uses liquid compositions (including H<sub>2</sub>O) in equilibrium  
48  
49 with amphibole. Average water concentrations (5.2-5.3 wt. %) for this purpose were  
50  
51  
52  
53  
54  
55  
56  
57  
58  
59  
60 independently calculated using the plagioclase hygrometer of Waters & Lange (2015).

1  
2  
3 As another test for consistency, R2010 model pressure estimates were used in turn to  
4 estimate temperatures with the plagioclase–hornblende thermometer of Holland & Blundy  
5 (1994). The resulting calculated model temperatures cover a larger range than the Ridolfi *et*  
6 *al.* (2010) temperatures (typically 100 °C range in each pumice), but mean temperatures from  
7 each model are within 20 °C of each other. Therefore, amphibole temperature and pressure  
8 estimates using Ridolfi *et al.* (2010) appear to be at least internally consistent with  
9 temperature estimates using the method of Holland & Blundy (1994).  
10  
11  
12  
13  
14  
15  
16  
17  
18  
19

#### 20 *Fe–Ti oxide temperature and $fO_2$ estimates*

21 Magnetite and ilmenite pairs included within the same host orthopyroxene and, but to a lesser  
22 extent, amphibole were targeted to ensure textural equilibrium (Blundy *et al.*, 2006). All  
23 oxide pairs used passed the equilibrium test of Bacon & Hirschmann (1988).  
24  
25  
26  
27  
28  
29

30 *Kidnappers fall deposit:* The total suite of estimates shows a bimodal distribution  
31 throughout the fall deposit (Fig. 17), and mean values vary between KF-A dominated  
32 horizons (810 °C) and KF-B dominated horizons (785 °C) (Table 5). The temperature ranges  
33 recorded in samples from horizons dominated by the KF-A and KF-B glass types are similar  
34 to the ranges from the KI-1 and KI-2 ignimbrite groups (Fig. 17). Data from all other horizons  
35 display bimodality. Log  $fO_2$  estimates fall on the NNO buffer curve and cover a range from –  
36 11.6 to –15.5 (Fig. 17), whereas mean values vary slightly with stratigraphic height (Table 5).  
37  
38  
39  
40  
41  
42  
43  
44

45 *Kidnappers ignimbrite:* The oxide pairs show a broader range in model temperatures  
46 (760–970 °C) than in the fall deposit. The temperature ranges within each compositional  
47 group, and in each individual pumice are larger than the range in amphibole rim model  
48 temperatures, but are within the respective uncertainties. Log  $fO_2$  estimates fall on the NNO  
49 buffer curve and cover a range from –10.8 to –14.9 (Fig. 17), with mean values also varying  
50 with compositional group (Table 5).  
51  
52  
53  
54  
55  
56  
57  
58  
59  
60

1  
2  
3 *Rocky Hill ignimbrite*: Model temperature estimates cover a similar range to the  
4  
5 Kidnappers ignimbrite of 750–960 °C and also show variations in mean values with whole-  
6  
7 rock group (Fig. 17; Table 5). Temperature and  $fO_2$  estimates from RH-1 and RH-2 pumices  
8  
9 are very similar to those in the KI-1 and KI-2 groups, respectively.  
10  
11

12  
13  
14 *Plagioclase–melt and orthopyroxene–melt temperature estimates*  
15

16  
17 Due to the presence of multiple melt compositions within Mangakino eruptives (Cooper *et al.*,  
18  
19 2012), it was considered important to use melt (glass) compositions that are directly  
20  
21 associated (within a common pumice) with crystal populations. Only crystal rims were used  
22  
23 so as to maximise the likelihood of equilibrium between crystals and melt. Due to the  
24  
25 challenges in matching loose crystals to glass shard compositional groups within the  
26  
27 Kidnappers fall deposit, plagioclase–melt and orthopyroxene–melt temperatures were  
28  
29 estimated from ignimbrite pumices only.  
30  
31

32  
33 The plagioclase–melt thermometer of Putirka (2008) is strongly sensitive to the H<sub>2</sub>O  
34  
35 content of the melt, which was estimated for each pumice using the plagioclase hygrometer of  
36  
37 Waters & Lange (2015). Average model water contents range from 4.8–6.7 wt. % H<sub>2</sub>O in  
38  
39 Kidnappers pumice and 5.1–5.9 wt. % H<sub>2</sub>O in Rocky Hill pumices. All model water content  
40  
41 estimates from amphibole rims using Ridolfi *et al.* (2010) (5.2–5.7 wt.% H<sub>2</sub>O) are within  
42  
43 range of the Waters & Lange (2015) estimates. Putirka (2008) model temperatures from  
44  
45 Kidnappers plagioclase range from 745–840 °C (Supplementary Fig. 6), with the mean values  
46  
47 from each compositional group being distinctive (KI-1 = 780 °C, KI-2 = 750 °C, KI-3 = 820  
48  
49 °C; Table 5). Model temperatures for the Rocky Hill plagioclase are more restricted, and can  
50  
51 be grouped into two tight modes representing grains from RH-1 (mean of 785 °C) and RH-2  
52  
53 (mean of 760 °C; Supplementary Fig. 6; Table 5).  
54  
55  
56  
57  
58  
59  
60

1  
2  
3 Model orthopyroxene–melt temperatures using the methods of Putirka (2008) in the  
4 Kidnappers KI-2 group crystals display multiple modes from 720–770 °C (750 °C mean),  
5 whereas KI-1 group crystals range between 740 and 800 °C (775 °C mean), and KI-3 group  
6 crystals have a broad distribution with a mean of 795 °C (Supplementary Fig. 6). In contrast,  
7 50% of Rocky Hill pumice samples contain orthopyroxene that is not in equilibrium with the  
8 melt (using the criteria of Putirka, 2008). For example, two samples of RH-1 (P2029, P2030:  
9 Fig. 3) and one of RH-2 (P2046) pumices have significantly lower matrix glass Mg  
10 concentrations (Fig. 9) and melt–rim pairs are far from equilibrium. Where crystal rims are in  
11 equilibrium with the melt, mean model temperatures are 770 °C in the RH-1 group and 760  
12 °C in the RH-2 group (Supplementary Fig. 6; Table 5).  
13  
14  
15  
16  
17  
18  
19  
20  
21  
22  
23  
24  
25  
26

## 27 DISCUSSION

### 28 Reliability of geothermobarometry estimates

29  
30  
31  
32  
33 Published uncertainties for the different thermobarometers are large ( $\pm 22$ – $44$  °C; see Table 5),  
34 although by using the averages of large datasets, the relative differences (as opposed to  
35 absolute values) between calculated temperatures will have smaller uncertainties. Much of the  
36 variation in temperature and pressure estimates from the Kidnappers and Rocky Hill samples  
37 is within each model uncertainty. The relative differences in model temperatures reported  
38 above between pumice compositional groups remain consistent, however, whether the  
39 estimates use amphibole, Fe–Ti oxides, plagioclase–melt or orthopyroxene–melt methods.  
40  
41 Here we consider some of the disparities in geothermobarometry estimates and their possible  
42 causes.  
43  
44  
45  
46  
47  
48  
49  
50  
51

52  
53 The Al-in-amphibole barometer of Ridolfi *et al.* (2010) is based on simple regression  
54 of  $Al_{tot}$  from selected experiments at a known pressure and therefore all variability in Al  
55 content is expressed as a pressure change. Therefore, in magmatic systems involving multiple,  
56  
57  
58  
59  
60

1  
2  
3 evolving and interacting melts, changes in the Al concentration of the melt can increase  
4  
5 amphibole  $Al_{tot}$  values without any accompanying change in pressure (e.g., Coombs *et al.*,  
6  
7 2013; Erdmann *et al.*, 2014; Kiss *et al.*, 2014; Putirka, 2016). However, in New Zealand  
8  
9 rhyolites (Allan *et al.*, 2012; Cooper & Wilson, 2014; Barker *et al.*, 2015), the Ridolfi *et al.*  
10  
11 (2010) barometer yields geologically reasonable estimates, consistent with evidence from  
12  
13 volatile studies (Dunbar *et al.*, 1989; Liu *et al.*, 2006) and model estimates using the other  
14  
15 mineral phases. Magmas at Mangakino are plagioclase saturated and Al-buffered, and  
16  
17 therefore, variations in the Al content of amphibole, which are not interpreted to be the result  
18  
19 of mixing on the basis that other compositional parameters do not change, have the potential  
20  
21 to be controlled by pressure (although with large uncertainties: Putirka, 2016). There are no  
22  
23 significant differences in the Eu/Eu\* values in glass and amphiboles from KI-2 and RH-2  
24  
25 pumices to suggest that magma mixing caused the amphibole  $Al_{tot}$  trends. Thus the core-to-  
26  
27 rim decreases in  $Al_{tot}$  in the KH-2 and RH-2 amphiboles are interpreted to reflect changes in  
28  
29 pressure. Within the Kidnappers KI-3 group pumices, however, amphiboles record core-to-  
30  
31 rim increases in both model temperature (~40 °C) and pressure (~40 MPa; Fig. 16). The  
32  
33 former can be explained by an input of hotter, less evolved magma, consistent with core-to-  
34  
35 rim compositional changes within the other phases. We thus interpret the rise in model  
36  
37 pressures as an artifact of the changes in melt Al concentrations, driving increased amphibole  
38  
39  $Al_{tot}$  values.

40  
41  
42  
43  
44  
45 The average pressures estimated using the Putirka (2016) model (equation 7a) are  
46  
47 around three times higher, and relative core to rim relationships in pressure are not coherent  
48  
49 when compared to the model pressures of Ridolfi *et al.* (2010). These disparities highlight the  
50  
51 difficulties in estimating the pressures of amphiboles at shallow crustal depths and negates the  
52  
53 use of interpreting absolute pressure values. The Putirka (2016) model uses global amphibole-  
54  
55 liquid experimental data and is water dependent. Therefore amphibole cores, which are likely  
56  
57  
58  
59  
60

1  
2  
3 not in equilibrium with the matrix glass may well return erroneous values. The Fe-Mg  
4  
5 exchange coefficient  $K_D(\text{Fe-Mg})^{\text{amph-liq}}$  can be used as a test for amphibole-liquid equilibrium  
6  
7 (Putirka, 2016). 75 % of all amphibole analyses from Kidnappers pumice fall outside the  
8  
9 suggested range ( $K_D=0.28\pm 0.11$ ) and therefore are not suitable for use with the amphibole-  
10  
11 melt models of Putirka (2016).  
12

13  
14 There is a larger range in Fe–Ti oxide model temperatures from each compositional  
15  
16 group when compared with amphibole. This may be a consequence of Fe–Ti oxides  
17  
18 responding more rapidly to changes in temperature immediately prior to eruption, over  
19  
20 timescales that are too short for the re-equilibration of amphibole compositions (e.g. De  
21  
22 Angelis *et al.*, 2013). Alternatively, these differences may reflect the relatively large Fe–Ti  
23  
24 oxide model uncertainties (Blundy & Cashman, 2008), coupled with a high number of  
25  
26 modeled equilibrium pairs, resulting in a large spread in temperatures.  
27  
28

29  
30 The ranges in plagioclase–liquid and orthopyroxene–liquid model temperatures are  
31  
32 smaller in both eruption deposits when compared to other thermometry techniques. In part  
33  
34 this is due to the use of only crystal rims (not cores), but is also an artifact of the thermometry  
35  
36 models, which are strongly reliant on melt and H<sub>2</sub>O concentrations. The use of average matrix  
37  
38 glass values and average modeled H<sub>2</sub>O concentrations reduces the number of variables in  
39  
40 temperature calculations, thus reducing the range of modeled temperatures.  
41  
42  
43  
44

#### 45 **Melt evolution processes from amphibole signatures**

46  
47 Inflections observed within amphibole major- and trace-element data with increasing  
48  
49 evolution of the bulk-pumice compositions can be linked to changes affecting the overall  
50  
51 melt-dominant bodies (Fig. 15). The sharp drop in  $(\text{Na} + \text{K})^{\text{A}}$  with decreasing  $\text{Al}^{\text{T}}$  (at  $\sim 1.2$ ),  
52  
53 particularly evident in KI-2 type rims (Fig. 15), is inferred to reflect continued plagioclase  
54  
55 and/or biotite crystallisation (removal of Na + K from the melt). Both Kidnappers and Rocky  
56  
57  
58  
59  
60



1  
2  
3 Hill amphibole  $\text{Mg}/(\text{Mg} + \text{Fe}^{3+})$  and Mn values increase with decreasing  $\text{Al}^{\text{T}}$  (at  $<1.2$ ), which  
4 is interpreted to reflect orthopyroxene instability (cf. Allan *et al.*, 2013). Inflections in  
5  
6  
7 amphibole Mn and Zn concentrations with both  $\text{Eu}/\text{Eu}^*$  and model pressures are also  
8  
9  
10 consistent with orthopyroxene instability in the more evolved ( $\text{Eu}/\text{Eu}^* < 0.3$ ), inferred lower  
11 (model) pressure melts (Fig. 15). The breakdown of orthopyroxene, preferentially enriched in  
12  
13 Mg, Mn and Zn when compared to amphibole (Supplementary data), increases the availability  
14  
15 of these elements in the melt. This inference is supported by qualitative differences in  
16  
17 orthopyroxene proportions from KI-2 (amph  $>$  opx) and KI-3 (opx  $>$  amph) group pumices in  
18  
19 the Kidnappers ignimbrite. These features are the opposite of those observed in the Oruanui  
20  
21 rhyolite, where orthopyroxene was more prevalent at lower pressures in the melt-dominant  
22  
23 body (Allan *et al.*, 2013).  
24  
25  
26

27  
28 Zr concentrations in Kidnappers/Rocky Hill amphiboles show a change also at the  
29  
30 same point as Mn does (at  $\text{Eu}/\text{Eu}^* = 0.3$ ; Fig. 15), in response to the onset of zircon  
31  
32 crystallisation and subsequent removal of Zr from the melt. The upward trend in Zr  
33  
34 concentrations in a minority of amphibole cores with  $\text{Eu}/\text{Eu}^*$  values of 0.8–0.3 suggests the  
35  
36 presence of an antecrystic amphibole component which originally grew in zircon-  
37  
38 undersaturated conditions. These antecrystic cores may have crystallised at deeper levels  
39  
40 and/or pre-date the 1.1 and 1.0 Ma peak crystallisation episodes inferred from U–Pb zircon  
41  
42 age spectra (Cooper *et al.*, 2014). We suggest that the amphibole changes at  $\text{Eu}/\text{Eu}^* < 0.3$ ,  
43  
44 model pressures  $<120$  MPa, and depths of 4.5–4.0 km reflect a change in crystal growth in the  
45  
46 final zircon saturated, melt-dominant bodies that were erupted. The inflection at  $\text{Eu}/\text{Eu}^* < 0.3$   
47  
48 is particularly evident in the KI-2 and RH-2 compositional groups, which also have a large  
49  
50 proportion of ‘down temperature’ core-to-rim textural and chemical changes, as well as core-  
51  
52 to-rim decreases in model amphibole temperature and pressure estimates (Fig. 16). These data  
53  
54  
55 are consistent with the idea of a decompression event, representing significant extraction of  
56  
57  
58  
59  
60



1  
2  
3 melt and crystals from a mush/source zone to establish the KI-2/RH-2 melt-dominant body at  
4  
5 shallower levels. The timing of this process cannot be constrained through zircon U–Pb ages  
6  
7 as zircon growth within the mush zones versus melt dominant bodies cannot be definitively  
8  
9 distinguished. However, within Kidnappers pumices, there are two (low and high aspect ratio)  
10  
11 populations of zircons, with the high aspect ratio population representing rapid zircon  
12  
13 crystallisation that is, within analytical uncertainty, the same as eruption age (Cooper *et al.*,  
14  
15 2014). Extraction of magma from a mush to establish a melt dominant body has the potential  
16  
17 to be geologically rapid (cf. Oruanui: Allan *et al.*, 2013).  
18  
19  
20  
21  
22

### 23 **Distinct magma batches at Mangakino**

24  
25 Glass and whole-rock chemistry, coupled with the textures and chemistry of minerals in both  
26  
27 eruption deposits suggest that each distinct compositional group underwent different  
28  
29 evolutionary pathways and were held at distinct P–T conditions prior to eruption, consistent  
30  
31 with the idea that distinct magma batches were tapped by both eruptions. Even so, the overall  
32  
33 similarities of crystal chemistry and textures between the Kidnappers and Rocky Hill samples  
34  
35 suggest growth within a common mush system, undergoing the same system-wide processes  
36  
37 with the same fractionating assemblages. This source contributed crystals in the assembly of  
38  
39 the final erupted melt-dominant bodies for both the Kidnappers and Rocky Hill eruptions. The  
40  
41 mush source from which the crystals and melt were derived had a broadly similar  
42  
43 composition and is inferred (from model pressure values) to have been lodged at similar or  
44  
45 greater depths (~4–10 km) to the eruptible melt-dominant bodies (3.5–6.5 km). The  
46  
47 geochemical similarities across all the erupted compositions in both eruptions is in part due to  
48  
49 the dominance of greywacke crust within the TVZ, which exerts a strong control on the  
50  
51 generation and final composition of TVZ silicic melts (McCulloch *et al.*, 1994; Graham *et al.*,  
52  
53 1995; Price *et al.*, 2015). The model depths estimated here from amphiboles are comparable  
54  
55  
56  
57  
58  
59  
60

1  
2  
3 to those inferred for other large-scale silicic systems (Brown *et al.*, 1998a; Wallace *et al.*,  
4 1999; Bachmann *et al.*, 2002; Liu *et al.*, 2006; Wilson *et al.*, 2006; Hildreth & Wilson, 2007).  
5  
6  
7 The general similarities in temperature and pressure estimates also imply that the distinctive  
8  
9 melt-dominant bodies tapped throughout the Kidnappers and Rocky Hill eruptions were  
10  
11 laterally separated rather than vertically stacked in the crust.  
12

13  
14 A unique crystal and glass geochemical signature is particularly evident in the KI-3  
15  
16 compositional group that is not found within the earlier erupted Kidnappers fall, or later  
17  
18 erupted Rocky Hill deposits. The majority of crystals in all phases from the KI-3 group  
19  
20 display reverse zoning; light BSE rims (higher An) in plagioclase (Fig. 10) and dark BSE  
21  
22 rims (higher En) in orthopyroxene (Fig. 11). Traversing from core-to-rim, Al increases in all  
23  
24 crystal phases studied, particularly amphibole and orthopyroxene (Figs. 14 and 15). These  
25  
26 core to rim shifts correspond to an apparent temperature increase of ~40 °C (Fig. 16). This  
27  
28 evidence, coupled to the increased range and unique trends in major and trace element glass  
29  
30 chemistry within the KI-3 group points towards interaction with a less evolved, Al-rich end-  
31  
32 member melt that did not mix to any significant extent with the other pumice compositional  
33  
34 groups. The KI-3 glass has no counterpart within the fall deposit implying also that this was a  
35  
36 discrete magma batch, only tapped during ignimbrite emplacement. We infer that mafic  
37  
38 interaction with the KI-3 magma source explains the chemical and temperature changes  
39  
40 within this particular, relatively small-volume, body and has the potential to have 'primed' it  
41  
42 for eruption (cf. Matthews *et al.*, 2012). However, apart from the KI-3 group, there is no  
43  
44 evidence from crystals from a more mafic magma interacting with the rhyolites forming the  
45  
46 rest of the erupted materials, through remobilisation of mush, or eruption triggering.  
47  
48  
49  
50

51  
52 KI-1 and KI-2 type pumice glasses are similar to (but extend the compositional ranges  
53  
54 of) the KF-A (plus KF-C) and KF-B type glass groups in the fall deposit, respectively. Also,  
55  
56 the proportions of mineral textures from the fall can be matched to those of the pumice  
57  
58  
59  
60

1  
2  
3 groups. For example at the base of the fall deposit (KF-A dominant), dark BSE plagioclase  
4 rims are only sparsely present (<10%), similar to KI-1 pumices (12%). Similarly, a  
5  
6 significant increase in the abundance of dark BSE plagioclase rims (typical of KI-B pumice)  
7  
8 coincides with the appearance of KF-B glass. We thus infer that the KI-1 and KF-A, and KI-2  
9  
10 and KF-B group materials originated from the same two melt-dominant bodies and share  
11  
12 common magmatic processes as types A and B material of Cooper *et al.* (2012), respectively.  
13  
14 During eruption of the fall deposit, more restricted bodies of melt were tapped, and hence less  
15  
16 glass heterogeneity is observed (although the fall deposit is  $\sim 2/3$  of the total eruption volume).  
17  
18 After the onset of ignimbrite deposition, more variable (and heterogeneous) melt was tapped  
19  
20 from these melt-dominant bodies (cf. Kennedy *et al.*, 2008). Overlapping matrix glass  
21  
22 compositions in the KI-1 and KI-2 pumice groups suggest that the parental melt-dominant  
23  
24 bodies may have undergone some mutual mixing during ignimbrite generation, and not  
25  
26 remained separate as they were in the earlier eruption stages. However, the distinctive crystal  
27  
28 textural characteristics in the KI-1 and KI-2 groups imply that the two magmas had undergone  
29  
30 different crystallisation histories. In general, minerals from KI-1 pumices have no significant  
31  
32 core-to-rim changes in textures, chemistry or model P–T estimates, whereas those from KI-2  
33  
34 display normal zoning ('down temperature' signals). We thus infer that the KI-1/KF-A melt-  
35  
36 dominant body experienced relatively uniform P–T conditions and similar melt Al  
37  
38 concentrations in the lead-up to eruption, whereas the KI-2/KF-B body cooled (core-to-rim  
39  
40 decrease in model temperature of  $\sim 20\text{--}30$  °C), with accompanying crystal growth and  
41  
42 fractionation. Alternatively, if the amphibole model pressure decrease of  $\sim 10$  MPa is  
43  
44 considered valid, the KI-2/KF-B down-temperature signature may reflect the extraction of  
45  
46 material from a deeper mush zone to form a shallower melt-dominant body prior to eruption,  
47  
48 as seen in the Oruanui eruption (Allan *et al.*, 2013).  
49  
50  
51  
52  
53  
54  
55  
56  
57  
58  
59  
60

1  
2  
3 The KF-C glass (Type C of Cooper *et al.*, 2012) is not represented as a discrete  
4  
5 compositional field in the Kidnappers ignimbrite (KI-1 matrix glass compositions overlap  
6  
7 both KF-A and KF-C glass groups). The KF-C glass type diminishes in abundance upwards in  
8  
9 the fall deposit (Cooper *et al.*, 2012), and it is inferred that this melt was either exhausted  
10  
11 during fall deposit stages of the activity, or that its remnants were incorporated into the KF-  
12  
13 A/KI-1 melt-dominant body.  
14  
15

16 In the Rocky Hill ignimbrite, crystal textures (Figs. 10, 11) and chemistries (Fig. 12)  
17  
18 from the RH-1 and RH-2 groups correspond to those in KI-1 and KI-2, respectively. RH-1  
19  
20 crystals show little core-to-rim changes in chemistry or model P–T estimates and have similar  
21  
22 proportions of non-distinct plagioclase rims and unzoned orthopyroxene grains to their KI-1  
23  
24 counterparts. RH-2 crystals are dominated by normal zoning (‘down temperature’ signals)  
25  
26 with decreases in model core-to-rim temperatures (~20–30 °C) and pressures (10 MPa), as in  
27  
28 KI-2. We interpret these similarities to suggest that the two main melt-dominant bodies  
29  
30 tapped in the Kidnappers were erupted again in the Rocky Hill, or that similar processes re-  
31  
32 established two new magma batches within the same source systems. The similarity of zircon  
33  
34 U–Pb age spectra from the Rocky Hill and Kidnappers (Cooper *et al.*, 2014) suggest growth  
35  
36 within a common system and imply that magmatic processes recorded by Rocky Hill crystals  
37  
38 must pre-date the Kidnappers eruption. However, further crystal growth also occurred during  
39  
40 the time-break between the eruptions, and a significant proportion of plagioclase-rich crystal  
41  
42 mush with associated brown glass was incorporated into the melt dominant body. Also,  
43  
44 deposits of the Rocky Hill do not contain any ‘KI-3 type’ material (either glass compositions  
45  
46 or reversely zoned crystals), consistent with the Rocky Hill ignimbrite representing a separate  
47  
48 eruption.  
49  
50  
51  
52

53  
54 There are other examples of large silicic eruptions that discharged multiple melt  
55  
56 batches with distinct compositional signatures that cannot easily be related by any  
57  
58  
59  
60

1  
2  
3 differentiation or fractional crystallisation process within a single magma body (e.g., Fridrich  
4 & Mahood, 1987; Schuraytz *et al.*, 1989; Briggs *et al.*, 1993; Cambray *et al.*, 1995; Mills *et*  
5 *al.*, 1997). Most of these studies propose models whereby the discrete melt batches are held  
6  
7 within a single unitary magma chamber, with barriers required to inhibit mixing between  
8  
9 compositional groups (e.g., Cambray *et al.*, 1995; Mills *et al.*, 1997). Such a scenario,  
10  
11 however, requires highly complex withdrawal dynamics and arbitrary barriers to mixing, and  
12  
13 may be reconsidered in view of the Kidnappers/Rocky Hill system. In this system, the  
14  
15 compositional separation is more simply accomplished by having horizontally separated melt-  
16  
17 dominant bodies. Such features have previously been documented in the TVZ (Gravley *et al.*,  
18  
19 2007; Shane *et al.*, 2007, 2008a, 2008b; Bégué *et al.*, 2014), although for volumes mostly two  
20  
21 orders of magnitude smaller than these examples.  
22  
23  
24  
25  
26  
27  
28  
29

### 30 **Volumes of the magma types**

31  
32 The relative sizes of magma bodies represented by each compositional group can be inferred  
33  
34 to a first order through the proportions of pumices collected for analysis. On the basis of  
35  
36 whole-rock data, 3 of 42 Kidnappers ignimbrite pumices belong to the KI-3 compositional  
37  
38 group, suggesting that this group comprises <10% of the total juvenile material. The KI-3  
39  
40 group is not represented in the Kidnappers fall deposit (i.e., ~2/3 of the total erupted extra-  
41  
42 caldera material) and this distinctive magma batch therefore represents <3% of the erupted  
43  
44 magma overall. The KI-1 group is the dominant composition within the Kidnappers  
45  
46 ignimbrite (27 out of 42 pumices: ~65 %), with the KI-2 group making up the remaining  
47  
48 ~30%. These volume proportions of KI-1 and KI-2 are broadly similar to the proportions of  
49  
50 KF-A (~68%) and KF-B (~22%) glass material reported from the fall deposit (Cooper *et al.*,  
51  
52 2012). If we infer that these respective groups in the fall and flow originated from common  
53  
54 melt-dominant bodies (KF-A = KI-A; KF-B = KI-B) then total contributions of erupted  
55  
56  
57  
58  
59  
60

1  
2  
3 magma from the two largest melt-dominant bodies are ~65% (780 km<sup>3</sup> DRE) and ~25% (300  
4 km<sup>3</sup> DRE), respectively. The two other less voluminous melts, KI-3 and KF-C are ~3% (40  
5 km<sup>3</sup> DRE) and ~7% (80 km<sup>3</sup> DRE). These absolute estimates may be ±50% (cf. Hildreth,  
6  
7  
8 1981, his Fig. 1), but the relative proportions are unlikely to change. The respective magma  
9  
10 volumes discharged in the Rocky Hill eruption are less well constrained due to the continuous  
11  
12 range in whole-rock compositions making a clear distinction between RH-1 and RH-2  
13  
14 difficult. On the basis of glass chemistry proportions, however, the RH-1 group (linked to KI-  
15  
16 1 and KF-A) remains the dominant magma type.  
17  
18  
19

### 20 21 22 23 **Compositional and mineralogical comparisons between products of the Kidnappers and** 24 **Rocky Hill eruptions** 25 26

27  
28 As a whole, glasses from the Kidnappers and Rocky Hill eruptions are unusual in the fact that  
29  
30 both major and trace element chemical heterogeneity is displayed over a complete range of  
31  
32 scales, from chamber-wide, through single-clast, to sub-millimetre scales. Although some  
33  
34 rhyolitic eruptions in the TVZ have compositional variations in glass (e.g. Nairn *et al.*, 2004;  
35  
36 Shane *et al.*, 2003, 2008b), this level of heterogeneity is unusual in most TVZ rhyolitic  
37  
38 eruptions (e.g. Sutton *et al.*, 1995; Allan *et al.*, 2008). The switch from fall activity to  
39  
40 ignimbrite generation in the Kidnappers eruption is inferred to have been accompanied by  
41  
42 wider scale caldera collapse, which disrupted the systematic withdrawal of discrete magma  
43  
44 bodies (Cooper *et al.*, 2012), and triggered the catastrophic evacuation of all magma batches.  
45  
46  
47

48  
49 The pumice glasses from the Kidnappers and Rocky Hill ignimbrites provide evidence  
50  
51 for contrasting magmatic processes involved in each eruption. K<sub>2</sub>O concentrations in  
52  
53 Kidnappers pumices (particularly KI-2) are greater than would be expected from fractional  
54  
55 crystallisation of the minerals present, and whole-rock to glass K<sub>2</sub>O tie-lines have negative  
56  
57 slopes (Fig. 4) indicating the addition of K<sub>2</sub>O. Magma mixing can be ruled out as a cause of  
58  
59  
60

1  
2  
3 K<sub>2</sub>O addition as respective glass K<sub>2</sub>O concentrations are not elevated and do not show larger  
4  
5 variations. The K<sub>2</sub>O addition is better explained by incorporation of xenocrystic biotite into  
6  
7 Kidnappers magmas (Fig. 4), consistent also with higher Rb concentrations, and increasing  
8  
9 Rb/Sr ratios in Kidnappers whole-rock data, although the latter is also influenced by the  
10  
11 plagioclase content of the pumices (Fig. 5).  
12

13  
14 In contrast to the Kidnappers, whole-rock to glass K<sub>2</sub>O tie-lines within Rocky Hill  
15  
16 pumices have positive slopes (Fig. 7) consistent with a fractional crystallisation trend. Whole-  
17  
18 rock Al<sub>2</sub>O<sub>3</sub> values extend to considerably higher concentrations in Rocky Hill pumices than in  
19  
20 the Kidnappers with little accompanying change in glass values (Fig. 7), consistent with a  
21  
22 greater abundance of Al-rich phases (plagioclase and amphibole). Whole-rock Y  
23  
24 concentrations in the Kidnappers samples do not correlate with Al<sub>2</sub>O<sub>3</sub>, whereas in the Rocky  
25  
26 Hill they form a tightly defined trend (Fig. 8). Y is particularly enriched in amphibole  
27  
28 ( $[Y_{\text{amph}}]/[Y_{\text{melt}}] = 10$ ) when compared to the other major crystal phases (supplementary  
29  
30 electronic appendices). The Rocky Hill data thus imply that there was either a strong  
31  
32 amphibole crystallisation control or an input of amphibole into the melt dominant bodies  
33  
34 during the time gap between the Kidnappers and Rocky Hill eruptions.  
35  
36  
37  
38

39 Major element matrix glass compositions in Rocky Hill pumices have smaller ranges  
40  
41 than those within Kidnappers pumices (Fig. 9), while trace element concentrations have a  
42  
43 larger range within the RH-1 group in comparison to KI-1. The reduction in major element  
44  
45 diversity in the pumices is inferred to reflect convective stirring in the chamber in the  
46  
47 aftermath of Kidnappers caldera collapse (e.g., Marshall & Sparks, 1984; Folch *et al.*, 2001;  
48  
49 Kennedy & Stix, 2007; Kennedy *et al.*, 2008). An alternative, but not opposing possibility is  
50  
51 that smaller and compositionally more uniform sources were tapped during the Rocky Hill  
52  
53 eruption, as suggested by the narrower range in model temperature and pressure estimates.  
54  
55  
56 Rim compositions within the Rocky Hill crystals also plot into tighter and more discrete  
57  
58  
59  
60



1  
2  
3 groups, reflecting a reduction in the compositional diversity of the melt. The two glass  
4  
5 compositional groupings within the Rocky Hill are remarkably similar to the KF-A and KF-B  
6  
7 Kidnappers fall deposit glass compositional groups. If we infer that the RH-1 and RH-2 melt  
8  
9 groups originated from the same sources as the KF-A/KI-1 and KF-B/KI-2 melt groups, then  
10  
11 there are two possible end-member scenarios.  
12

13  
14 First, portions of the two distinctive melt-dominant bodies remained after the  
15  
16 Kidnappers eruption and were re-erupted. This scenario alone is precluded by the differences  
17  
18 in crystal zonation patterns and the differences in glass types between the two suites of  
19  
20 deposits. In particular, there is the brown glass selvages and thick bubble walls associated  
21  
22 with plagioclase-bearing clots and 'phenoclasts', commonly found within Rocky Hill pumices  
23  
24 but exceedingly rare within Kidnappers pumices. This brown glass has fluid-affected  
25  
26 compositions (low  $K_2O$ , Rb and Li; high  $Na_2O$ : Supplementary Fig. 1), typically infilling and  
27  
28 surrounding shattered plagioclase grains. The brown glass phenoclasts are contained within  
29  
30 pumice with 'normal' glass chemistry and therefore this alteration is not secondary or a result  
31  
32 of vapour-phase alteration in the deposit during cooling. We interpret these clots and  
33  
34 associated glass to represent the incorporation of a disrupted plagioclase-rich border zone to  
35  
36 the magma body. In addition,  $Al_2O_3$  values in the Rocky Hill pumices are significantly higher  
37  
38 at the same  $Eu/Eu^*$  values as the Kidnappers pumices/glasses and do not trend towards their  
39  
40 respective glass compositions (Figs. 4 and 7). Also, the whole-rock compositional array does  
41  
42 not trend toward its respective glass compositions (Fig. 7), implying that an additional  
43  
44 plagioclase component is present in Rocky Hill pumices, consistent with the addition of  
45  
46 antecrystic material from a crystal mush.  
47  
48  
49  
50

51  
52 Second, two melt-dominant bodies were re-established anew during the time break  
53  
54 between the two events, incorporating new material from common deeper mush sources and  
55  
56 replicating the earlier voluminous KI-1 and KI-2 magma bodies. This scenario alone is  
57  
58  
59  
60



1  
2  
3 precluded by our interpretation of the closely similar zircon age characteristics between the  
4 Kidnappers and Rocky Hill samples (Cooper *et al.*, 2014). If the Rocky Hill melt-dominant  
5 bodies were wholly newly created, then we would expect a greater proportion of the zircons  
6 to have come from the inherited 1.1 Ma crystallization mode. We thus interpret the Rocky  
7 Hill crystals and melts forming magma types RH-1 and RH-2 to represent a combination of  
8 new material extracted from a common crystal mush with existing remnants of the two largest  
9 melt dominant bodies tapped during the Kidnappers eruption.  
10  
11  
12  
13  
14  
15  
16  
17  
18  
19

### 20 21 **A model of the magmatic system for the Kidnappers and Rocky Hill eruptions**

22  
23 The following outlines the evolution of the Kidnappers/Rocky Hill magmatic system  
24 illustrated in Fig. 18, from eruption of the Kidnappers fall deposit and to the Rocky Hill  
25 eruption.  
26  
27  
28  
29

#### 30 31 32 *Earlier Kidnappers eruption (fall deposits)*

33  
34 During the eruption of the Kidnappers fall deposit, three discrete, horizontally separated melt-  
35 dominant bodies (type KF-A, KF-B and KF-C) are inferred to have been tapped from three  
36 vent systems to yield the simultaneous and sequential compositional changes in the fall  
37 deposit (Cooper *et al.*, 2012) (Fig. 18). No interaction or mixing took place between the melt-  
38 dominant bodies during this stage. The erupted volumes of melt were homogeneous, with  
39 little or no evidence for stratification and were stored at depths of ~3.5 to 6.5 km. The  
40 systematic tapping of the three horizontally separated melt-dominant bodies may have been  
41 controlled by tectonic processes following the partial drainage of the magma body feeding  
42 glass group KF-A and its associated crystals (Cooper *et al.*, 2012). Due to the volumes of  
43 magma that were evacuated during this stage, it seems likely that caldera collapse  
44 accompanied the eruption of the Kidnappers fall deposit. The initial caldera collapse may  
45  
46  
47  
48  
49  
50  
51  
52  
53  
54  
55  
56  
57  
58  
59  
60

1  
2  
3 have been related to geographically separated vents (cf. Gravley *et al.*, 2007), and therefore  
4  
5 deposition of the fall deposit remained systematic, rather than being accompanied by gross  
6  
7 mixing of the glass types.  
8  
9

10  
11  
12 *Later Kidnappers eruption (ignimbrite)*  
13

14 Draining of the melt-dominant bodies and tectonic readjustment is inferred to have caused  
15  
16 further and more widespread caldera collapse and a consequent increase in the eruption  
17  
18 intensity to generate the pyroclastic flows that deposited the Kidnappers ignimbrite. We  
19  
20 suggest that tectonic rupturing may have occurred between the initially separated calderas,  
21  
22 leading to wider scale collapse and an increase in the eruption intensity driving the fall-to-  
23  
24 flow transition. It is inferred that the ignimbrite-forming stage saw the evacuation of a wider  
25  
26 diversity of material from three distinct batches of melt plus crystals (Fig. 18). The earlier  
27  
28 KF-C melt dominant body was either incorporated into the volumetrically dominant KF-  
29  
30 A/KI-1 magma body, or had been entirely drained during the earlier fall deposit stage of the  
31  
32 eruption.  
33  
34  
35

36  
37 Of the two major magma bodies, material erupted from the KF-A/KI-1 magma body  
38  
39 had remained at a uniform depths and without any significant changed in temperature prior to  
40  
41 eruption, as represented in the mineral zonations. In contrast KF-B/KI-2 magma body rose to  
42  
43 shallower depths and experienced a fall in temperatures shortly before eruption. We interpret  
44  
45 this to represent the extraction of large volumes of crystals and melt from a deeper crystal  
46  
47 mush to establish a melt-dominant body at shallower levels. The KI-2 pumices also contain  
48  
49 more biotite, suggesting a greater involvement of lower temperature, biotite-richer marginal  
50  
51 material at shallower levels, represented in whole-rock and glass compositional trends. The  
52  
53 somewhat smaller KI-3 magma body interacted with hotter, lesser evolved melts during pre-  
54  
55  
56  
57  
58  
59  
60

1  
2  
3 eruptive storage, and did not mix syn-eruptively with the two larger melt-dominant bodies  
4  
5 discussed above (Fig. 18).  
6

7 Each compositional group within the Kidnappers ignimbrite is represented at the same  
8  
9 single stratigraphic level where there were no signs of any significant time breaks (e.g. flow  
10  
11 unit boundaries). We thus infer that the evacuation of the diverse magmas involved in the  
12  
13 later stages of the Kidnappers eruption was simultaneous.  
14  
15

### 16 17 18 *Prior to and during the Rocky Hill eruption* 19

20  
21 Data presented here suggest that in the time break between the Kidnappers and Rocky Hill  
22  
23 eruptions, the two largest melt-dominant magma bodies from the Kidnappers eruption were in  
24  
25 part reestablished from the same mush regions (Fig. 18). The Rocky Hill melt-dominant  
26  
27 bodies were more homogeneous than their counterparts in the Kidnappers, which may reflect:  
28  
29 (1) smaller volumes being tapped in the Rocky Hill eruption (2) a significant volume of new  
30  
31 melt plus an inherited population of zircons (Cooper *et al.*, 2014) being generated or extracted  
32  
33 from the mush/source zone (3) post-Kidnappers caldera collapse and tectonic readjustment  
34  
35 stirring magma remaining from the Kidnappers event (Marshall & Sparks, 1984; Folch *et al.*,  
36  
37 2001; Kennedy *et al.*, 2008). The reestablished bodies were more crystal rich (10-20%),  
38  
39 which may in part be due to the draining of significant proportions of eruptible melt and the  
40  
41 dredging of crystals (particularly plagioclase) from the inferred common mush zone.  
42  
43  
44

45  
46 It is conceivable that caldera collapse or tectonic readjustments accompanying  
47  
48 eruption of the Kidnappers fall deposit may have itself been the trigger mechanism for the  
49  
50 firstly systematic, and then repeated evacuation of magma through the Kidnappers and Rocky  
51  
52 Hill eruptions (cf. Gravley *et al.*, 2007; Bégué *et al.*, 2014). Allan *et al.* (2013) suggested that  
53  
54 rifting and extensional processes in the mush-bearing crust prior to the Oruanui eruption  
55  
56 promoted melt channels, whereby melt (and crystals) could be extracted to establish the melt-  
57  
58  
59  
60

1  
2  
3 dominant body over geologically rapid timescales (centuries). A similar scenario is suggested  
4  
5 in this system to explain the rapid renewal of eruptible melt and crystals from a common  
6  
7 mush zone following the Kidnappers and prior to the Rocky Hill eruption. The evidence from  
8  
9 modern Taupo (Sutton *et al.*, 1995; Wilson & Charlier, 2009; Allan *et al.*, 2012; Barker *et al.*,  
10  
11 2015), as well as from Mangakino suggests that parallel magma systems are able to operate in  
12  
13 the crust within the conditions of the TVZ.  
14  
15

## 16 17 18 **CONCLUSIONS** 19

20  
21  
22 The Mangakino volcanic centre was highly active around 1 Ma, producing ~1200 km<sup>3</sup> of  
23  
24 magma in the Kidnappers event followed by another ~200 km<sup>3</sup> during the Rocky Hill event.  
25

26  
27 From the petrological and geochemical dataset presented here, we conclude the following.

- 28  
29 (1) Both field constraints and the general similarity of crystal compositions and textures,  
30  
31 glass chemistry and zircon age spectra (Cooper *et al.*, 2014) between both eruptions  
32  
33 provides unequivocal evidence that magmas for both eruptions came from a common  
34  
35 deeper mush system. This system represented a source of crystals (and melt) with  
36  
37 broadly similar chemistries giving rise to the compositional similarity of the  
38  
39 Kidnappers fall deposit and subsequent Kidnappers and Rocky Hill ignimbrites.  
40  
41  
42 (2) Subtle variations in pumice mineralogy and whole-rock compositions, glass chemistry  
43  
44 and crystal textures are consistent with the notion that the Kidnappers and Rocky Hill  
45  
46 are distinct events and not the products of one zoned eruption. The renewal of  
47  
48 compositionally similar melt-dominant bodies between the Kidnappers and Rocky Hill  
49  
50 events, and the geologically short timescales involved highlights the rapidity of the  
51  
52 rejuvenation processes at Mangakino.  
53  
54  
55 (3) The systematically zoned Kidnappers fall deposit provides evidence for the tapping of  
56  
57 three discrete magma bodies whereas the Kidnappers ignimbrite is more  
58  
59  
60

1  
2  
3 compositionally diverse. The change from fall to flow is inferred to mark a change in  
4  
5 the scale and siting of caldera collapse and the simultaneous evacuation of discrete but  
6  
7 compositionally diverse melts. Compositional heterogeneity within the Kidnappers  
8  
9 and Rocky Hill ignimbrites is found both at the chamber-wide and pumice scale, and  
10  
11 the full compositional spectrum can be found in pumices sampled at any one  
12  
13 stratigraphic level within each ignimbrite. Evacuation of a single stratified magma  
14  
15 chamber is not a viable option for the Kidnappers/Rocky Hill eruptions. The magmatic  
16  
17 system involved multiple melt-dominant bodies, which were apparently drained  
18  
19 during the Kidnappers event. The two largest bodies were reestablished from a  
20  
21 common source region or mush prior to re-eruption during the Rocky Hill event.  
22  
23

- 24  
25 (4) Apart from the KI-3 magma type, there is no evidence to suggest there was interaction  
26  
27 with a lesser evolved, hotter magma. Within KI-3, this interaction may have played a  
28  
29 role in priming the smaller volume of magma prior to the Kidnappers eruption.  
30  
31 However, crystals from the two volumetrically dominant magma types in the  
32  
33 Kidnappers and Rocky Hill show no evidence for a temperature increase in the erupted  
34  
35 magma, rebomilisation of the mush, or an eruption trigger.  
36  
37
- 38 (5) Caldera collapse episodes apparently exerted significant control on the intensity and  
39  
40 timing of eruptions at Mangakino. During eruption of the Kidnappers fall deposit, the  
41  
42 systematic tapping of discrete magmas suggests that any caldera collapse areas  
43  
44 remained separate and confined to an association with each single melt-dominant body  
45  
46 (Fig. 18). The change in the Kidnappers eruption from fall deposition to the onset of  
47  
48 pyroclastic flows marks an apparent change in the scale and siting of caldera collapse.  
49  
50 The rapid rejuvenation of more homogeneous melt-dominant bodies and the triggering  
51  
52 of the Rocky Hill eruption, may also be attributed to stirring after caldera collapse  
53  
54 and/or a strong extensional tectonic control at Mangakino. Regional rifting processes  
55  
56  
57  
58  
59  
60

1  
2  
3 may have contributed towards allowing extracted melts and crystals to ascend rapidly  
4  
5 to reestablish or renew the melt-dominant bodies on such a short time scale of  
6  
7 decades.  
8  
9

## 10 11 **FUNDING**

12  
13 This work was supported by a Victoria University PhD Scholarship (GFC), and by the Royal  
14  
15 Society of New Zealand through the Marsden Fund (VUW0813) and a James Cook  
16  
17 Fellowship (CJNW).  
18  
19

## 20 21 **ACKNOWLEDGEMENTS**

22  
23 We thank Roger Briggs, Michelle Coombs and John Gamble for constructive comments and  
24  
25 edits of a preliminary version of this manuscript, Wim Degruyter and Matt Coble for  
26  
27 comments on the submitted manuscript and Richard Price for editorial handling.  
28  
29  
30  
31

## 32 33 **SUPPLEMENTARY DATA**

34  
35 Supplementary data are available at *Journal of Petrology* online  
36  
37  
38  
39

## 40 41 **REFERENCES**

- 42  
43 Allan, A. S. R., Baker, J. A., Carter, L. & Wysoczanski, R. J. (2008). Reconstructing the  
44  
45 Quaternary evolution of the world's most active silicic volcanic system: insights from  
46  
47 an ~1.65 Ma deep ocean tephra record sourced from Taupo Volcanic Zone, New  
48  
49 Zealand. *Quaternary Science Reviews* **27**, 2341-2360.  
50  
51  
52 Allan, A. S. R., Wilson, C. J. N., Millet, M. -A. & Wysoczanski, R. J. (2012). The invisible  
53  
54 hand: tectonic triggering and modulation of a rhyolitic supereruption. *Geology* **40**,  
55  
56 563-566.  
57  
58  
59  
60

- 1  
2  
3 Allan, A. S. R., Morgan, D. J., Wilson, C. J. N. & Millet, M. -A. (2013). From mush to  
4  
5 eruption in centuries: assembly of the super-sized Oruanui magma body.  
6  
7 *Contributions to Mineralogy and Petrology* **166**, 143-164.  
8
- 9  
10 Alloway, B. V., Pillans, B. J., Carter, L., Naish, T. R. & Westgate, J. A. (2005). Onshore-  
11  
12 offshore correlation of Pleistocene rhyolitic eruptions from New Zealand: implications  
13  
14 for TVZ eruptive history and paleoenvironmental construction. *Quaternary Science*  
15  
16 *Reviews* **24**, 1601-1622.  
17
- 18  
19 Bachmann, O. & Bergantz, G. W. (2008). Deciphering magma chamber dynamics from styles  
20  
21 of compositional zoning in large silicic ash flow sheets. *Reviews in Mineralogy and*  
22  
23 *Geochemistry* **69**, 651-674.  
24
- 25  
26 Bachmann, O., Dungan, M. A. & Lipman, P. W. (2002). The Fish Canyon magma body, San  
27  
28 Juan volcanic field, Colorado: rejuvenation and eruption of an upper-crustal batholith.  
29  
30 *Journal of Petrology* **43**, 1469-1503.  
31
- 32  
33 Bacon, C. R. & Hirschmann, M. M. (1988). Mg/Mn partitioning as a test for equilibrium  
34  
35 between coexisting Fe–Ti oxides. *American Mineralogist* **73**, 57-61.  
36
- 37  
38 Barker, S. J., Wilson, C. J. N., Allan, A. S. R. & Schipper, C. I. (2015). Fine-scale temporal  
39  
40 recovery, reconstruction and evolution of a post-supereruption magmatic system.  
41  
42 *Contributions to Mineralogy and Petrology* **170**, article 5.  
43
- 44  
45 Bégué, F., Deering, C. D., Gravley, D. M., Kennedy, B. M., Chambefort, I., Gualda, G. A. R.  
46  
47 & Bachmann, O. (2014). Extraction, storage and eruption of multiple isolated magma  
48  
49 batches in the paired Mamaku and Ohakuri eruption, Taupo Volcanic Zone, New  
50  
51 Zealand. *Journal of Petrology* **55**, 1653-1684.  
52
- 53  
54 Best, M. G. & Christiansen, E. H. (1997). Origin of broken phenocrysts in ash-flow tuffs.  
55  
56 *Geological Society of America Bulletin* **109**, 63-73.  
57
- 58  
59  
60



- 1  
2  
3 and correlation to global oxygen isotope stratigraphy. *Earth and Planetary Science*  
4  
5 *Letters* **109**, 573-584.  
6
- 7 Blank, H. R. (1965). Ash-flow deposits of the central King Country, New Zealand. *New*  
8  
9 *Zealand Journal of Geology and Geophysics* **8**, 588-607.  
10
- 11 Blundy, J. & Cashman, K. (2008) Petrological reconstruction of magmatic system variables  
12  
13 and processes. In: Putirka, K. D. & Tepley, F. J. (Eds.), *Minerals, inclusions and*  
14  
15 *volcanic processes. Reviews in Mineralogy and Geochemistry* **69**, 179–239  
16  
17
- 18 Blundy, J., Cashman, K. & Humphreys, M. (2006). Magma heating by decompression-driven  
19  
20 crystallization beneath andesite volcanoes. *Nature* **443**, 76-80.  
21  
22
- 23 Briggs, R. M., Gifford, M. G., Moyle, A. R., Taylor, S. R., Norman, M. D., Houghton, B. F.  
24  
25 & Wilson, C. J. N. (1993). Geochemical zoning and eruptive mixing in ignimbrites  
26  
27 from Mangakino volcano, Taupo Volcanic Zone, New Zealand. *Journal of*  
28  
29 *Volcanology and Geothermal Research* **56**, 175-203.  
30  
31
- 32 Brown, S. J. A., Wilson, C. J. N., Cole, J. W. & Wooden, J. (1998a). The Whakamaru group  
33  
34 ignimbrites, Taupo Volcanic Zone, New Zealand: evidence for reverse tapping of a  
35  
36 zoned silicic magma system. *Journal of Volcanology and Geothermal Research* **84**, 1-  
37  
38 37.  
39
- 40 Brown, S. J. A., Burt, R. M., Cole, J. W., Krippner, S. J. P., Price, R. C. & Cartwright, I.  
41  
42 (1998b). Plutonic lithics in ignimbrites of Taupo Volcanic Zone, New Zealand:  
43  
44 sources and conditions of crystallisation. *Chemical Geology* **148**, 21-41.  
45  
46
- 47 Cambray, F. W., Vogel, T. A. & Mills, J. G. (1995). Origin of compositional heterogeneities  
48  
49 in tuffs of the Timber Mountain Group: the relationship between magma batches and  
50  
51 magma transfer and emplacement in an extensional environment. *Journal of*  
52  
53 *Geophysical Research* **100**, 15793-15805.  
54  
55
- 56 Carter, L., Alloway, B. V., Shane, P. & Westgate, J. A. (2004). Deep-ocean record of major  
57  
58  
59  
60

- 1  
2  
3 late Cenozoic rhyolitic eruptions from New Zealand. *New Zealand Journal of Geology*  
4  
5 *and Geophysics* **47**, 481-500.  
6  
7 Cashman, K. V. & Giordano, G. (2014). Calderas and magma reservoirs. *Journal of*  
8  
9 *Volcanology and Geothermal Research* **288**, 28-45.  
10  
11 Cathey, H. E. & Nash, B.P. (2004). The Cougar Point Tuff: implications for thermochemical  
12  
13 zonation and longevity of high-temperature, large volume silicic magmas of the  
14  
15 Miocene Yellowstone hotspot. *Journal of Petrology* **45**, 27-58.  
16  
17 Chamberlain, K. J., Wilson, C. J. N., Wallace, P. J. & Millet, M. -A. (2015). Micro-analytical  
18  
19 perspectives on the Bishop Tuff and its magma chamber. *Journal of Petrology* **56**,  
20  
21 605-640.  
22  
23 Chesner, C. A. (2012). The Toba caldera complex. *Quaternary International* **258**, 5-18.  
24  
25 Cole, J. W. & Lewis, K. B. (1981). Evolution of the Taupo-Hikurangi subduction system.  
26  
27 *Tectonophysics* **72**, 1-21.  
28  
29 Cole, J. W., Milner, D. M. & Spinks, K. D. (2005). Calderas and caldera structures: a review.  
30  
31 *Earth-Science Reviews* **69**, 1-26.  
32  
33 Coombs, M. L., Sisson, T. W., Bleick, H. A., Henton, S. M., Nye, C. J., Payne, A. L.,  
34  
35 Cameron, C. E., Larsen, J. F., Wallace, K. L. & Bull, K. F. (2013). Andesites of the  
36  
37 2009 eruption of Redoubt Volcano, Alaska, *Journal of Volcanology and Geothermal*  
38  
39 *Research* **259**, 349-372.  
40  
41 Cooper, G. F. & Wilson, C. J. N. (2014). Development, mobilization and eruption of a large  
42  
43 crystal rich ignimbrite: the Ongatiti ignimbrite, New Zealand. *Lithos* **198-199**, 38-57.  
44  
45 Cooper, G. F., Wilson, C. J. N., Millet, M. -A., Baker, J. & Smith, E. G. C. (2012).  
46  
47 Systematic tapping of independent magma chambers during the 1 Ma Kidnappers  
48  
49 supereruption. *Earth and Planetary Science Letters* **213-214**, 23-33.  
50  
51 Cooper, G. F., Wilson, C. J. N., Charlier B. L. A., Wooden, J. L. & Ireland, T. R. (2014).  
52  
53  
54  
55  
56  
57  
58  
59  
60

1  
2  
3 Temporal evolution and compositional signatures of two supervolcanic systems  
4 recorded in zircons from Mangakino volcanic centre, New Zealand. *Contributions to*  
5  
6  
7 *Mineralogy and Petrology* **167**, 1018.  
8

9  
10 De Angelis, S. H., Larsen, J. & Coombs, M. (2013). Pre eruptive magmatic conditions at  
11  
12 Augustine volcano, Alaska, 2006: evidence from amphibole geochemistry and textures.  
13  
14 *Journal of Petrology* **54**, 1939-1961.  
15

16  
17 Dunbar, N. W., Hervig, R. L. & Kyle, P. R. (1989). Determination of pre-eruptive H<sub>2</sub>O, F and  
18  
19 Cl contents of silicic magmas using melt inclusions: examples from Taupo volcanic  
20  
21 centre, New Zealand. *Bulletin of Volcanology* **51**, 177-184.  
22

23  
24 Erdmann, S., Martel, C., Pichavant, M. & Kushnir, K. (2014). Amphibole as an archivist of  
25  
26 magmatic crystallization conditions: problems, potential, and implications for  
27  
28 inferring magma storage prior to the paroxysmal 2010 eruption of Mount Merapi,  
29  
30 Indonesia. *Contributions to Mineralogy and Petrology* **167**, article 1016.  
31

32  
33 Fridrich, C. J. & Mahood, G. A. (1987). Compositional layers in the zoned magma chamber  
34  
35 of the Grizzly Peak Tuff. *Geology* **15**, 299-303.  
36

37  
38 Folch, A., Codina, R. & Martí, J. (2001). Numerical modeling of magma withdrawal during  
39  
40 explosive caldera-forming eruptions. *Journal of Geophysical Research* **106**, 16163-  
41  
42 16175.  
43

44  
45 Ghiorso, M. S. & Evans, B. W. (2008). Thermodynamics of rhombohedral oxide solid  
46  
47 solutions and a revision of the Fe-Ti two-oxide geothermometer and oxygen-  
48  
49 barometer. *American Journal of Science* **308**, 957-1039.  
50

51  
52 Girard, G. & Stix, J. (2010). Rapid extraction of discrete magma batches from a large  
53  
54 differentiating magma chamber: the Central Plateau Member rhyolites, Yellowstone  
55  
56 caldera, Wyoming. *Contributions to Mineralogy and Petrology* **160**, 441-465.  
57

58  
59 Graham, I. J., Cole, J. W., Briggs, R. M., Gamble, J. A. & Smith, I. E. M. (1995). Petrology  
60

- 1  
2  
3 and petrogenesis of volcanic rocks from the Taupo Volcanic Zone: a review. *Journal*  
4  
5 *of Volcanology and Geothermal Research* **68**, 59-87.  
6  
7  
8 Gravley, D. M., Wilson, C. J. N., Leonard, G. S. & Cole, J. W. (2007). Double trouble: paired  
9  
10 ignimbrite eruptions and collateral subsidence in the Taupo Volcanic Zone, New  
11  
12 Zealand. *Geological Society of America Bulletin* **119**, 18-30.  
13  
14 Hildreth, W. (1979). The Bishop Tuff: evidence for the origin of compositional zonation in  
15  
16 silicic magma chambers. In: Chapin, C. E. & Elston, W. E. (Eds.) *Ash-flow tuffs*.  
17  
18 *Geological Society of America, Special Paper* **180**, 43-75.  
19  
20  
21 Hildreth, W. (1981). Gradients in silicic magma chambers: implications for lithospheric  
22  
23 magmatism. *Journal of Geophysical Research* **86**, 10153-10192.  
24  
25  
26 Hildreth, W. (2004). Volcanological perspectives on Long Valley, Mammoth Mountain, and  
27  
28 Mono Craters: several contiguous but discrete systems. *Journal of Volcanology and*  
29  
30 *Geothermal Research* **136**, 169-198.  
31  
32  
33 Hildreth, W. & Wilson, C. J. N. (2007). Compositional zoning of the Bishop Tuff. *Journal of*  
34  
35 *Petrology* **48**, 951-999.  
36  
37  
38 Holland, T. & Blundy, J. (1994). Non-ideal interactions in calcic amphiboles and their  
39  
40 bearing on amphibole-plagioclase thermometry. *Contributions to Mineralogy and*  
41  
42 *Petrology* **116**, 433-447.  
43  
44  
45 Houghton, B. F., Wilson, C. J. N., McWilliams, M. O., Lanphere, M. A., Weaver, S. D.,  
46  
47 Briggs, R. M. & Pringle, M. S. (1995). Chronology and dynamics of a large silicic  
48  
49 magmatic system: central Taupo Volcanic Zone, New Zealand. *Geology* **23**, 13-16.  
50  
51  
52 Kennedy, B. M. & Stix, J. (2007). Magmatic processes associated with caldera collapse at  
53  
54 Ossipee ring dyke, New Hampshire. *Geological Society of America Bulletin* **119**, 3-17.  
55  
56  
57 Kennedy, B. M., Jellinek, A. M. & Stix, J. (2008). Coupled caldera subsidence and stirring  
58  
59 inferred from analogue models. *Nature Geoscience* **1**, 385-389.  
60

- 1  
2  
3 Kennedy, B. M., Wilcock, J. & Stix, J. (2012). Caldera resurgence during magma  
4 replenishment and rejuvenation at Valles and Lake City calderas. *Bulletin of*  
5 *Volcanology* **74**, 833-847.  
6  
7  
8  
9  
10 Kiss, B., Harang, S., Ntaflou, T., Mason, P. R. D. & Pál-Molnár, E. (2014). Amphibole  
11 perspective to unravel pre-eruptive processes and conditions in volcanic plumbing  
12 systems beneath intermediate arc volcanoes: a case study from Ciomadul volcano (SE  
13 Carpathians). *Contributions to Mineralogy and Petrology* **167**, article 986.  
14  
15  
16  
17  
18 Leake, B. E., Woolley, A. R., Birch, W. D., Burke, E. A., Ferraris, G., Grice, J. D.,  
19 Hawthorne, F. C., Kisch, H.J., Krivovichev, V. G. & Schumacher, J. C. (2004).  
20 Nomenclature of amphiboles: additions and revisions to the International  
21 Mineralogical Association's amphibole nomenclature. *American Mineralogist* **89**,  
22 883-887  
23  
24  
25  
26  
27  
28  
29  
30 Liu, Y., Anderson, A. T., Wilson, C. J. N., Davis, A. M. & Steele, I. M. (2006). Mixing and  
31 differentiation in the Oruanui rhyolitic magma, Taupo, New Zealand: evidence from  
32 volatiles and trace elements in melt inclusions. *Contributions to Mineralogy and*  
33 *Petrology* **151**, 71-87.  
34  
35  
36  
37  
38  
39  
40  
41  
42  
43  
44  
45  
46  
47  
48  
49  
50  
51  
52  
53  
54  
55  
56  
57  
58  
59  
60

- 1  
2  
3 McCulloch, M. T., Kyser, T. K., Woodhead, J. & Kinsley, L. (1994). Pb-Sr-Nd-O isotopic  
4  
5 constraints on the origin of rhyolites from the Taupo Volcanic Zone of New Zealand:  
6  
7 evidence for assimilation followed by fractionation from basalt. *Contributions to*  
8  
9 *Mineralogy and Petrology* **115**, 303-312.  
10  
11 Metz, J. M. & Mahood, G. A. (1985). Precursors to the Bishop Tuff eruption: Glass  
12  
13 Mountain, Long Valley, California. *Journal of Geophysical Research* **90**, 11121-  
14  
15 11126.  
16  
17 Metz, J. M. & Mahood, G. A. (1991). Development of the Long Valley, California, magma  
18  
19 chamber recorded in precaldera rhyolite lavas of Glass Mountain. *Contributions to*  
20  
21 *Mineralogy and Petrology* **106**, 379-397.  
22  
23 Moyle, A. R. (1989). Volcanic geology and geochemistry of the Rocky Hill Ignimbrite,  
24  
25 Upper Waipa Valley. M.Sc. thesis University of Waikato, Hamilton, New Zealand.  
26  
27  
28  
29 Miller, C. F. & Wark, D. A. (2008). Supervolcanoes and their explosive supereruptions.  
30  
31 *Elements* **4**, 11-16.  
32  
33  
34 Milner, D. M., Cole, J. W. & Wood, C. P. (2003). Mamaku Ignimbrite: a caldera-forming  
35  
36 ignimbrite erupted from a compositionally zoned magma chamber in Taupo Volcanic  
37  
38 Zone, New Zealand. *Journal of Volcanology and Geothermal Research* **122**, 243-264.  
39  
40  
41 Mills, J. G., Saltoun, B. W. & Vogel, T. A. (1997). Magma batches in the Timber Mountain  
42  
43 magmatic system, southwestern Nevada volcanic field, Nevada, USA. *Journal of*  
44  
45 *Volcanology and Geothermal Research* **78**, 185-208.  
46  
47  
48 Nairn, I. A., Shane, P. R., Cole, J. W., Leonard, G. J., Self, S. & Pearson, N. (2004). Rhyolite  
49  
50 magma processes of the ~AD 1315 Kaharoa eruption episode, Tarawera volcano, New  
51  
52 Zealand. *Journal of Volcanology and Geothermal Research* **131**, 265-294.  
53  
54  
55 Nelson, S. T. & Montana, A. (1992). Sieve-textured plagioclase in volcanic rocks produced  
56  
57 by rapid decompression. *American Mineralogist* **77**, 1242-1249.  
58  
59  
60

- 1  
2  
3 Ninkovich, D. (1968). Pleistocene volcanic eruptions in New Zealand recorded in deep-sea  
4  
5 sediments. *Earth and Planetary Science Letters* **4**, 89-102.  
6  
7 Perkins, M. E. & Nash, W. P. (2002). Explosive silicic volcanism of the Yellowstone hotspot:  
8  
9 the ash fall tuff record. *Geological Society of America Bulletin* **114**, 367-381.  
10  
11 Price, R. C., Mortimer, N., Smith, I. E. M. & Maas, R. (2015). Whole-rock geochemical  
12  
13 reference data for Torlesse and Waipapa terranes, North Island, New Zealand. *New*  
14  
15 *Zealand Journal of Geology and Geophysics* **58**, 213-228.  
16  
17 Pritchard, C. J. & Larson, P. B. (2012). Genesis of the post-caldera eastern Upper Basin  
18  
19 Member rhyolites, Yellowstone, WY: from volcanic stratigraphy, geochemistry and  
20  
21 radiogenic isotope modeling. *Contributions to Mineralogy and Petrology* **164**, 205-  
22  
23 228.  
24  
25 Putirka, K. D. (2008). Thermometers and barometers for volcanic systems. *Reviews in*  
26  
27 *Mineralogy and Geochemistry* **69**, 61-120.  
28  
29 Putirka, K. (2016). Amphibole thermometers and barometers for igneous systems, and some  
30  
31 implications for eruption mechanisms of felsic magmas at arc volcanoes. *American*  
32  
33 *Mineralogist* **101**, (in press: doi:10.2138/am-2016-5506).  
34  
35 Ridolfi, F., Renzulli, A. & Puerini, M. (2010). Stability and chemical equilibrium of  
36  
37 amphibole in calc-alkaline magmas: an overview, new thermobarometric formulations  
38  
39 and application to subduction-related volcanoes. *Contributions to Mineralogy and*  
40  
41 *Petrology* **160**, 45-66.  
42  
43 Rogan, A. M. (1982). A geophysical study of the Taupo Volcanic Zone, New Zealand.  
44  
45 *Journal of Geophysical Research* **87**, 4073-4088.  
46  
47 Rotella, M. D., Wilson, C. J. N., Barker, S. J., Schipper, C. I., Wright, I. C. & Wysoczanski,  
48  
49 R. J. (2015). Dynamics of deep submarine silicic explosive eruptions in the Kermadec  
50  
51 arc, as reflected in pumice vesicularity textures. *Journal of Volcanology and*  
52  
53  
54  
55  
56  
57  
58  
59  
60



- 1  
2  
3 *Geothermal Research* **301**, 314-332.
- 4  
5 Schuraytz, B. C., Vogel, T. A. & Younker, L. W. (1989). Evidence for dynamic withdrawal  
6  
7 from a layered magma body: the Topopah Spring Tuff, southwestern Nevada. *Journal*  
8  
9 *of Geophysical Research* **94**, 5925-5942.
- 10  
11 Self, S., Goff, F., Gardner, J. N., Wright, J. V. & Kite, W. M. (1986). Explosive rhyolitic  
12  
13 volcanism in the Jemez Mountains: vent locations, caldera development and relation  
14  
15 to regional structure. *Journal of Geophysical Research* **91**, 1779-1798.
- 16  
17 Shane, P. A. R. (1994). A widespread, early Pleistocene tephra (Potaka tephra, 1 Ma) in New  
18  
19 Zealand: character, distribution, and implications. *New Zealand Journal of Geology*  
20  
21 *and Geophysics* **37**, 25-35.
- 22  
23 Shane, P., Smith, V. C., Lowe, D. J. & Nairn, I. A. (2003). Re-identification of c. 15 700 cal  
24  
25 yr BP tephra bed at Kaipo Bog, eastern North Island: implications for dispersal of  
26  
27 Rotorua and Puketarata tephra beds. *New Zealand Journal of Geology and Geophysics*  
28  
29 **46**, 591-596.
- 30  
31 Shane, P., Martin, S. B., Smith, V. C., Beggs, K. F., Darragh, M. B., Cole, J. W. & Nairn, I.  
32  
33 A. (2007). Multiple rhyolite magmas and basalt injection in the 17.7 ka Rerewhakaaitu  
34  
35 eruption episode from Tarawera volcanic complex, New Zealand. *Journal of*  
36  
37 *Volcanology and Geothermal Research* **164**, 1-26.
- 38  
39 Shane, P., Nairn, I. A., Smith, V. C., Darragh, M., Beggs, K., & Cole, J. W. (2008a). Silicic  
40  
41 recharge of multiple rhyolite magmas by basaltic intrusion during the 22.6 ka Okareka  
42  
43 eruption episode, New Zealand. *Lithos* **103**, 527-549.
- 44  
45 Shane, P., Nairn, I. A., Martin, S. B. & Smith, V. C. (2008b). Compositional heterogeneity in  
46  
47 tephra deposits resulting from the eruption of multiple magma bodies: implications for  
48  
49 tephrochronology. *Quaternary International* **178**, 44-53.
- 50  
51  
52  
53  
54  
55  
56 Simon, J. & Reid, M. R. (2005). The pace of rhyolite differentiation and storage in an  
57  
58  
59  
60

- 1  
2  
3 'archetypical' silicic magma system, Long Valley, California. *Earth and Planetary*  
4  
5 *Science Letters* **235**, 123-140.  
6  
7 Singer, B. S. (2014). A Quaternary geomagnetic instability time scale. *Quaternary*  
8  
9 *Geochronology* **21**, 29-52.  
10  
11 Smith, R. L. (1979). Ash-flow magmatism. In: Chapin, C. E. & Elston, W. E. (Eds.) *Ash-flow*  
12  
13 *tuffs. Geological Society of America Special Paper* **180**, 5-27.  
14  
15 Smith, R. L. & Bailey, R. A. (1966). The Bandelier Tuff: a study of ash-flow eruption cycles  
16  
17 from zoned magma chambers. *Bulletin Volcanologique* **29**, 83-103.  
18  
19 Sparks, R. S. J., Sigurdsson, H. & Wilson, L. (1977). Magma mixing: a mechanism for  
20  
21 triggering acid explosive eruptions. *Nature* **267**, 315-318.  
22  
23 Stern, T. A. (1979). Regional and residual gravity fields, central North Island, New Zealand.  
24  
25 *New Zealand Journal of Geology and Geophysics* **22**, 479-485.  
26  
27 Stix, J., Goff, F., Gorton, M. P., Heiken, G. & Garcia, S. R. (1988). Restoration of  
28  
29 compositional zonation in the Bandelier silicic magma chamber between two caldera-  
30  
31 forming eruptions: geochemistry and origin of the Cerro Toledo Rhyolite, Jemez  
32  
33 Mountains, New Mexico. *Journal of Geophysical Research* **93**, 6129-6147.  
34  
35 Sutton, A., Blake, S. & Wilson, C. J. N. (1995). An outline geochemistry of rhyolite eruptives  
36  
37 from Taupo volcanic centre, New Zealand. *Journal of Volcanology and Geothermal*  
38  
39 *Research* **68**, 153-175.  
40  
41 Tanaka, H., Turner, G. M., Houghton, B. F., Tachibana, T., Kono, M., McWilliams, M. O.  
42  
43 (1996). Palaeomagnetism and chronology of the central Taupo Volcanic Zone, New  
44  
45 Zealand. *Geophysics Journal International* **124**, 919-934.  
46  
47  
48  
49  
50 Tsuchiyama, A. (1985). Dissolution kinetics of plagioclase in the melt of the system diopside-  
51  
52 albite-anorthite, and origin of dusty plagioclase in andesites. *Contributions to*  
53  
54 *Mineralogy and Petrology* **89**, 1-16.  
55  
56  
57  
58  
59  
60

- 1  
2  
3 Turner, E. P. (1928). A brief account of the re-establishment of vegetation on Tarawera  
4  
5 Mountain since the eruption of 1886. *Transactions of the New Zealand Institute* **59**,  
6  
7 60-66.  
8
- 9  
10 Waters, L. E. & Lange, R. A. (2015). An updated calibration of the plagioclase-liquid  
11  
12 hygrometer-thermometer applicable to basalts through rhyolites. *American*  
13  
14 *Mineralogist* **100**, 2172-2184.  
15
- 16  
17 Watts, K. E., Bindeman, I. N. & Schmitt, A. K. (2012). Crystal scale anatomy of a dying  
18  
19 supervolcano: an isotope and geochronology study of individual phenocrysts from  
20  
21 voluminous rhyolites of the Yellowstone caldera. *Contributions to Mineralogy and*  
22  
23 *Petrology* **164**, 45-67.  
24
- 25  
26 Wilson, C. J. N. (1986). Reconnaissance stratigraphy and volcanology of ignimbrites from  
27  
28 Mangakino volcano. In: Smith, I. E. M. (Ed.) *Late Cenozoic Volcanism in New*  
29  
30 *Zealand. Royal Society of New Zealand Bulletin* **23**, 179-193.  
31
- 32  
33 Wilson, C. J. N. (1993). Stratigraphy, chronology, styles and dynamics of late Quaternary  
34  
35 eruptions from Taupo volcano, New Zealand. *Philosophical Transactions of the Royal*  
36  
37 *Society of London A***343**, 205-306.  
38
- 39  
40 Wilson, C. J. N. & Charlier, B. L. A. (2009). Rapid rates of magma generation at  
41  
42 contemporaneous magma systems, Taupo volcano, New Zealand: insights from U-Th  
43  
44 model-age spectra in zircons. *Journal of Petrology* **50**, 875-907.  
45
- 46  
47 Wilson, C. J. N., Rogan, A. M., Smith, I. E. M., Northey, D. J., Nairn, I. A. & Houghton, B.  
48  
49 F. (1984). Caldera volcanoes of the Taupo Volcanic Zone, New Zealand. *Journal of*  
50  
51 *Geophysical Research* **89**, 8463-8484.  
52
- 53  
54 Wilson, C. J. N., Houghton, B. F., Kamp, P. J. J. & McWilliams, M. O. (1995a). An  
55  
56 exceptionally widespread ignimbrite with implications for pyroclastic flow  
57  
58 emplacement. *Nature* **378**, 605-607.  
59  
60

- 1  
2  
3 Wilson, C. J. N., Houghton, B. F., McWilliams, M. O., Lanphere, M. A., Weaver, S. D. &  
4  
5 Briggs, R. M. (1995b). Volcanic and structural evolution of Taupo Volcanic Zone,  
6  
7 New Zealand: a review. *Journal of Volcanology and Geothermal Research* **68**, 1-28.  
8  
9  
10 Wilson, C. J. N., Blake, S., Charlier, B. L. A. & Sutton, A. N. (2006). The 26.5 ka Oruanui  
11  
12 eruption, Taupo volcano, New Zealand: development, characteristics and evacuation  
13  
14 of a large rhyolitic magma body. *Journal of Petrology* **47**, 35-69  
15  
16  
17 Wilson, C. J. N., Charlier, B. L. A., Fagan, C. J., Spinks, K. D., Gravley, D. M., Simmons, S.  
18  
19 F. & Browne, P. R. L. (2008). U-Pb dating of zircon in hydrothermally altered rocks  
20  
21 as a correlation tool: application to the Mangakino geothermal field, New Zealand.  
22  
23 *Journal of Volcanology and Geothermal Research* **176**, 191-198  
24  
25  
26 Wilson, C. J. N., Gravley, D. M., Leonard, G. S. & Rowland, J. V. (2009). Volcanism in the  
27  
28 central Taupo Volcanic Zone, New Zealand: tempo styles and controls. In:  
29  
30 Thordarson, T., Self, S., Larsen, G., Rowland, S. K. & Hoskuldsson, A. (Eds.), *Studies*  
31  
32 *in Volcanology: The Legacy of George Walker. Special Publications of IAVCEI* **2**,  
33  
34 225-247.  
35  
36  
37 Wolff, J. A., Ramos, F. C. & Davidson, J. P. (1999). Sr isotope disequilibrium during  
38  
39 differentiation of the Bandelier Tuff: constraints on the crystallization of a large  
40  
41 rhyolitic magma chamber. *Geology* **27**, 495-498.  
42  
43  
44 Wolff, J. A., Brunstad, K. A. & Gardner, J. N. (2011). Reconstruction of the most recent  
45  
46 volcanic eruptions from the Valles caldera, New Mexico. *Journal of Volcanology and*  
47  
48 *Geothermal Research* **199**, 53-68.  
49  
50  
51  
52  
53  
54  
55  
56  
57  
58  
59  
60

### Figure Captions

- 1  
2  
3  
4  
5 **Fig. 1.** Map of the North Island, New Zealand showing the extent of the Kidnappers and  
6 Rocky Hill ignimbrites and sampling locations. The thick dashed line marks the  
7 boundary of the old TVZ. Modified from Briggs *et al.* (1993) and Wilson *et al.*  
8 (1995b).  
9  
10  
11  
12  
13  
14 **Fig. 2.** Images to show the typical field relationships of the Kidnappers and Rocky Hill  
15 deposits. (a) Contrasts between the natural exposures of the Rocky Hill ignimbrite  
16 and the temporary or artificial exposures of the Kidnappers deposits. Road cutting  
17 is at 38.562259°S, 175.417357°E. (b) Exposure in a road cutting at 38.567042°S,  
18 175.464727°E that shows the erosional nature of the contact between the  
19 Kidnappers and Rocky Hill ignimbrites.  
20  
21  
22  
23  
24  
25  
26  
27  
28 **Fig. 3.** Diagrammatic catalogue of samples from the Kidnappers fall deposit, Kidnappers  
29 ignimbrite and Rocky Hill ignimbrite chosen for crystal-specific studies and glass  
30 analyses. Kidnappers fall samples are ordered in stratigraphic height through the  
31 proximal fall deposit. Pumice from the ignimbrites are arranged by whole-rock  
32 compositional groups (SiO<sub>2</sub> wt.%) and are without stratigraphic control. The  
33 colours assigned to compositional groups are used in all figures throughout this  
34 paper. Note that the stratigraphic heights covered by the term 'other' (light blue)  
35 contain material from KF-C, as well KF-A and KF-B fall deposit compositional  
36 groups. Major element analyses are indicated with a 'm', and trace element  
37 analyses are denoted by a 't'.  
38  
39  
40  
41  
42  
43  
44  
45  
46  
47  
48  
49  
50 **Fig. 4.** Plots of whole-rock (circles) and matrix glass (triangles) major oxide abundances  
51 against silica for all analysed Kidnappers single pumice clasts. Tie-lines connect  
52 whole-rock–glass pairs. Crosses represent whole-rock 2 sd XRF uncertainties (left  
53 hand side) and 2 sd EPMA matrix glass uncertainties (right hand side) (Electronic  
54  
55  
56  
57  
58  
59  
60

1  
2  
3 Appendix 1). Colours of the symbols indicate the compositional groups assigned  
4  
5 to each pumice (KI-1 = red, KI-2 = green, KI-3 = blue; Fig. 3). Mineral  
6  
7 accumulation vectors are shown to highlight influence of the variable crystal  
8  
9 content on pumice whole-rock concentrations (p=plagioclase, a=amphibole,  
10  
11 o=opx, b=biotite).

12  
13  
14 **Fig. 5.** Plots of selected trace elements versus silica (a–c), K<sub>2</sub>O (d) and Al<sub>2</sub>O<sub>3</sub> (e, f) for  
15  
16 pumice whole-rock and matrix glass from Kidnappers pumice. Tie-lines connect  
17  
18 whole-rock–glass pairs. Crosses represent 2 sd whole-rock solution ICPMS  
19  
20 uncertainties (Electronic Appendix 1). Colours of the symbols indicate the  
21  
22 compositional groups assigned to each pumice (KI-1 = red, KI-2 = green, KI-3 =  
23  
24 blue; Fig. 3).

25  
26  
27 **Fig. 6.** Selected major and trace element plots of Kidnappers matrix glass. Each data  
28  
29 point represents a single matrix glass analysis. Spots are divided into three groups  
30  
31 based on whole-rock compositional groups (KI-1, KI-2 and KI-3; Fig. 3), and  
32  
33 shaded areas highlight the compositional range covered by the glass  
34  
35 compositional groups in the Kidnappers fall deposit identified in Cooper *et al.*  
36  
37 (2012) (KF-A = red, KF-B = green, KF-C = light blue (KF-C contains KF-C glass  
38  
39 and variable proportions of KF-A and KF-B; see Cooper *et al.*, 2012 and Fig. 3).

40  
41  
42 **Fig. 7.** Plots of whole-rock (diamonds) and matrix glass (triangles) major element  
43  
44 abundances against silica for all analysed Rocky Hill single pumice clasts. Tie-  
45  
46 lines connect whole-rock–glass pairs. The range of Kidnappers data is shown by  
47  
48 the coloured areas (KI-1 = red, KI-2 = green, KI-3 = blue; Fig. 3) for whole-rock  
49  
50 analyses and grey areas (glass analyses). Crosses represent whole-rock 2 sd XRF  
51  
52 analyses and grey areas (glass analyses). Crosses represent whole-rock 2 sd XRF  
53  
54 uncertainties (left hand side) and 2 sd EPMA matrix glass uncertainties (right  
55  
56 hand side) (Electronic Appendix 1).

- 1  
2  
3 **Fig. 8.** Plots of selected trace elements versus silica (a–c), K<sub>2</sub>O (d) and Al<sub>2</sub>O<sub>3</sub> (e,f) for  
4  
5 pumice whole-rock and matrix glass from Rocky Hill pumices. Tie-lines connect  
6  
7 whole-rock–glass pairs. Crosses represent 2 sd whole-rock solution ICPMS  
8  
9 uncertainties (Electronic Appendix 1). Colours of the symbols indicate the  
10  
11 compositional groups to which pumices are assigned (RH-1 = red, RH-2 = green;  
12  
13 Fig. 3).  
14  
15
- 16 **Fig. 9.** Plots of selected major and trace elements of Rocky Hill matrix glass. Each data  
17  
18 point represents a single matrix glass analysis. Spots are divided into two groups  
19  
20 based on whole-rock compositional groups. Coloured shaded areas represent the  
21  
22 corresponding ranges covered by matrix glass compositional groups within  
23  
24 Kidnappers pumice (KI-1 = red, KI-2 = green, KI-3 = blue; Fig. 3).  
25  
26
- 27 **Fig. 10.** Summary of textural features (based on BSE imaging) of Kidnappers and Rocky  
28  
29 Hill plagioclase grains from each pumice compositional group. Plagioclase grains  
30  
31 are divided into three populations based on the BSE intensity change from  
32  
33 intermediate domains to outermost rims. ‘Light rims’ and ‘dark rims’ are grains  
34  
35 that have prominent outermost rims that are either lighter or darker than their  
36  
37 interior domains. ‘Non-distinct rims’ do not show a significant change in  
38  
39 brightness from their associated interior domains.  
40  
41  
42
- 43 **Fig. 11.** Summary of textural features (based on BSE imaging) of Kidnappers and Rocky  
44  
45 Hill orthopyroxene grains from each pumice compositional group. Normally  
46  
47 zoned orthopyroxenes are those with darker (higher En) cores and lighter (lower  
48  
49 En) outer zones. Nominally unzoned grains do not show any significant  
50  
51 compositional zonation, although some streaky discontinuous zoning may be  
52  
53 present. Reversely zoned grains have lighter (lower En) cores and darker (higher  
54  
55 En) outer zones. Patchy grains display a range of compositions but zoning is  
56  
57  
58  
59  
60



1  
2  
3 discontinuous and no core–rim relationships are observed. Bar charts show the  
4 proportions of grain populations within each compositional group. A dark exterior  
5 zone (e) may be superimposed on any of the four textures, and the proportions of  
6 grains with dark exteriors (as a percentage of total orthopyroxene grains) are  
7 shown.  
8  
9  
10  
11  
12

13  
14 **Fig. 12.** Summary plots of mineral composition for plagioclase, orthopyroxene and  
15 amphibole from the Kidnappers fall deposit (a–c) versus stratigraphic height in  
16 the fall deposit where sampled (Fig. 3), Kidnappers ignimbrite (d–f) and Rocky  
17 Hill ignimbrite (g–i) versus the compositions of their host pumices. Dashed lines  
18 mark divisions between glass compositional groups in the Kidnappers fall deposit  
19 and pumice compositional groups within the Kidnappers and Rocky Hill  
20 ignimbrites.  
21  
22  
23  
24  
25  
26  
27  
28

29  
30 **Fig. 13.** In situ Or (mol.%) and trace element compositions versus An (mol.%) of  
31 plagioclase from the Kidnappers fall deposit (a–c), Kidnappers ignimbrite (d–f)  
32 and Rocky Hill ignimbrite (g–i).  
33  
34  
35

36  
37 **Fig. 14.** In situ major and trace element compositions of orthopyroxenes from the  
38 Kidnappers fall (a–c), Kidnappers ignimbrite (d–f) and Rocky Hill ignimbrite (g–  
39 i).  
40  
41  
42

43  
44 **Fig. 15.** In situ major and trace element compositions of amphiboles from the Kidnappers  
45 fall deposit (a–c), Kidnappers ignimbrite (d–f) and Rocky Hill ignimbrite (g–i).  
46 Approximate position of inflection points discussed in the text are marked with  
47 dashed lines.  
48  
49  
50

51  
52 **Fig. 16.** Stacked histograms of amphibole core and rim apparent temperatures (°C) and  
53 pressures (MPa) from each compositional group within Kidnappers and Rocky  
54 Hill pumices and horizons where the KF-A and KF-B glass compositional groups  
55  
56  
57  
58  
59  
60

1  
2  
3 dominate the material within the fall deposit (Fig. 3). Apparent amphibole  
4  
5 temperatures and pressures were calculated using the method of Ridolfi *et al.*  
6  
7 (2010).  
8

9  
10 **Fig. 17.** Fe–Ti oxide model temperatures and oxygen fugacities calculated using the  
11  
12 methods of Ghiorso & Evans (2008). Apparent temperatures from all Fe–Ti oxide  
13  
14 equilibrium pairs in each compositional group are displayed as stacked  
15  
16 histograms. Calculated oxygen fugacity values ( $\log f_{\text{O}_2}$ ) vs. temperature ( $^{\circ}\text{C}$ ) from  
17  
18 each compositional group are shown.  
19

20  
21 **Fig. 18.** Semi-quantitative cross sections of the Kidnappers/Rocky Hill magmatic systems  
22  
23 through time. (1) During the early stages of the Kidnappers eruption, material was  
24  
25 erupted from at least two independent magma chambers (plus the possible minor  
26  
27 KF-C magma) as a phreatomagmatic fall (Cooper *et al.*, 2012). Caldera collapse  
28  
29 probably commenced during the fall phase. (2) Eruption and deposition of  
30  
31 material deposited as flows was coincidental with wholesale caldera collapse.  
32  
33 During this period, a wider range of compositions were tapped from two,  
34  
35 heterogeneous melt-dominant bodies which had little exchange of crystals or melt.  
36  
37 A third smaller volume of melt underwent late-stage heating and mixing with a  
38  
39 more primitive, mafic melt, but did not mix with the other Kidnappers magmas.  
40  
41 (3) After a short time break the Rocky Hill eruption commenced. Two smaller  
42  
43 homogeneous melt-dominant bodies, broadly similar to Type A and B of the early  
44  
45 Kidnappers were tapped. Collapse of the chamber roof and margins incorporated  
46  
47 altered material into the melt (  
48  
49  
50  
51 red arrows). Depths are estimated from amphiboles using the method of Ridolfi *et al.* (2010).  
52  
53

54 The horizontal extents in (1) are approximately estimated from the volume of  
55  
56  
57  
58  
59  
60

1  
2  
3  
4  
5  
6  
7  
8  
9  
10  
11  
12  
13  
14  
15  
16  
17  
18  
19  
20  
21  
22  
23  
24  
25  
26  
27  
28  
29  
30  
31  
32  
33  
34  
35  
36  
37  
38  
39  
40  
41  
42  
43  
44  
45  
46  
47  
48  
49  
50  
51  
52  
53  
54  
55  
56  
57  
58  
59  
60

erupted material and the general size of the gravity anomaly that defines the Mangakino caldera.

For Peer Review

1  
2  
3 **Supplementary Fig. 1.** K<sub>2</sub>O versus Rb for Rocky Hill matrix glass and brown glass from a  
4  
5 single pumice clast. (a) BSE image of a broken plagioclase grain with associated  
6  
7 brown glass between fragments and surrounding grain. (b) Photograph of a  
8  
9 pumice chip to show the textural relationship between matrix glass and brown  
10  
11 glass, which is found in association with crystal clots.

12  
13  
14 **Supplementary Fig. 2.** Summary of textural features of plagioclase and orthopyroxene grains  
15  
16 from samples through the Kidnappers fall deposit (Cooper *et al.*, 2012). These  
17  
18 textures are discussed in the text with representative images and the proportions in  
19  
20 the ignimbrite pumices in Figs 10 and 11.

21  
22  
23 **Supplementary Fig. 3.** Stacked histograms to summarise the compositional (An mol.%)  
24  
25 relationships between plagioclase cores and rims from the each compositional  
26  
27 group in the Kidnappers fall deposit, Kidnappers ignimbrite and Rocky Hill  
28  
29 ignimbrite. Colour designations for each compositional group are the same as in  
30  
31 Fig. 3 in the main paper.

32  
33  
34 **Supplementary Fig. 4.** Stacked histograms to summarise the compositional (Wo mol.%)  
35  
36 relationship between orthopyroxene cores and rims from the Kidnappers fall  
37  
38 deposit, Kidnappers ignimbrite and Rocky Hill ignimbrite. Colour designations  
39  
40 are as in Fig. 3 in the main paper.

41  
42  
43 **Supplementary Fig. 5.** Stacked histograms to summarise the compositional relationships  
44  
45 between amphibole cores and rims from the Kidnappers fall deposit, Kidnappers  
46  
47 ignimbrite and Rocky Hill ignimbrite. Colour designations are as in Fig. 3 in the  
48  
49 main paper.

50  
51  
52 **Supplementary Fig. 6.** Stacked histograms of plagioclase–liquid and orthopyroxene–liquid  
53  
54 model temperatures from each compositional group within just the Kidnappers  
55  
56 and Rocky Hill pumices. Apparent temperatures were calculated using the  
57  
58  
59  
60

1  
2  
3 methods of Putirka (2008). Temperatures were calculated using only the rims of  
4  
5 plagioclase and orthopyroxene grains, with matrix glass compositions from the  
6  
7 same pumice clast.  
8  
9  
10  
11  
12  
13  
14  
15  
16  
17  
18  
19  
20  
21  
22  
23  
24  
25  
26  
27  
28  
29  
30  
31  
32  
33  
34  
35  
36  
37  
38  
39  
40  
41  
42  
43  
44  
45  
46  
47  
48  
49  
50  
51  
52  
53  
54  
55  
56  
57  
58  
59  
60

For Peer Review

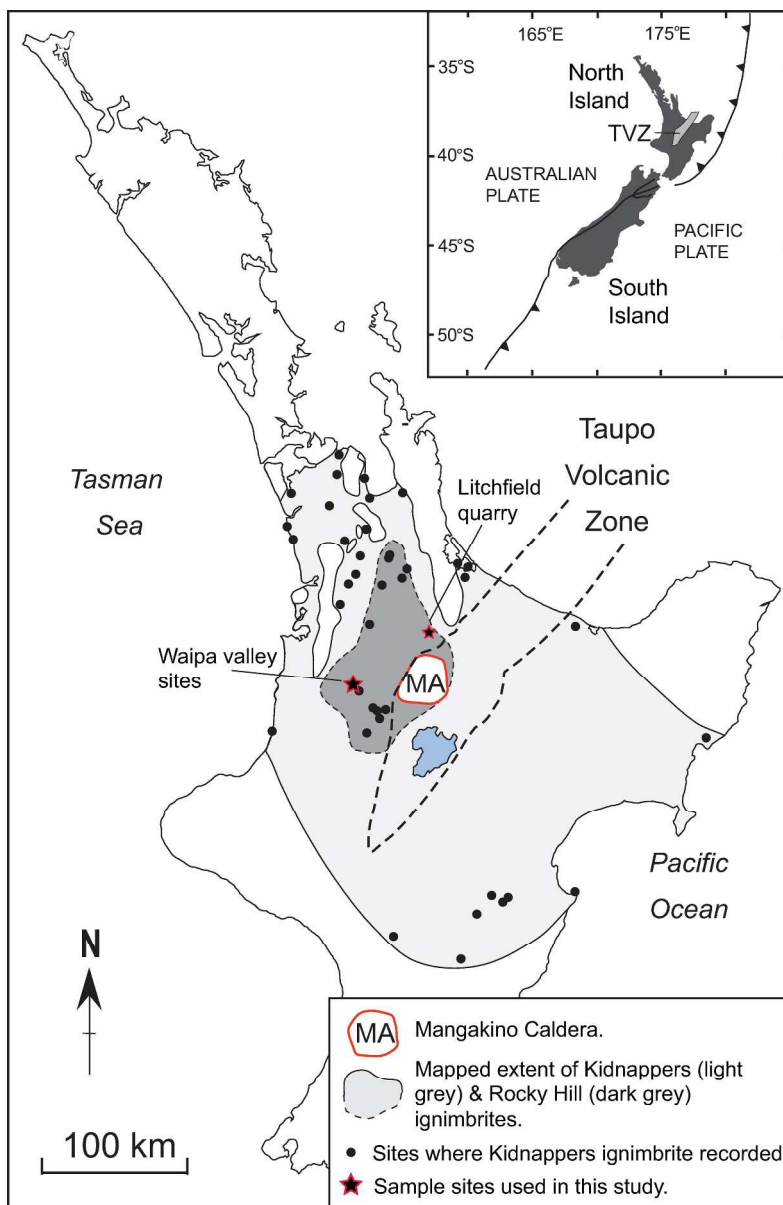


Fig.1  
210x315mm (300 x 300 DPI)

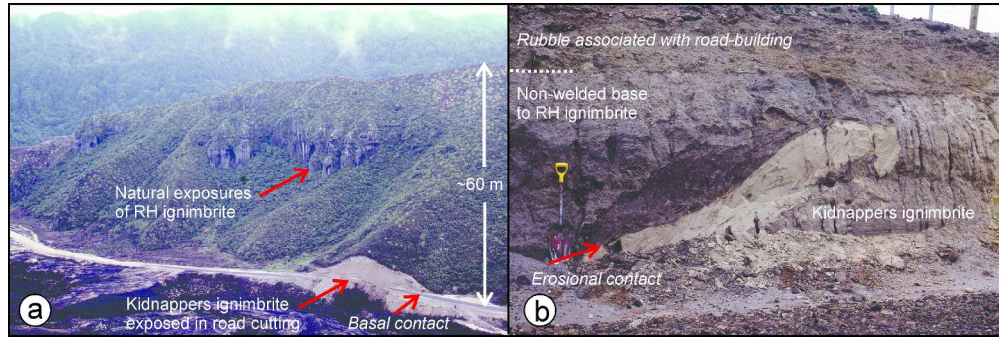


Fig. 2  
334x110mm (300 x 300 DPI)

or Peer Review



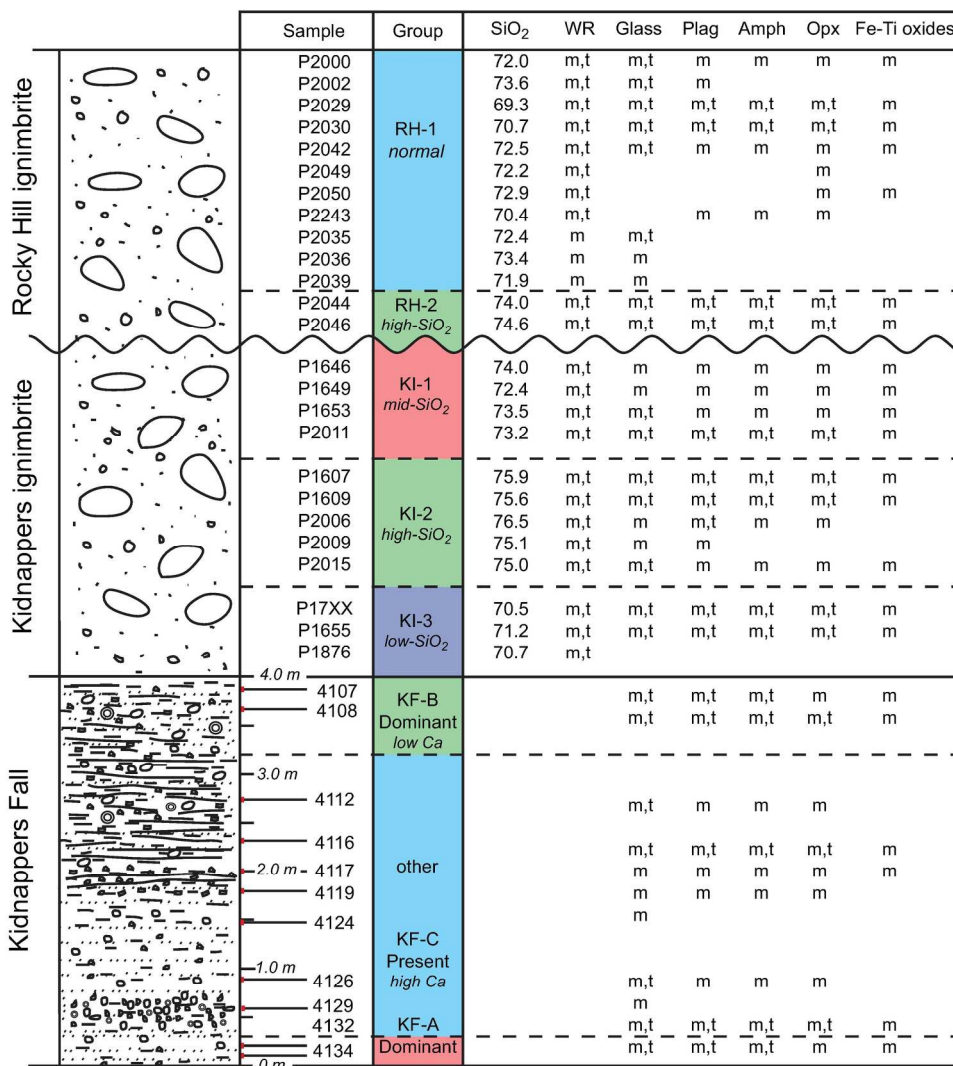


Fig. 3  
192x236mm (300 x 300 DPI)

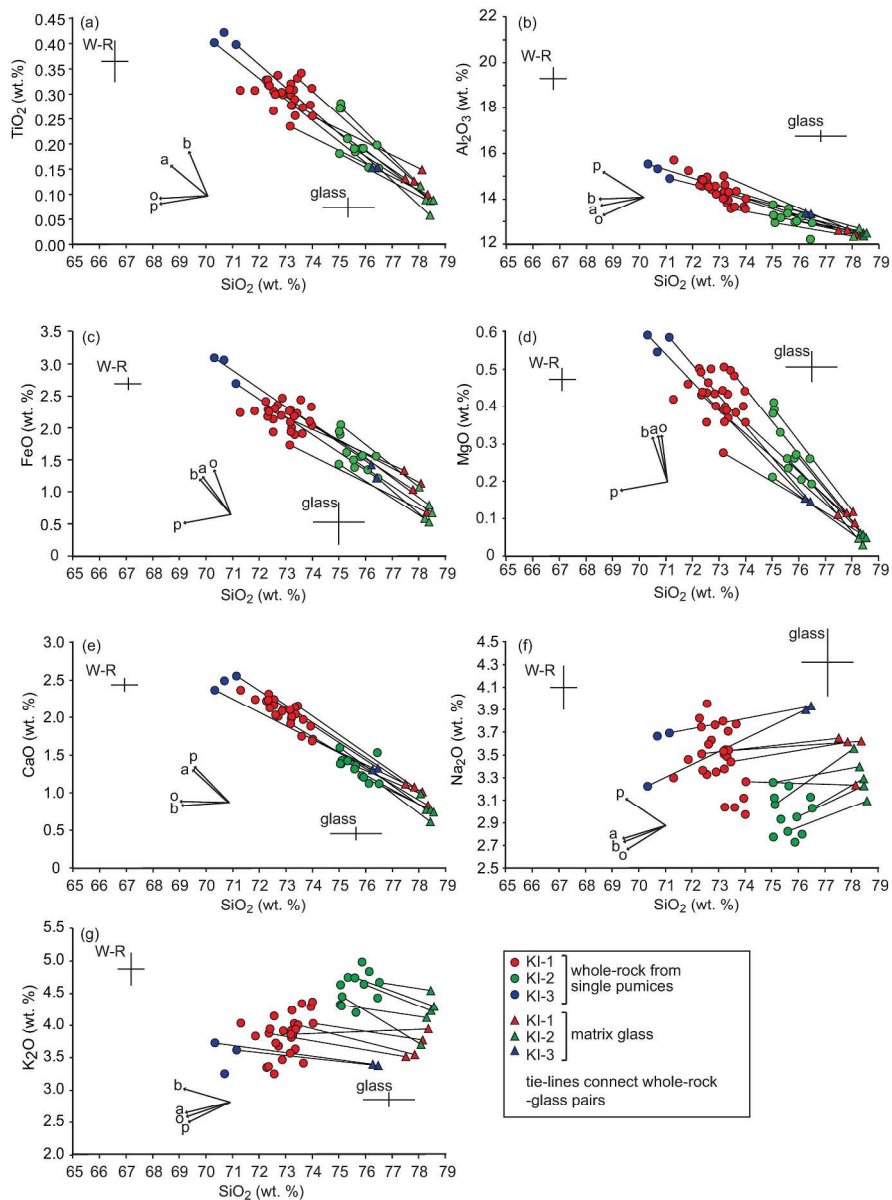


Fig. 4  
272x326mm (300 x 300 DPI)

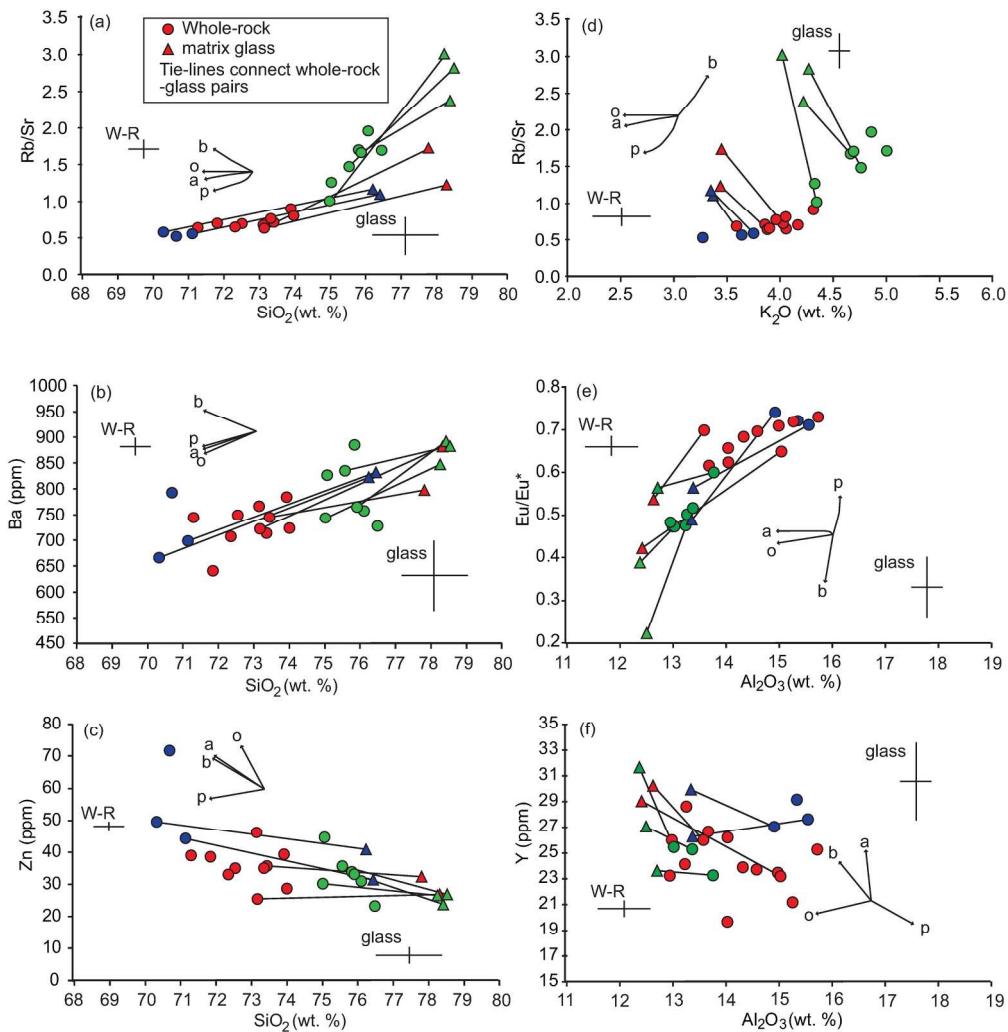


Fig. 5  
208x215mm (300 x 300 DPI)

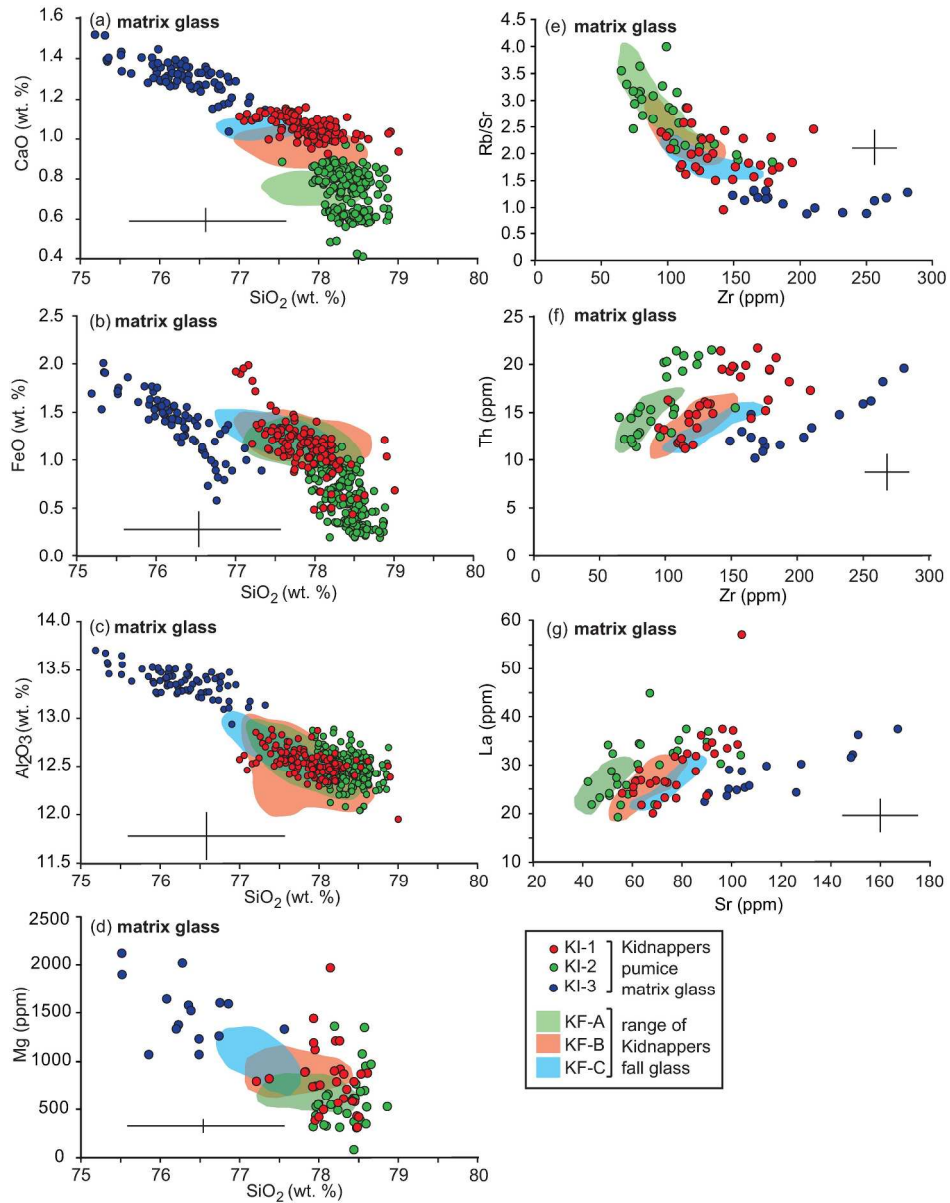


Fig. 6  
239x307mm (300 x 300 DPI)

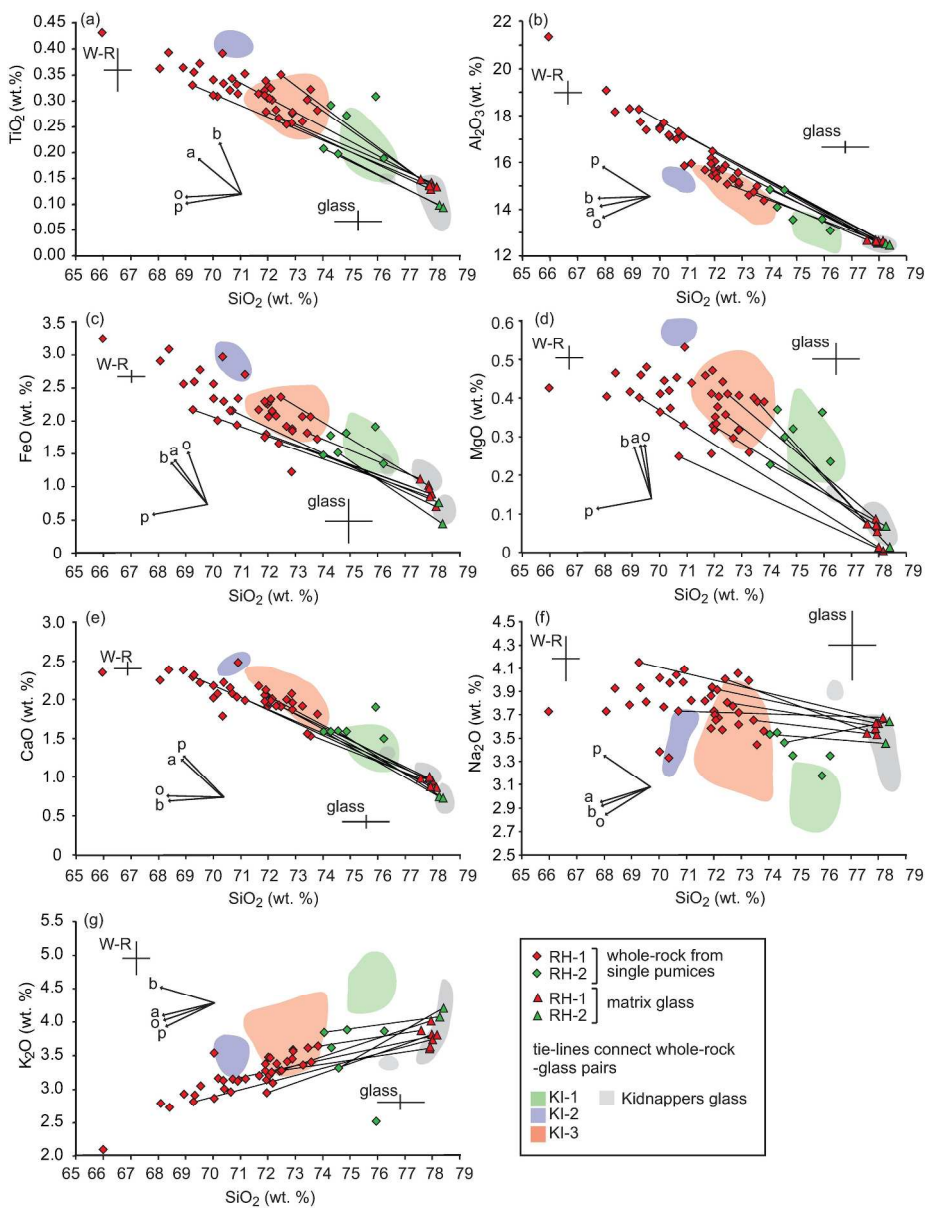


Fig. 7  
258x338mm (300 x 300 DPI)

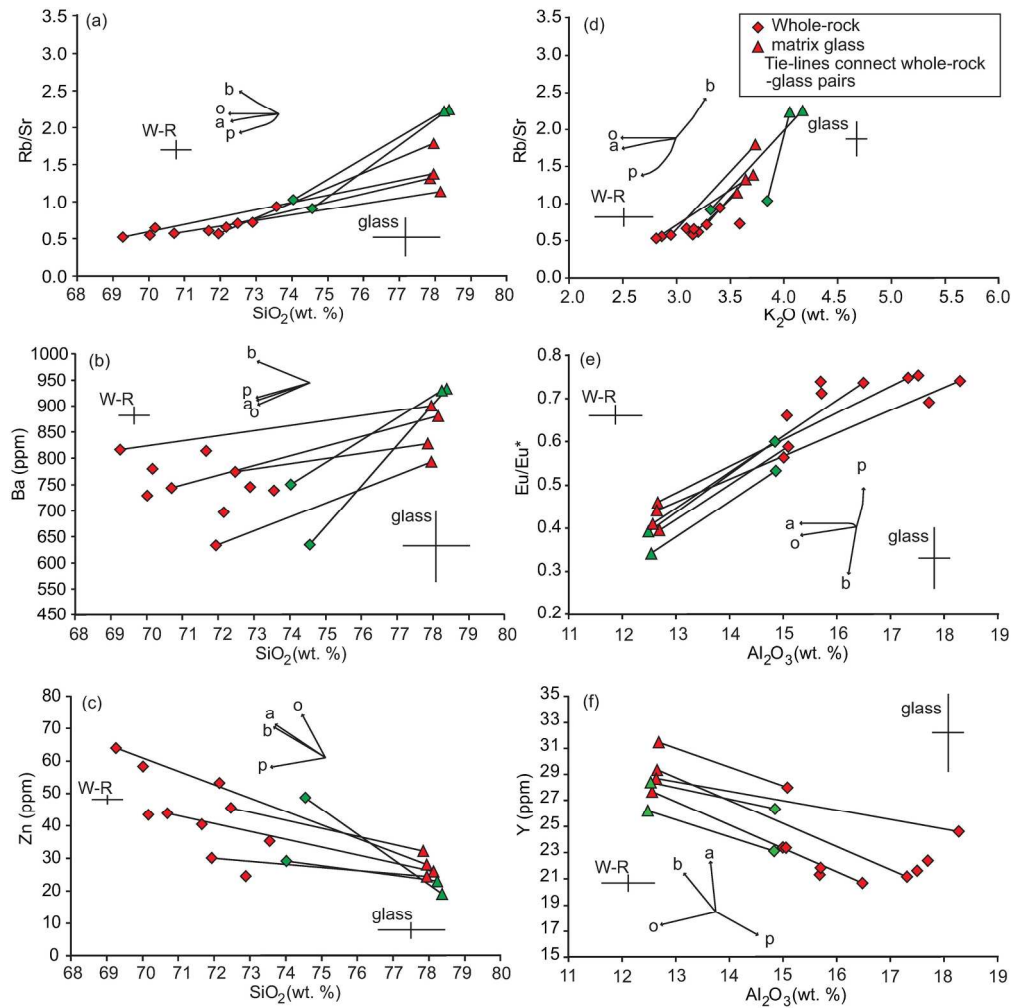


Fig. 8  
202x202mm (300 x 300 DPI)



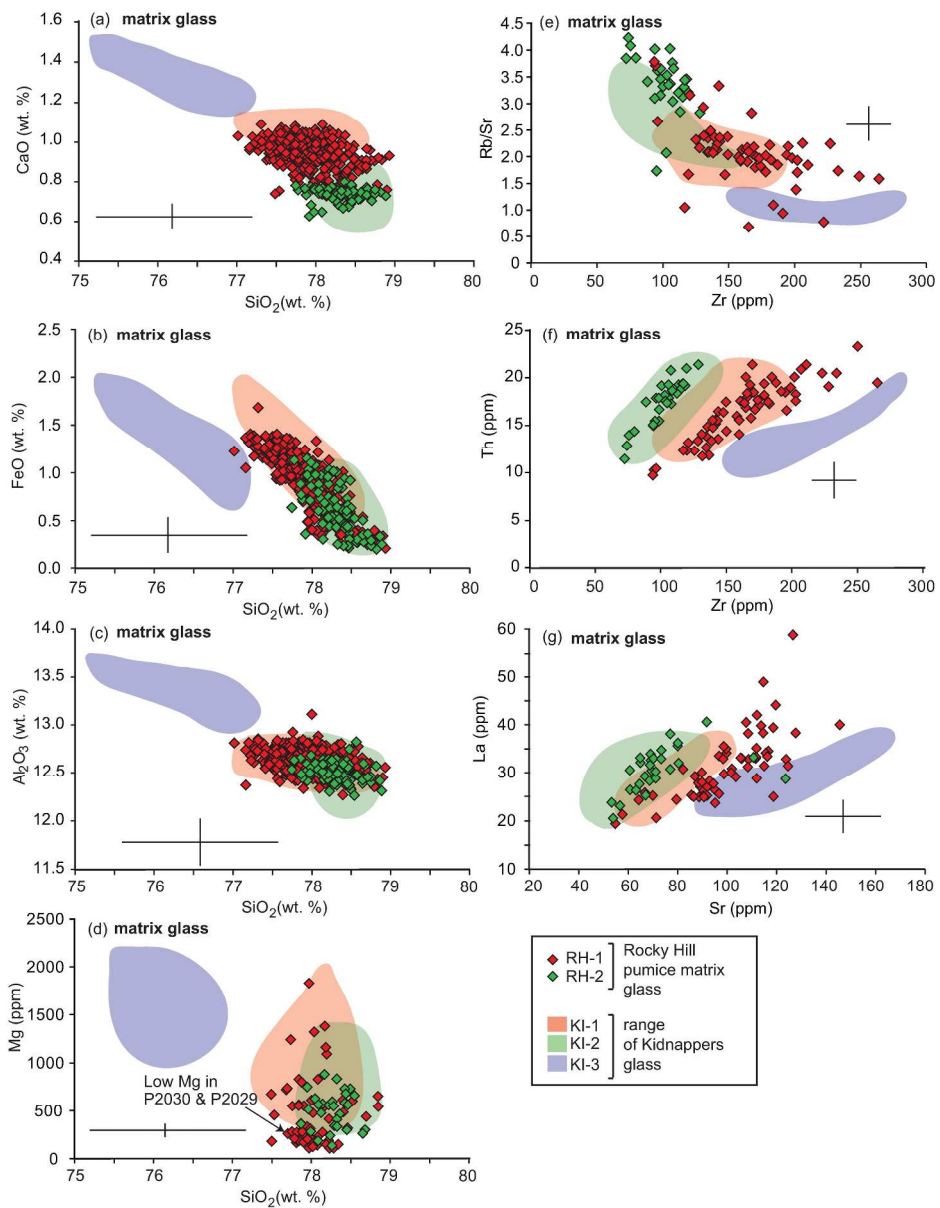


Fig. 9  
260x336mm (300 x 300 DPI)

1  
2  
3  
4  
5  
6  
7  
8  
9  
10  
11  
12  
13  
14  
15  
16  
17  
18  
19  
20  
21  
22  
23  
24  
25  
26  
27  
28  
29  
30  
31  
32  
33  
34  
35  
36  
37  
38  
39  
40  
41  
42  
43  
44  
45  
46  
47  
48  
49  
50  
51  
52  
53  
54  
55  
56  
57  
58  
59  
60

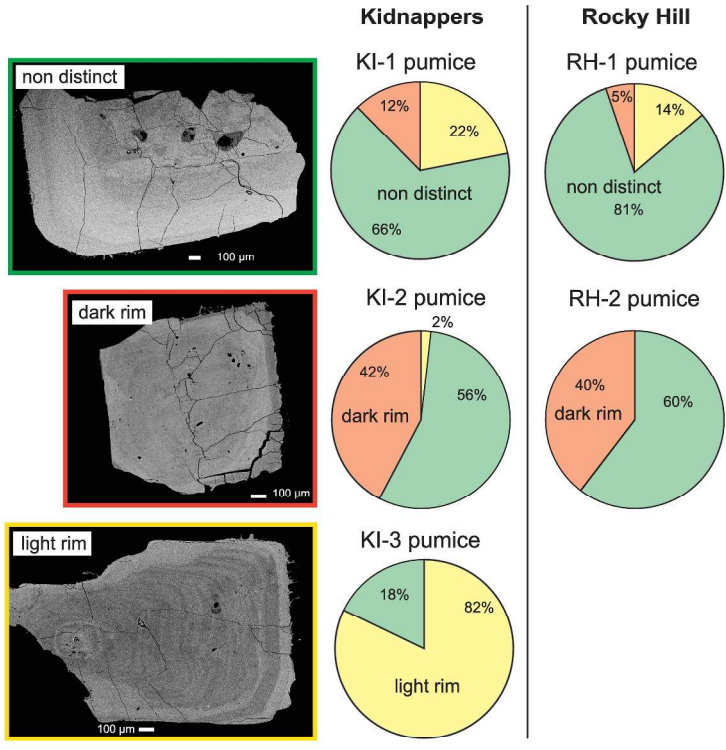


Fig. 10  
297x420mm (300 x 300 DPI)



1  
2  
3  
4  
5  
6  
7  
8  
9  
10  
11  
12  
13  
14  
15  
16  
17  
18  
19  
20  
21  
22  
23  
24  
25  
26  
27  
28  
29  
30  
31  
32  
33  
34  
35  
36  
37  
38  
39  
40  
41  
42  
43  
44  
45  
46  
47  
48  
49  
50  
51  
52  
53  
54  
55  
56  
57  
58  
59  
60

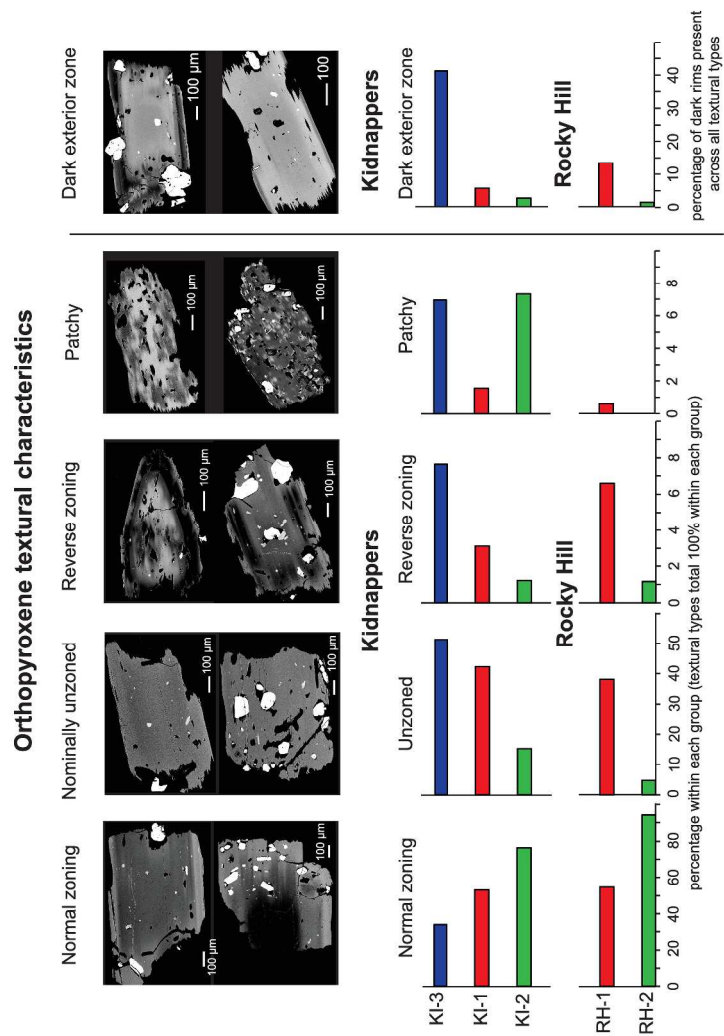


Fig. 11  
297x420mm (300 x 300 DPI)

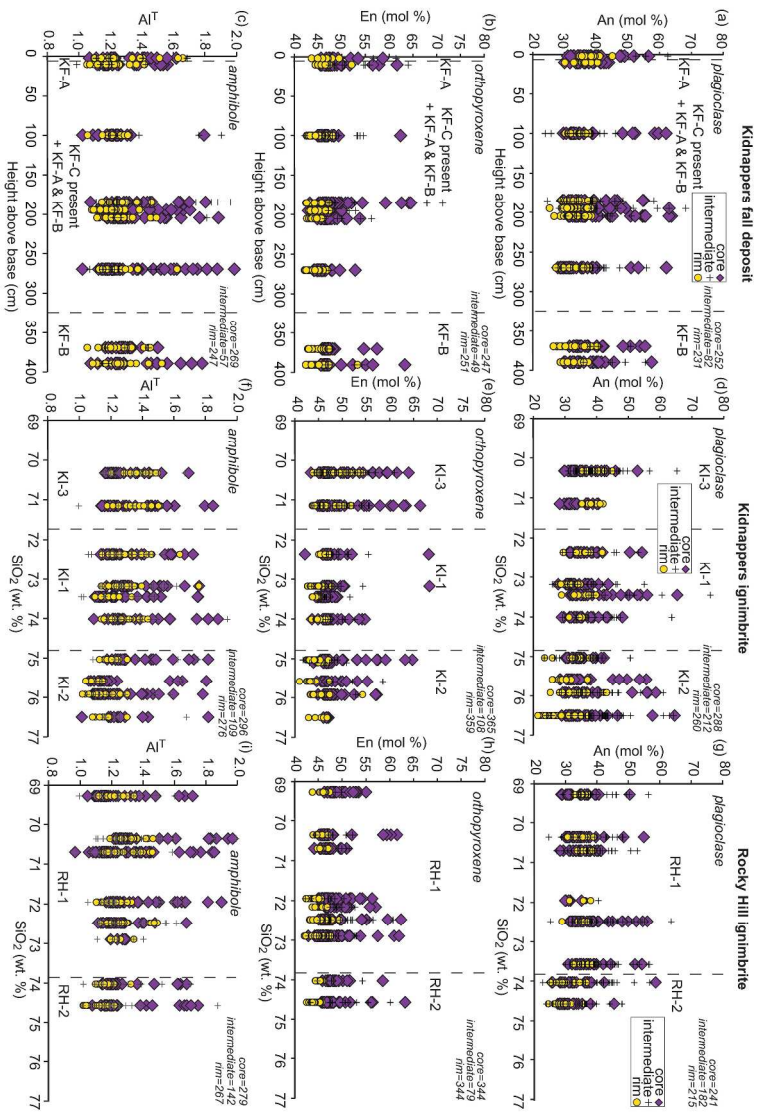


Fig. 12  
297x420mm (300 x 300 DPI)

1  
2  
3  
4  
5  
6  
7  
8  
9  
10  
11  
12  
13  
14  
15  
16  
17  
18  
19  
20  
21  
22  
23  
24  
25  
26  
27  
28  
29  
30  
31  
32  
33  
34  
35  
36  
37  
38  
39  
40  
41  
42  
43  
44  
45  
46  
47  
48  
49  
50  
51  
52  
53  
54  
55  
56  
57  
58  
59  
60

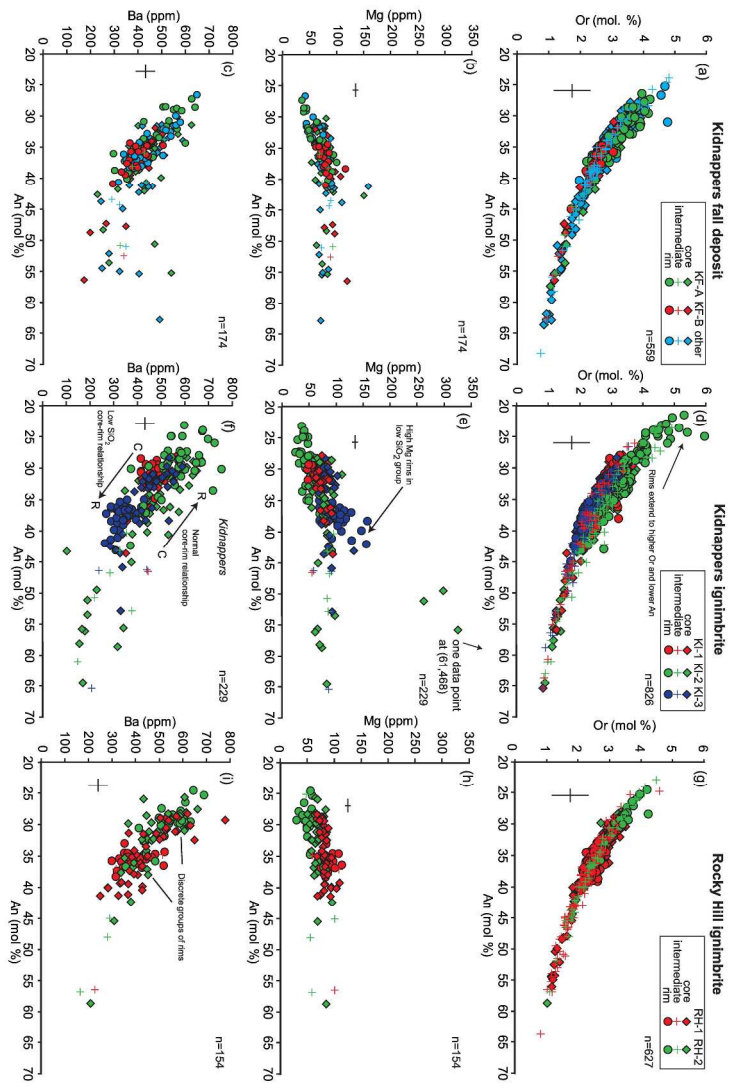


Fig. 13  
297x420mm (300 x 300 DPI)

1  
2  
3  
4  
5  
6  
7  
8  
9  
10  
11  
12  
13  
14  
15  
16  
17  
18  
19  
20  
21  
22  
23  
24  
25  
26  
27  
28  
29  
30  
31  
32  
33  
34  
35  
36  
37  
38  
39  
40  
41  
42  
43  
44  
45  
46  
47  
48  
49  
50  
51  
52  
53  
54  
55  
56  
57  
58  
59  
60

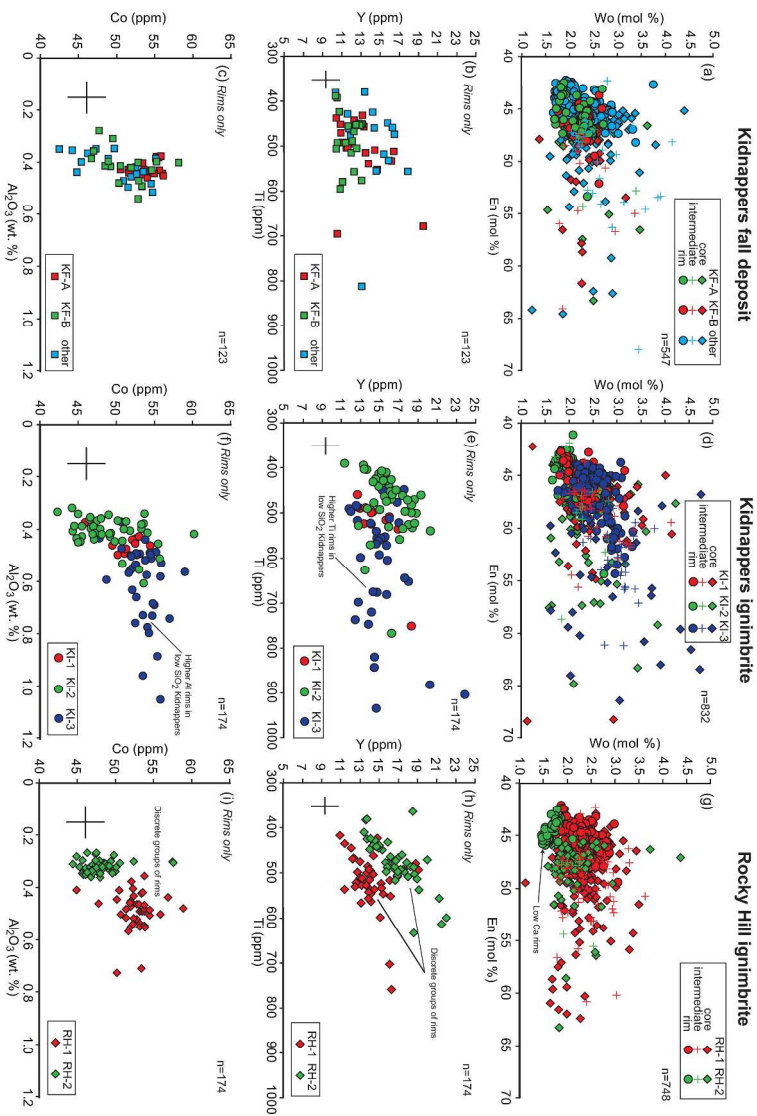


Fig. 14  
297x420mm (300 x 300 DPI)

1  
2  
3  
4  
5  
6  
7  
8  
9  
10  
11  
12  
13  
14  
15  
16  
17  
18  
19  
20  
21  
22  
23  
24  
25  
26  
27  
28  
29  
30  
31  
32  
33  
34  
35  
36  
37  
38  
39  
40  
41  
42  
43  
44  
45  
46  
47  
48  
49  
50  
51  
52  
53  
54  
55  
56  
57  
58  
59  
60

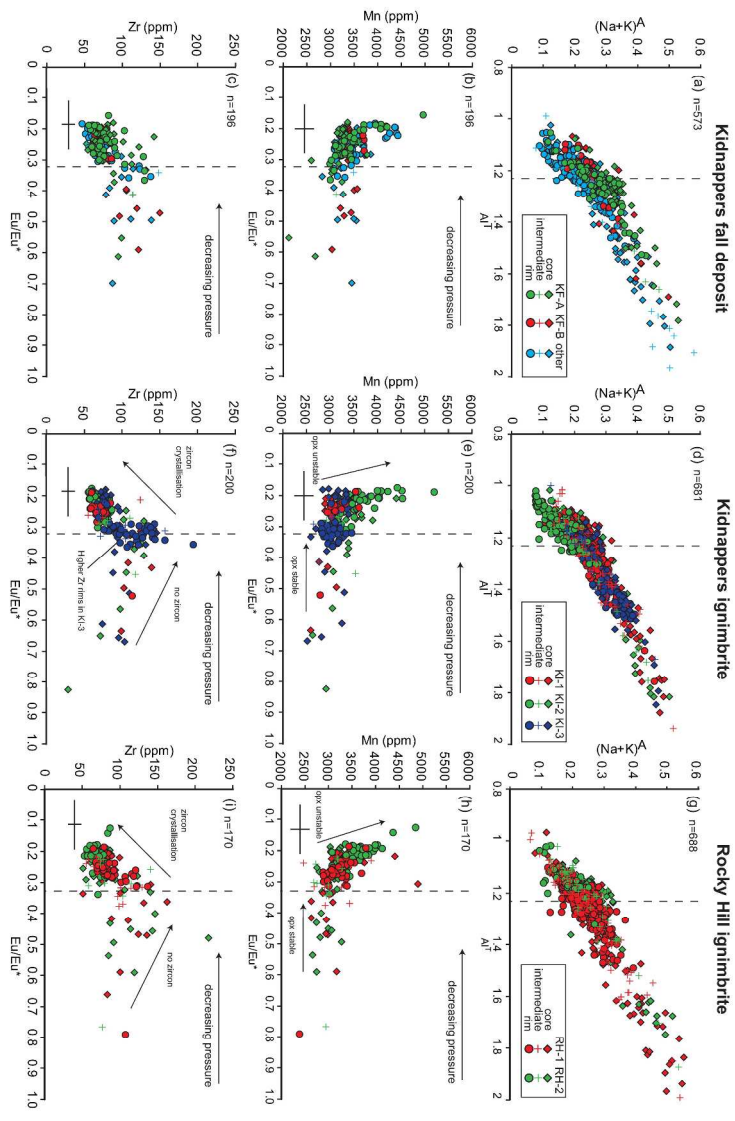


Fig. 15  
297x420mm (300 x 300 DPI)

1  
2  
3  
4  
5  
6  
7  
8  
9  
10  
11  
12  
13  
14  
15  
16  
17  
18  
19  
20  
21  
22  
23  
24  
25  
26  
27  
28  
29  
30  
31  
32  
33  
34  
35  
36  
37  
38  
39  
40  
41  
42  
43  
44  
45  
46  
47  
48  
49  
50  
51  
52  
53  
54  
55  
56  
57  
58  
59  
60

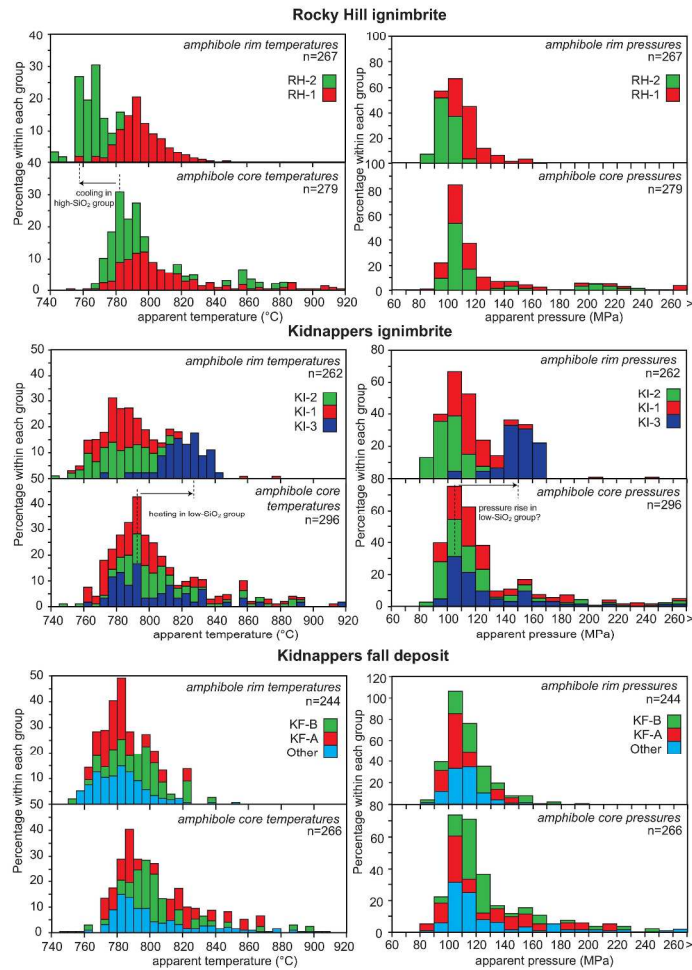


Fig. 16  
297x420mm (300 x 300 DPI)



1  
2  
3  
4  
5  
6  
7  
8  
9  
10  
11  
12  
13  
14  
15  
16  
17  
18  
19  
20  
21  
22  
23  
24  
25  
26  
27  
28  
29  
30  
31  
32  
33  
34  
35  
36  
37  
38  
39  
40  
41  
42  
43  
44  
45  
46  
47  
48  
49  
50  
51  
52  
53  
54  
55  
56  
57  
58  
59  
60

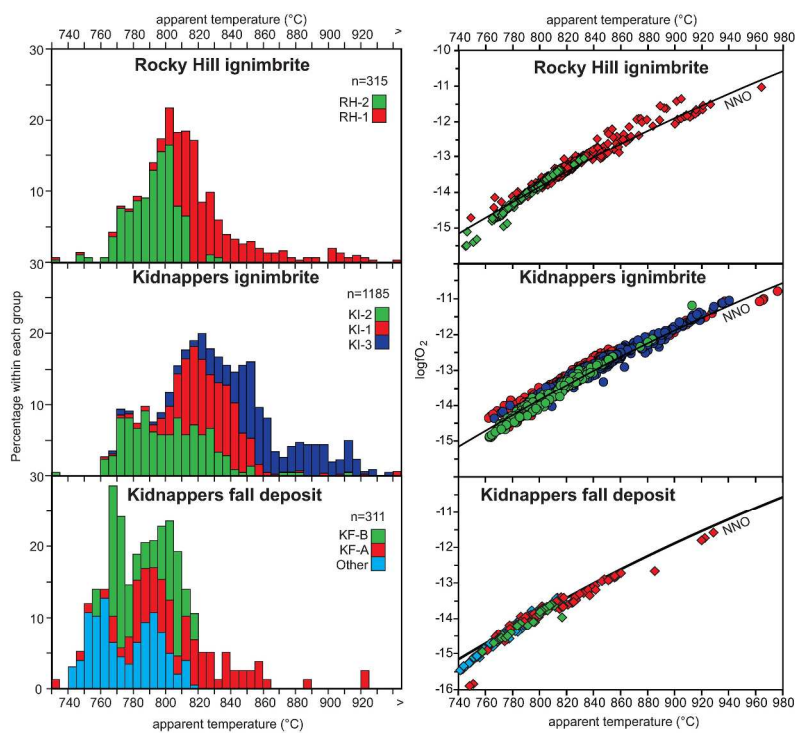


Fig. 17  
297x420mm (300 x 300 DPI)





Table 1: Mean whole-rock major and trace element concentrations for each compositional group within Kidnappers and Rocky Hill pumices

	Kidnappers pumice						Rocky Hill pumice			
	KI-1		KI-2		KI-3		RH-1		RH-2	
	72-74 wt. % SiO <sub>2</sub>		> 74.5 wt. % SiO <sub>2</sub>		< 72 wt. % SiO <sub>2</sub>		<74 wt. % SiO <sub>2</sub>		> 74 wt. % SiO <sub>2</sub>	
	Mean	± 2 sd	Mean	± 2 sd	Mean	± 2 sd	Mean	± 2 sd	Mean	± 2 sd
<b>Major elements</b>										
XRF	n=27		n=12		n=3		n=37		n=6	
SiO <sub>2</sub>	73.0	1.30	75.6	1.07	70.8	0.63	71.4	2.99	75.0	1.79
TiO <sub>2</sub>	0.30	0.05	0.21	0.09	0.41	0.03	0.32	0.07	0.24	0.11
Al <sub>2</sub> O <sub>3</sub>	14.4	1.06	13.1	0.77	15.3	0.69	16.3	2.39	14.0	1.45
Fe <sub>2</sub> O <sub>3</sub> T	2.42	0.41	1.77	0.56	3.28	0.50	2.45	0.86	1.83	0.50
MnO	0.06	0.01	0.04	0.01	0.08	0.03	0.05	0.02	0.04	0.01
MgO	0.43	0.11	0.28	0.15	0.57	0.05	0.39	0.13	0.30	0.12
CaO	2.07	0.34	1.34	0.30	2.47	0.18	2.04	0.41	1.62	0.28
Na <sub>2</sub> O	3.48	0.51	2.99	0.36	3.53	0.51	3.79	0.40	3.40	0.28
K <sub>2</sub> O	3.85	0.61	4.58	0.48	3.54	0.51	3.21	0.50	3.50	1.06
P <sub>2</sub> O <sub>5</sub>	0.03	0.08	0.02	0.01	0.05	0.09	0.06	0.12	0.07	0.12
<b>Totals normalised to 100%, volatile free</b>										
FeO T	2.17	0.37	1.59	0.51	2.95	0.45	2.21	0.78	1.64	0.45
LOI	1.96	1.74	2.57	0.87	2.76	0.97	3.55	1.50	3.22	0.94
<b>Trace elements</b>										
<b>Solution ICP-MS</b>										
	n=10		n=7		n=3		n=10		n=2	
Li	15.2	11.7	15.5	12.6	14.5	14.7	22.7	20.0	10.7	4.5
B	3.71	2.44	3.12	1.19	2.72	0.56	3.43	1.72	2.81	0.38
MgO wt. %	0.363	0.134	0.248	0.155	0.530	0.024	0.378	0.117	0.257	0.131
Sc	6.56	2.34	4.67	2.38	9.78	0.50	6.93	1.34	5.25	1.46
TiO <sub>2</sub> wt. %	0.256	0.055	0.188	0.106	0.371	0.028	0.313	0.068	0.215	0.036
V	17.6	6.7	10.7	8.9	25.2	2.1	20.0	3.9	15.1	2.8
Cr	2.15	1.78	1.16	0.80	2.39	1.59	1.96	0.64	2.27	2.37
Mn	392	36	301	97	722	-	361	173	-	-
Co	2.35	1.16	1.71	0.68	3.77	2.29	2.94	1.26	1.95	0.79
Ni	0.836	0.232	0.543	0.173	1.12	0.29	1.23	0.77	1.20	1.50
Cu	3.81	2.88	3.91	2.05	4.39	1.43	4.67	2.16	7.85	6.34
Zn	35.7	11.6	33.2	12.9	55.3	29.1	43.9	24.5	39.0	27.6
Ga	16.6	1.6	15.6	1.2	18.0	0.8	18.1	1.9	15.3	3.3
Rb	109	26	144	28	103	7	97.8	14	112	23
Sr	153	34	96	30	187	14	153	36	116	3
Y	23.9	4.5	25.1	3.8	27.9	2.2	22.8	4.4	24.7	4.5
Zr	104	28	85.0	33.9	172	42	116	17	89.7	19.0
Nb	8.22	0.74	8.31	1.57	9.64	0.36	9.79	1.05	7.82	2.05
Mo	1.43	0.66	1.60	0.57	1.46	0.45	1.35	0.49	1.76	0.23
Cs	6.37	2.11	8.95	2.23	5.09	1.29	5.94	1.04	6.55	1.31
Ba	729	79	791	116	718	132	747	109	692	163
La	23.3	5.3	26.5	2.5	24.6	3.9	22.9	4.5	24.5	8.8
Ce	47.0	7.2	52.3	5.3	52.5	9.6	48.4	10.9	47.1	12.0
Pr	5.51	1.54	6.07	0.69	5.93	0.85	5.19	0.99	5.72	1.42
Nd	20.6	5.8	22.0	3.0	22.7	2.9	19.0	3.7	20.8	4.9
Sm	4.22	1.19	4.38	0.74	4.79	0.48	3.82	0.72	4.22	0.92
Eu	0.93	0.23	0.71	0.16	1.14	0.12	0.86	0.15	0.78	0.00
Gd	4.13	1.04	4.21	0.62	4.81	0.45	3.81	0.68	4.24	0.53
Tb	0.631	0.161	0.634	0.113	0.739	0.099	0.596	0.114	0.628	0.08
Dy	3.96	0.88	4.03	0.68	4.69	0.42	3.77	0.68	4.02	0.55
Ho	0.826	0.165	0.842	0.142	0.971	0.089	0.783	0.145	0.827	0.137
Er	2.46	0.48	2.58	0.41	2.86	0.24	2.35	0.42	2.52	0.52
Tm	0.380	0.071	0.407	0.056	0.432	0.029	0.363	0.060	0.388	0.081
Yb	2.54	0.42	2.76	0.33	2.83	0.12	2.42	0.42	2.67	0.57

1	<b>Lu</b>	0.384	0.062	0.424	0.058	0.428	0.010	0.367	0.055	0.394	0.080
2	<b>Hf</b>	3.14	0.62	2.89	0.90	4.68	0.84	3.62	0.62	2.74	0.05
3	<b>Ta</b>	0.677	0.205	0.751	0.142	0.715	0.182	0.788	0.117	0.777	0.322
4	<b>W</b>	1.17	0.58	1.42	0.68	1.20	0.76	1.24	0.61	1.55	0.56
5	<b>Ti</b>	1.28	0.65	1.48	0.48	1.42	0.80	1.36	0.62	1.96	1.27
6	<b>Pb</b>	12.7	2.4	13.5	2.7	18.6	6.9	15.9	4.3	14.3	7.0
7	<b>Th</b>	10.5	1.3	13.4	1.3	9.75	0.73	11.8	1.7	11.3	4.1
8	<b>U</b>	2.35	0.33	2.90	0.22	2.29	0.14	2.35	0.30	2.50	0.59
9	<b>Eu/Eu*</b>	0.67	0.10	0.50	0.09	0.73	0.03	0.67	0.15	0.57	0.10

---

For Peer Review

Table 2: Mean matrix glass major and trace element concentrations for each compositional group within Kidnappers and Rocky Hill pumices

	Kidnappers matrix glass						Rocky Hill matrix glass			
	KI-1		KI-2		KI-3		RH-1		RH-2	
	Mean	$\pm 2\ sd$	Mean	$\pm 2\ sd$	Mean	$\pm 2\ sd$	Mean	$\pm 2\ sd$	Mean	$\pm 2\ sd$
<b>Major elements</b>										
EPMA	n=125		n=193		n=76		n=412		n=95	
SiO <sub>2</sub>	77.9	0.7	78.4	0.5	76.3	1.0	77.9	0.6	78.3	0.5
TiO <sub>2</sub>	0.136	0.042	0.081	0.047	0.153	0.039	0.137	0.036	0.096	0.024
Al <sub>2</sub> O <sub>3</sub>	12.5	0.3	12.5	0.3	13.4	0.3	12.6	0.2	12.5	0.2
Fe <sub>2</sub> O <sub>3</sub> T	1.15	0.54	0.62	0.51	1.38	0.59	0.94	0.56	0.63	0.52
MnO	0.031	0.039	0.025	0.036	0.047	0.044	0.017	0.032	0.017	0.028
MgO	0.104	0.043	0.046	0.057	0.153	0.063	0.057	0.082	0.045	0.069
CaO	1.06	0.11	0.73	0.22	1.31	0.17	0.95	0.13	0.74	0.06
Na <sub>2</sub> O	3.48	0.50	3.39	0.50	3.91	0.40	3.61	0.26	3.53	0.37
K <sub>2</sub> O	3.64	0.37	4.25	0.73	3.40	0.38	3.77	0.35	4.13	0.23
<b>Raw uncorrected total</b>	95.0		95.7		96.4		95.8		95.9	
<b>Trace elements</b>										
LA-ICP-MS	n=32		n=29		n=16		n=61		n=29	
Li	42.1	20.5	36.7	16.9	34.8	17.0	47.2	20.5	52.3	13.7
Na <sub>2</sub> O wt. %	3.65	0.56	3.36	0.66	3.72	1.67	4.01	1.08	3.88	0.75
MgO wt. %	0.145	0.168	0.102	0.095	0.268	0.178	0.076	0.120	0.083	0.066
CaO wt. %	1.01	0.51	0.88	0.41	1.38	0.61	1.06	0.30	0.87	0.41
Sc	9.64	7.35	6.10	11.53	10.5	6.5	9.69	4.03	7.02	1.75
TiO <sub>2</sub> wt. %	0.17	0.05	0.12	0.04	0.23	0.09	0.18	0.13	0.12	0.01
V	2.08	2.36	1.35	2.12	2.76	2.77	3.06	3.41	1.34	0.50
Mn	204	116	242	122	356	134	146	57	154	64
Co	1.04	1.89	0.540	2.044	1.21	2.66	1.07	1.82	0.28	1.17
Ni	1.47	6.13	1.30	6.65	1.75	5.78	0.75	4.04	0.84	5.14
Cu	5.66	24.84	4.66	35.89	6.26	42.51	9.15	28.06	-	-
Zn	28.4	21.2	25.7	18.4	36.2	22.8	27.3	34.0	21.5	21.5
Ga	16.4	5.8	15.8	4.5	15.6	5.3	17.0	5.6	15.6	3.0
Rb	153	58	169	35	131	56	133	45	158	18
Sr	79.1	28.1	64.4	32.60	117	49	100	36	72.64	30.12
Y	32.5	42.1	27.1	14.0	28.1	15.6	29.8	13.4	27.5	8.9
Zr	140	60	102	55	201	86	164	72	101	28
Nb	9.98	2.89	9.49	2.71	10.5	2.4	10.8	4.6	8.92	1.39
Mo	2.16	3.91	1.84	2.36	1.68	1.99	1.72	0.86	1.87	1.19
Cs	8.16	3.58	8.51	2.78	6.41	2.24	7.42	1.82	8.51	3.08
Ba	856	204	868	184	827	164	860	215	930	159
La	30.7	20.6	29.3	11.9	28.1	9.1	31.2	14.0	30.6	9.0
Ce	57.0	14.9	54.9	10.0	54.4	11.4	56.2	14.3	57.5	10.2
Pr	6.71	6.03	6.09	1.92	5.92	2.11	6.15	2.12	6.24	1.49
Nd	27.4	36.3	23.4	14.2	25.6	9.4	24.5	9.2	23.9	7.2
Sm	5.81	11.08	4.51	3.42	4.93	3.31	4.93	2.02	4.77	2.02
Eu	0.694	1.095	0.631	0.710	0.818	0.496	0.662	0.291	0.507	0.235
Gd	5.17	8.47	3.83	3.93	4.63	4.04	4.69	2.40	4.16	1.72
Tb	0.804	1.392	0.613	0.518	0.772	0.436	0.731	0.369	0.681	0.253
Dy	5.85	8.02	4.28	3.03	5.35	3.35	4.91	2.30	4.48	1.60
Ho	1.21	1.63	1.01	0.66	1.15	0.91	1.06	0.57	0.93	0.38
Er	3.45	4.04	2.93	2.07	2.85	2.38	3.18	1.53	2.95	1.14
Tm	0.518	0.706	0.427	0.448	0.540	0.385	0.495	0.246	0.501	0.208
Yb	3.74	4.10	2.96	2.23	2.70	2.85	3.48	1.82	3.35	1.27
Lu	0.573	0.688	0.513	0.385	0.537	0.418	0.550	0.254	0.571	0.299
Hf	4.11	2.47	3.38	2.11	5.47	3.45	5.02	2.48	3.68	1.37
Ta	0.903	0.565	0.941	0.602	0.859	0.495	0.993	0.422	0.979	0.304
W	2.10	1.52	2.25	1.76	1.74	1.52	2.23	1.87	2.21	0.88
Pb	17.5	3.2	17.1	6.1	20.3	6.2	21.5	7.0	19.1	4.3
Th	16.0	6.3	16.3	6.8	13.7	5.4	16.4	6.1	17.4	4.8
U	3.55	1.49	3.73	1.31	3.08	0.75	3.36	0.67	3.71	0.79

1  
2  
3  
4  
5  
6  
7  
8  
9  
10  
11  
12  
13  
14  
15  
16  
17  
18  
19  
20  
21  
22  
23  
24  
25  
26  
27  
28  
29  
30  
31  
32  
33  
34  
35  
36  
37  
38  
39  
40  
41  
42  
43  
44  
45  
46  
47  
48  
49  
50  
51  
52  
53  
54  
55  
56  
57  
58  
59  
60

<b>Rb/Sr</b>	2.81	4.95	1.00	14.73	2.73	10.40	1.82	1.18	2.79	1.83
<b>Eu/Eu*</b>	0.45	0.47	0.45	0.56	0.53	0.27	0.43	0.19	0.36	0.23

---

For Peer Review

Table 3: Summary of mineral characteristics and features from all deposits

	<b>Phenocryst size</b>	<b>Characteristics</b>	<b>Notable features</b>
<b>Plagioclase</b>	$\leq 2\text{mm}$	Euhedral to subhedral	Variable and complex zoning
<b>Orthopyroxene</b>	$\leq 1\text{mm}$	Subhedral, fractured with ragged terminations	Near ubiquitous Fe-Ti oxide inclusions $\pm$ zircon & apatite
<b>Quartz</b>	$\leq 2\text{mm}$	Euhedral, bipyramidal, often broken	Variable and complex zoning in CL
<b>Amphibole</b>	$\leq 3\text{mm}$ (Kid) $\leq 5\text{mm}$ (RH)	Euhedral, prismatic	Fe-Ti oxide inclusions common $\pm$ apatite
<b>Biotite</b>	$\leq 1\text{mm}$	Euhedral to subhedral books and flakes	Golden coloured and weathered, 'fresher' in RH No clear zoning
<b>Fe-Ti oxides</b>	$\leq 200\mu\text{m}$	Discrete oxides altered and oxidized	

Table 4: Range and average mineral compositions from each compositional group

Deposit Group	Kidnappers fall deposit		Kidnappers ignimbrite			Rocky Hill ignimbrite	
	KF-A	KF-B	KI-1	KI-2	KI-3	RH-1	RH-2
<b>Plagioclase</b>							
Total range	An <sub>31</sub> Or <sub>0.9</sub> - An <sub>63</sub> Or <sub>3.2</sub>	An <sub>26</sub> Or <sub>1.1</sub> - An <sub>57</sub> Or <sub>4.2</sub>	An <sub>26</sub> Or <sub>0.8</sub> - An <sub>65</sub> Or <sub>3.8</sub>	An <sub>21</sub> Or <sub>0.9</sub> - An <sub>65</sub> Or <sub>6.0</sub>	An <sub>27</sub> Or <sub>0.8</sub> - An <sub>65</sub> Or <sub>3.6</sub>	An <sub>25</sub> Or <sub>0.8</sub> - An <sub>64</sub> Or <sub>4.6</sub>	An <sub>23</sub> Or <sub>1.0</sub> - An <sub>59</sub> Or <sub>4.5</sub>
Core average	An <sub>39</sub> Or <sub>2.4</sub>	An <sub>37</sub> Or <sub>2.7</sub>	An <sub>37</sub> Or <sub>2.6</sub>	An <sub>36</sub> Or <sub>2.8</sub>	An <sub>35</sub> Or <sub>2.7</sub>	An <sub>36</sub> Or <sub>2.5</sub>	An <sub>33</sub> Or <sub>2.9</sub>
Rim average	An <sub>37</sub> Or <sub>2.5</sub>	An <sub>33</sub> Or <sub>3.1</sub>	An <sub>35</sub> Or <sub>2.7</sub>	An <sub>30</sub> Or <sub>3.7</sub>	An <sub>38</sub> Or <sub>2.2</sub>	An <sub>36</sub> Or <sub>2.4</sub>	An <sub>30</sub> Or <sub>3.3</sub>
<b>Orthopyroxene</b>							
Total range	En <sub>44</sub> Wo <sub>2.0</sub> - En <sub>61</sub> Wo <sub>2.2</sub>	En <sub>42</sub> Wo <sub>1.5</sub> - En <sub>63</sub> Wo <sub>3.6</sub>	En <sub>42</sub> Wo <sub>1.1</sub> - En <sub>68</sub> Wo <sub>4.1</sub>	En <sub>41</sub> Wo <sub>1.6</sub> - En <sub>65</sub> Wo <sub>5.2</sub>	En <sub>43</sub> Wo <sub>1.6</sub> - En <sub>66</sub> Wo <sub>4.8</sub>	En <sub>42</sub> Wo <sub>0.8</sub> - En <sub>62</sub> Wo <sub>3.6</sub>	En <sub>43</sub> Wo <sub>1.5</sub> - En <sub>63</sub> Wo <sub>4.4</sub>
Core average	En <sub>49</sub> Wo <sub>2.5</sub>	En <sub>48</sub> Wo <sub>2.5</sub>	En <sub>48</sub> Wo <sub>2.5</sub>	En <sub>48</sub> Wo <sub>2.5</sub>	En <sub>49</sub> Wo <sub>2.6</sub>	En <sub>48</sub> Wo <sub>2.4</sub>	En <sub>48</sub> Wo <sub>2.2</sub>
Rim average	En <sub>47</sub> Wo <sub>2.4</sub>	En <sub>46</sub> Wo <sub>2.2</sub>	En <sub>45</sub> Wo <sub>2.3</sub>	En <sub>44</sub> Wo <sub>2.1</sub>	En <sub>47</sub> Wo <sub>2.5</sub>	En <sub>45</sub> Wo <sub>3.4</sub>	En <sub>45</sub> Wo <sub>1.6</sub>
<b>Amphibole</b>							
Total range	1.07-1.7 Al <sup>T</sup>	1.05-1.78 Al <sup>T</sup>	1.01-1.94 Al <sup>T</sup>	1.02-1.82 Al <sup>T</sup>	0.99-1.85 Al <sup>T</sup>	0.97-1.99 Al <sup>T</sup>	1.02-1.87 Al <sup>T</sup>
Core average	1.31 Al <sup>T</sup>	1.31 Al <sup>T</sup>	1.30 Al <sup>T</sup>	1.28 Al <sup>T</sup>	1.31 Al <sup>T</sup>	1.29 Al <sup>T</sup>	1.27 Al <sup>T</sup>
Rim average	1.20 Al <sup>T</sup>	1.26 Al <sup>T</sup>	1.26 Al <sup>T</sup>	1.15 Al <sup>T</sup>	1.42 Al <sup>T</sup>	1.24 Al <sup>T</sup>	1.13 Al <sup>T</sup>
<b>Magnetite</b>							
Total range	Usp <sub>0.27-0.46</sub>	Usp <sub>0.29-0.38</sub>	Usp <sub>0.23-0.49</sub>	Usp <sub>0.27-0.36</sub>	Usp <sub>0.24-0.42</sub>	Usp <sub>0.23-0.48</sub>	Usp <sub>0.16-0.32</sub>
Average	Usp <sub>0.33</sub>	Usp <sub>0.30</sub>	Usp <sub>31</sub>	Usp <sub>31</sub>	Usp <sub>35</sub>	Usp <sub>31</sub>	Usp <sub>28</sub>
<b>Ilmenite</b>							
Total range	Ilm <sub>0.88-0.93</sub>	Ilm <sub>0.88-0.91</sub>	Ilm <sub>0.85-0.90</sub>	Ilm <sub>0.80-0.90</sub>	Ilm <sub>0.86-0.91</sub>	Ilm <sub>0.80-0.90</sub>	Ilm <sub>0.84-0.91</sub>
Average	Ilm <sub>0.89</sub>	Ilm <sub>0.89</sub>	Ilm <sub>0.88</sub>	Ilm <sub>0.89</sub>	Ilm <sub>0.88</sub>	Ilm <sub>0.88</sub>	Ilm <sub>0.89</sub>

Table 5: Summary of model temperature, pressure and oxygen fugacity estimates

	Kidnappers fall deposit		Kidnappers ig.			Rocky Hill ig.	
	KF-A	KF-B	KI-1	KI-2	KI-3	RH-1	RH-2
<b>Amphibole</b>							
<b>Ridolfi et al., 2010</b>	Uncertainty: temp: $\pm 22$ °C ( $\sigma_{est}$ ), pressure: 11-24 %						
Core average T (°C)	805	810	800	805	805	810	800
Rim average T (°C)	780	795	785	780	820	795	765
Core average P (MPa)	130	135	130	125	130	130	125
Rim average P (MPa)	110	120	120	100	150	115	100
<b>Putirka, 2016</b>							
Uncertainty: eqn. 5: $\pm 30$ °C (SEE), eqn. 9: $\pm 39$ °C (SEE), eqn. 7a: 1.0 kbar							
Core average T (°C) eqn. 5	790	795	785	785	790	790	782
Rim average T (°C) eqn. 5	770	785	770	750	800	775	745
Core average T (°C) eqn. 9	805	805	800	790	805	800	785
Rim average T (°C) eqn. 9	790	790	790	770	815	790	765
Core average P (MPa) eqn. 7a	290	340	320	360	280	310	330
Rim average P (MPa) eqn. 7a	330	340	320	400	220	300	380
<b>Fe-Ti oxides</b>							
<b>Ghiorso &amp; Evans, 2008</b>	Uncertainty: $\pm 50$ °C ( $2\sigma$ ; Hora et al., 2013)						
Average T (°C)	810	785	830	800	860	830	790
Average Log $f_{O_2}$	-13.7	-14.2	-13.1	-13.9	-12.5	-13.2	-14.0
<b>Plagioclase-melt</b>							
<b>Putirka, 2008</b>	Uncertainty: $\pm 36$ °C (SEE)						
Rim average T (°C)	-	-	780	750	820	785	760
<b>Orthopyroxene-melt</b>							
<b>Putirka, 2008</b>	Uncertainty: $\pm 41$ °C (SEE)						
Rim average T (°C)	-	-	775	750	795	770	760

Uncertainties are those reported in the original studies unless otherwise stated. SEE = standard error of estimate, aad = average absolute deviation.